universität wien

MASTERARBEIT / MASTER'S THESIS

Titel der Masterarbeit / Title of the Master's Thesis

„Complex Dynamics of Star-forming Filaments: Comparison between models and observations“

verfasst von / submitted by

Johannes Mayer, B.Sc.

angestrebter akademischer Grad / in partial fulfilment of the requirements for the degree of

Master of Science (M.Sc.)

Wien, 2016 / Vienna 2016

Studienkennzahl lt. Studienblatt / degree programme code as it appears on the student record sheet:	A 066 861
Studienrichtung lt. Studienblatt / degree programme as it appears on the student record sheet:	Masterstudium Astronomie
Betreut von / Supervisor:	Dr. Alvaro Hacar Gonzalez
Mitbetreut von / Co-Supervisor:	

Abstract

I have investigated the evolution and dynamics of filaments in molecular clouds by simulating the time-evolution of their radial profiles. Rotation, infall and different dust species were considered to investigate their effect on the evolution. Synthetic spectra were developed for each model to make a statement and prediction about observable signatures for filaments. I found a clear separation of gas and dust species in all phases of the evolution due to a pure dynamical effect. After some dynamical evolution, radial profiles in equilibrium reveal that large dust grains must primarily be found within the filament while small dust grains are located beyond the filament as well. Moreover, gas-to-dust ratios at this stage are not constant and strongly depends on the radius and dust grain sizes. The evolution of the filament is divided into two phases. The first phase is called the infall phase and is dominated by inwards falling material. The second phase is called re-expansion phase and initiates when material starts to settle an equilibrium configuration at the center of the filament. Finally, the development of synthetic spectra reveals that we can clearly distinguish between time steps of the infall phase while it is difficult to differentiate between individual time steps of the subsequent re-expansion phase.

Zusammenfassung

Mit eindimensionalen Simulationen wurde die zeitliche Entwicklung und Dynamik von Filamenten in Molekülwolken untersucht. Die Berücksichtigung von Rotation, Gaseinfall und Staub ermöglichte es, deren Einfluss auf die Entwicklung zu untersuchen. Künstliche Spektren wurden entwickelt um eine Aussage über mögliche Signaturen in den Beobachtungen von Filamenten zu machen. Ich habe eine deutliche Separierung einzelner Staubkomponenten in allen Phasen der Entwicklung entdeckt, dass auf einen rein dynamischen Effekt zurückzuführen ist. Des Weiteren sieht man, dass große Staubpartikeln hauptsächlich innerhalb des Filaments zu sehen sein sollten, während kleine Staubteilchen auch außerhalb des Filaments zu finden sind. Außerdem wurde gezeigt, dass das Verhältnis zwischen Gas und Staub nicht konstant ist und stark von der Staubgröße abhängig ist und mit dem Radius des Filaments variiert. Die zeitliche Entwicklung eines Filaments wurde in zwei Phasen geteilt. Mit künstlichen Spektren wurde gezeigt, dass der aktuelle Entwicklungszustand eines Filaments nur während der 1. Phase ("infall phase") der Entstehung eindeutig bestimmt werden kann, während einzelne Zeitschritte der 2. Phase ("re-expansion phase") nicht zu unterscheiden sind.

Contents

Part I.
Introduction

Historical Review

Filaments in molecular clouds have already been emphasized by Edward Barnard observing the Taurus complex in 1907 (Barnard, 1907). 12 years later, he published the first systematic photographic survey of dark clouds, a catalogue containing 182 clouds (Barnard, 1919). At this time, dark clouds were not directly connected to the star formation process. It was Bart J. Bok in 1946 that claimed first that dark nebulae ('Bok globules') are the sites of stellar birth. This theory was then supported by infrared and millimeter observations in the latter half of the twentieth century. The finding of molecules in space in the sixties manifested that dark clouds are made of molecules with molecular Hydrogen H_2 as major contributor (Weinreb et al. (1963), Wilson et al. (1970)). A detailed research on filaments itself has begun in 1979 when S. Schneider and B. Elmegreen published their catalog of dark globular filaments comprising a list of 23 filamentary objects (Schneider and Elmegreen, 1979) including regions like L1517, L1529 and L1495 in the Taurus dark cloud complex (see Fig.1). These filamentary structures have also been found in radio observations, for instance, in ^{13}CO maps of the Orion A molecular cloud (Bally et al. (1987), Johnstone and Bally (1999)). Another breakthrough followed when submillimeter observations with the Herschel Space Observatory (through thermal dust emission, see below) have revealed that filaments are ubiquitous in molecular clouds (André et al. (2010), Molinari et al. (2010)) and possess an universal width of ∼0.1 pc (Arzoumanian et al., 2011) where only the densest regions are able to develop prestellar cores.

Filaments & Cores

A lot of work has been done to investigate the origin of the universal width of filaments (see for instance Hennebelle (2013)), but it is still matter of debate. These findings privilege a picture in which filaments and prestellar cores represent the key steps in the star formation process (André et al., 2014). At this point, it is important to define a filament and different types of cores. A prestellar core is a gravitational bound overdensity which is starless, while a protostellar core hosts a protostar (André et al., 2014). A starless core does not show any evidence of star formation. According to the definition by André et al. (2014), filaments are elongated structures of interstellar medium (ISM) with an aspect ratio larger than ∼5-10 with a significantly overdensity with respect to its surroundings. I take the liberty of adopting this definition for this thesis. Moreover, Herschel observations of active star-forming regions have shown that prestellar cores are primarily located in filaments exceeding a critical mass per unit length of $M_{\mathrm{line,crit}} \simeq 16\ M_\odot\ \mathrm{pc}^{-1}$ ($=2c_s^2/G$ with $c_s \sim 0.2$ km s^{-1} for an isothermal filament with T = 10 K)(Inutsuka and Miyama, 1997). This linear mass can be calculated by

$$M_{line} = \int_0^\infty 2\pi r \rho(r) dr \tag{1}$$

where the density profile ρ(r) for an isothermal filament in hydrostatic equilibrium can be described by the analytical Ostriker profile (Ostriker, 1964)

$$\rho_{Ostr} = \rho(r) = \rho_0 \left[1 + \left(\frac{r}{H}\right)^2\right]^{-2} \tag{2}$$

where ρ_0 is the central density, r is the radial distance from the center of the filament, and H is the height scale defined as

$$H = \sqrt{\frac{2c_s^2}{\pi G \rho_0}}. \tag{3}$$

Many clouds (for instance, Taurus, Polaris, and Ophiuchus) contain very long filaments, with a typical length of 1 pc up to several tens of pc, and appear to be co-linear with the longer extent of the host cloud (André et al., 2014). While dense self-gravitating filaments tend to be located perpendicular to the direction of the local magnetic filed, low-density sub-filaments (also called striations) tend to be parallel to the magnetic field feeding the main filaments with material with typical infall velocities of $\sim$0.5 - 1 km s^{-1} (Palmeirim et al., 2013).

Star-forming cores differ from their host cloud in terms of density, shape and internal motion. Thanks to multi-tracer analysis, where individual tracers sensitive to different density regimes are analysed, it is possible to investigate different density regimes allowing us to study their differences and the transition from low-density gas to dense cores. Thus, we should briefly emphasize the significance of different gas tracers, especially that of $C^{18}O$(1-0) and N_2H^+(1-0) (Diazenylium). $C^{18}O$ is a good tracer for diffuse gas ($>5{\cdot}10^2$ cm^{-3}) in molecular clouds while N_2H^+(1-0) is tracing gas with densities greater than 10^4 cm^{-3}, roughly the same density where $C^{18}O$ disappears from the gas phase by freezing out onto dust grains. Thus, dust plays a very important role in the chemical evolution of filaments and clouds (further details in section Dust).

Molecular Spectroscopy

Besides atomic spectral lines due to electronic transitions between two individual energy levels of an electron, rotational and vibrational transitions in molecules are important sources of spectral lines. During the transition of an energetic higher state E_k to a lower state E_j, atoms and molecules emit a photon according to the

energy difference of these levels $\Delta E = E_k - E_j = h \cdot \nu$, where h is the Planck constant and ν is the resulting frequency of the emitted photon. Since the energy difference of two levels is larger in electronic transitions than that of rotational and vibrational transitions in molecules, atomic lines can primarily be found at optical wavelengths while molecular spectral lines can be observed at larger wavelength (=lower energy), at infrared and radio wavelengths. Then one has

$$E_{electronic} \gg E_{vibrational} \gg E_{rotational}.$$

Back to $C^{18}O$ and N_2H^+, their rotational transition J = 1 - 0 occurs at 109.782 GHz and 93.173 GHz (corresponds to a wavelength of 2.730 mm and 3.217 mm), respectively, and can therefore be observed with radio telescopes. The isotope $C^{18}O$ and N_2H^+ is used for its property of being optical thin in molecular clouds allowing us to measure their gas column density, while $C^{16}O$ is optical thick and allow us to study massive clouds, rather than dense cores (Stahler and Palla, 2008). The intensity of different spectral lines depends on several cloud properties and can not easily be compared with each other. At low densities, well below the critical density for an excited state (the density for which collisional de-excitation matches the radiative de-excitation rate (Draine, 2010)), the excitation temperature T_{exc} is less than the kinetic temperature T_{kin} of the gas and the line intensity is proportional to the square of the density n (a detailed derivation can be found , for instance, in Dopita and Sutherland (2013)). Only at low densities and temperatures far below the excitation temperature for rotational transitions of molecules, the excitation of the upper levels are irrelevant (Tielens, 2005) and emission lines will be unobservable.

At densities close or above the critical density, T_{exc} becomes T_{kin} and the gas comes into thermal equilibrium (LTE) due to collisional de-excitation. The line intensity of molecules in this density regime is then linearly proportional to n. This is appropriate for an optical thin gas (no absorption and stimulated emission) where photons can leave the cloud unhindered. In optically thick clouds, however, the critical density is reduced due to trapping of photons and absorption processes. To sum up, the line intensity depends on the optical depth of the cloud and is proportional to n in density regimes near or above the critical density, and to n^2 in density regimes well below the critical density. Observations are most sensitive to gas with densities near the corresponding critical density n_{crit} (Stahler and Palla, 2008).

Velocity Structure and Formation of Filaments

Investigation of internal velocity structures in L1517 has shown that filaments has subsonic internal motions and are velocity-coherent (uniform velocity) over their whole length (Hacar and Tafalla, 2011), while their surrounding low-density gas is dominated by turbulent motions. Research on L1495 in the Taurus region has revealed that velocity-coherent filaments with a length of 0.5 pc are grouped and exhibit similar kinematics and chemical composition (Hacar et al., 2013). These groups of filamentary structures are called bundles. According to this picture, cores are formed in several steps. At first, a molecular cloud fragments into a filament with multiple bundles. These bundles will then fragment into velocity-coherent fil-

aments with similar size and velocity dispersion, also called fibers. Furthermore, some of these fibers will accrete enough mass to fragment into dense cores (Hacar et al., 2013; Tafalla and Hacar, 2015). A lifetime of $\sim 10^6$ years for prestellar and starless cores is relatively short compared to the lifetime of their host cloud (about 20 - 30 Myr, which is under debate (Matzner, 2002; Krumholz et al., 2006)). In particular, core lifetime depends on their average volume density and lie between one free-fall time (t_{ff}) and ($10 \times t_{ff}$) (Jessop and Ward-Thompson, 2000).

Theoretically, filaments can be formed by various processes. In simulations with supersonic turbulence, gas is quickly compressed to sheets and filaments (Porter et al. (1994), Padoan et al. (2001)). The origin of supersonic turbulence is extensive. It can be produced by supernovae, stellar winds, expanding HII regions, radiation pressure, Rayleigh-Taylor or gravitational instabilities (Elmegreen and Scalo, 2004). The collision of two shocked sheets or two planar shock wave fronts, an instability in self-gravitating sheets, or velocity shear in magnetized turbulent media can also result in the formation of filaments (Passot et al., 1995; Nagai et al., 1998; Padoan et al., 2001; Pudritz and Kevlahan, 2013).

Dust

As mentioned above, dust plays a crucial role in the chemical evolution of gas in molecular clouds, and also effects the gas motion due to drag forces. Dust in molecular clouds is observed primarily at sub-mm wavelengths, for instance, with the Herschel detector SPIRE (Spectral and Photometric Image Receiver) covering 250 to 500 μm wavelength. The dust grains emit thermal radiation according to the Planck's law for a definite temperature, that is, a maximum at $\sim$300 μm for a dust temperature of 10 K, or at $\sim$30 μm for a temperature of 100 K. Dust grains vary in size over several orders of magnitude, carbonaceous dust grains from a few nanometers up to $\sim$1 μm and silicates up $\sim$0.3 μm (Weingartner and Draine, 2001). The interaction with gas due to colliding atoms strongly depends on their size (and other physical phenomena, such as electric charge and surface characteristics of dust grains) leading to a drift velocity between gas and dust (Draine, 2010).

Dust grains have a fundamental impact on the interstellar chemistry and formation of molecules. The most abundant molecule H_2 is formed either on dust grains (grain catalysis, Gould and Salpeter (1963)) or, in the absence of dust, in the gas-phase by associative detachment of H^- and H (see, for instance, Draine (2010) or Dopita and Sutherland (2013)). The abundance of elements in the gas-phase is also effected by dust grains, it is reduced by a process known as interstellar depletion. Here, individual molecule species are depleted from the gas-phase at a certain density by freezing out onto the dust grains. This leads to tracers for different gas densities, as mentioned above. This is not only because of depletion, but also relative abundances, excitation and chemical evolution.

At low densities, C-bearing molecules like CO dominate the gas-phase (beside the most abundant molecule H_2). When the gas density increases, CO starts to deplete from the gas-phase and species like N_2H^+ increase in abundance (CO is the major destroyer of N_2H^+ and other molecular ions). Then, NH_3 is formed out of N_2H^+.

Thus, N-bearing molecules are dominant at densities where CO starts to deplete, that is, primarily in dense regions (see Bergin and Tafalla (2007) and their references). Another effect realized by dust is the shielding of molecular clouds from starlight reducing the ionization of gas and the photo-dissociation of molecules by absorption of UV photons (Li et al., 2013). Thus, dust is an important component of the ISM, although the average gas to dust ratio in the Milky Way is $\sim$100.

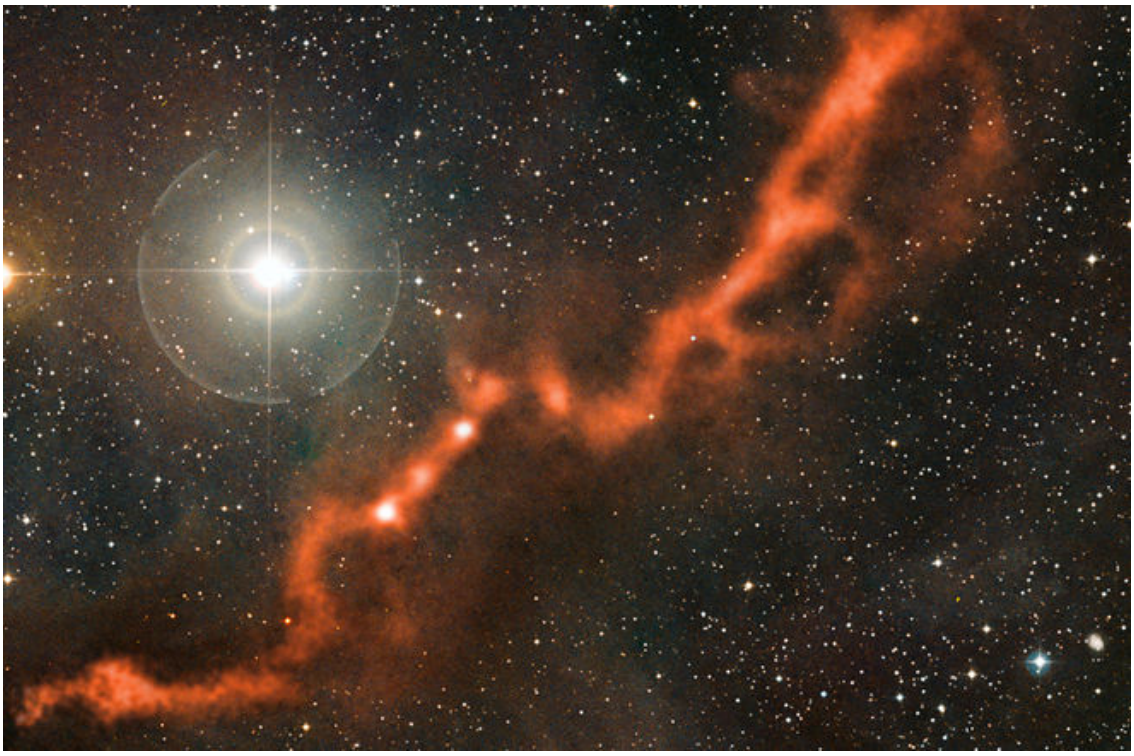

Figure 1: APEX image (870 μm) of the star-forming filament L1495 in the Taurus Complex superimposed on an optical image. Credit: ESO/APEX (MPIfR/ESO/OSO)/A. Hacar et al./Digitized Sky Survey 2. Acknowledgment: Davide De Martin.

Part II.
Motivation

Filaments in molecular cloud complexes like Taurus, Perseus and Aquila are known to be the factory for low mass stars. It is, therefore, important to understand the evolution, chemical and physical processes in such filaments. Since observations reveal us the dynamical (but also chemical) state of the filaments only for a single point in time, it is crucial to develop numerical simulations explaining our observations and understanding the star formation processes. They have, for instance, shown that molecular clouds must be highly filamentary before Herschel found the omnipresence of filaments (see Porter et al. (1994); Padoan et al. (2001); Nagai et al. (1998) and Passot et al. (1995)). The transition from diffuse gas to cores is still matter of debate and many different models are discussed. However, it is conclusive that dust plays an important role in the formation and evolution of filaments, but it is not clear it is doing considering the low gas-to-dust ratio of 100. Dust is crucial for the formation of molecules at different gas densities allowing us to observe and analyze individual density regimes, on the one hand, and for the shielding of molecules and molecular clouds from starlight, on the other hand. Therefore, it is appropriate to pay particular attention for dust and their evolution within filaments and molecular clouds.

The main motivation behind this thesis is to understand and interpret current observations of dust and molecules. I have developed synthetic spectra for individual models with different initial conditions by using a cylindrical, shell-like approach for one-dimensional simulations to explore the evolution of filaments and compare current observations with models. How can we diagnose the current dynamical state of observed filaments? How can we determine previous and upcoming evolution of these filaments? It is important to understand the evolution and dynamics of filaments and the transition from diffuse to dense gas, which is a crucial step in the star formation process, if not the most important one. It is also important to develop faithful models to make a detailed comparison with observations. Even when these simulations do not consider important processes like turbulence or radiation transfer, it can be shown that the evolution proceeds in different ways and depends on the initial conditions and assumptions. What are the initial conditions for observed filaments? How can we distinguish between different initial conditions and how can we determine the current dynamical state of a filament? How is dust acting in filaments during their evolution? How is the gas effected by dust? The goal of this thesis is to find an answer for these questions.

Part III. Simulations

1. Numerical Methods

I have investigated the dynamics of filaments in molecular clouds by programming an one-dimensional *FORTRAN 90* code to solve the hydrodynamic equations introduced in section 1.1. For this purpose, I have used the schemes of section 1.3 considering specific boundary conditions (section 1.4). The subsequent chapter introduces all basic equations for this code and is primarily referred to the books by Toro (1999), LeVeque et al. (1998) and LeVeque (2002), respectively. The scope of these simulations is to investigate the evolution of filaments in free fall collapse considering various initial conditions.
This part is structured as following. I start with a description of the three conservation equations, mass conservation, momentum conservation, and energy conservation, followed by the source term vector. Central schemes and time splitting methods are presented in section 1.3 and boundary conditions are introduced in the section 1.4. Further information about the code and implementations, such as gravity, are presented in section 2, and initial conditions can be found in section 3. In order to facilitate the reader, table 1 lists all symbols and their meanings I have used in this thesis.

1.1. Conservation Equations

1.1.1. Mass Conservation

The equation of mass conservation describes that no mass is generated or annihilated within a control volume dV. This law is described mathematically by the continuity equation

$$\rho_t + \nabla \cdot (\rho \mathbf{V}) = 0 \tag{4}$$

where ρ_t is the partial derivative of the density with respect to time, ∇ the three dimensional Nabla operator in Cartesian coordinates, and $\mathbf{V}$ the three dimensional velocity vector

$$\mathbf{V} = \begin{pmatrix} u \\ v \\ w \end{pmatrix}.$$

Thus, the second term in Eq.4 represents the flux of mass entering and leaving the control volume dV, and the first term the change of the mass in time. In the one

Symbol	Meaning
r	Radial distance
Δr	Spatial length of a grid cell
u	Radial velocity
$\mathbf{V}$	3D velocity vector
P	Pressure
T	Temperature
E	Total energy
ρ_{g}	Mass density of the gas
ρ_{dx}	Dust mass density of species x, where x=1,2,3
s	Dust grain size
κ_0,κ_d,κ_g	Drag coefficients
$\mathrm{c_s}$	Local sound speed
$\mathrm{M_{lin}}$	Linear mass [$\mathrm{M_\odot\ pc^{-1}}$]
$\mathbf{U}_{\mathrm{i}}^{\mathrm{n}}$	Vector of conserved variables in cell i at time n
$\mathbf{F}(\mathbf{U})$	Physical flux vector
$\mathbf{S}(\mathbf{U})$	Source term vector
Δt	Time step
$\mathrm{k_b}$	Boltzmann constant
$\mathrm{m_u}$	Atomic mass unit
μ	Mean molecular weight
ω	Rotational frequency [$\mathrm{s^{-1}}$]
G	Gravitation constant in SI base units
Φ	Gravitational potential
γ	Adiabatic exponent
$\mathrm{v_P}$	Projected velocity
$\mathrm{I(v_P)}$	Line intensity

Table 1: Meaning of the most important symbols.

dimensional case the vector $\mathbf{V}$ can simplified to $\mathbf{V} = \mathrm{u}$.

1.1.2. Momentum Conservation

The equation of momentum conservation represents the motion of a fluid and transport of momentum as described by Eq.5. In the first instance, this motion is dominated by the pressure force P. Additional forces are considered in chapter 2.

$$(\rho\mathbf{V})_t + \nabla \cdot (\rho\mathbf{V} \otimes \mathbf{V} + P\mathbf{I}) = 0 \tag{5}$$

The $\otimes$ represents the dyadic product of the velocity vectors. In Cartesian coordinates, this is expressed as

$$\mathbf{V} \otimes \mathbf{V} = \mathbf{V} \cdot \mathbf{V}^T = \begin{pmatrix} u \\ v \\ w \end{pmatrix} (u \quad v \quad w) = \begin{pmatrix} u^2 & uv & uw \\ vu & v^2 & vw \\ wu & wv & w^2 \end{pmatrix}.$$

Again, in one-dimensional simulations the dyadic product of the velocity vectors can be simplified to u^2. The vector $\mathbf{I}$ in the pressure term in Eq.5 represents the unit tensor

$$\mathbf{I} = \begin{pmatrix} 1 & 0 & 0 \\ 0 & 1 & 0 \\ 0 & 0 & 1 \end{pmatrix}$$

and can also be neglected in 1D simulations. The pressure P can be calculated with the help of the ideal gas equation. For an isothermal system, the adiabatic exponent $\gamma = c_p/c_c = 1$ and the pressure of an ideal gas can be expressed by

$$P = c_s^2 \rho = \frac{k_b T}{m_u \mu} \tag{6}$$

where c_s represents the local sound speed, $k_b = 1.38 \cdot 10^{-23}$ J K^{-1} the Boltzmann constant, T the temperature, μ the mean molecular weight of the gas, and $m_u = 1.66 \cdot 10^{-27}$ kg the atomic mass unit (mass of a hydrogen atom). I have considered a temperature of T = 10 K (Benson and Myers, 1989) and $\mu = 2.3$ (Kauffmann et al., 2008) for a cold molecular cloud, a typical value for a cloud composed of molecular hydrogen H_2 and Helium with an abundance of 10%, resulting in $c_s = 190.1$ m s^{-1}.

1.1.3. Energy Conservation

The energy conservation equation in conservative form is written as

$$(\rho E)_t + \nabla \cdot [(\rho E + P)\mathbf{V})] = 0. \tag{7}$$

The total energy E per unit volume is

$$E = \frac{1}{2}\mathbf{V}^2 + \frac{P}{(\gamma - 1)\rho} \tag{8}$$

where the first term represents the specific kinetic energy and latter one the specific internal energy (Toro, 1999) of an ideal gas. Thus, the first term of Eq.7 illustrates

the change of flux of the total energy in a control volume dV with respect to time, while the second and third term corresponds to the work done by the total energy and the pressure of the fluid, respectively. In isothermal systems, where $\gamma = 1$, the sound speed is constant, thus P and ρ are always proportional to each other. In this case, the energy conservation equation can be neglected and the hydrodynamics of a fluid is simplified to the mass and momentum conservation equation.

1.1.4. Summary of the Conservation Equations

By combining the individual terms of the three equations of conservation (Eq.4, Eq.5, and Eq.7) to vectors with respect to the time and space derivative, respectively, we obtain

$$\mathbf{U} = \begin{pmatrix} \rho \\ \rho u \\ \rho E \end{pmatrix} \qquad \mathbf{F}(\mathbf{U}) = \begin{pmatrix} \rho u \\ \rho u^2 + P \\ (\rho E + P)u \end{pmatrix} \tag{9}$$

where $\mathbf{U}$ is the vector of conserved variables and $\mathbf{F}(\mathbf{U})$ is called the physical flux vector (calculated with the quantities in $\mathbf{U}$) composing a non-linear system that can be expressed in Cartesian coordinates in the form

$$\mathbf{U}_t + \mathbf{F}(\mathbf{U})_r = \mathbf{S}(\mathbf{U}). \tag{10}$$

where $\mathbf{S}(\mathbf{U})$ is the source term vector. This is called the conservative form of the conservation equations. Notice that we are neglecting here a number of physical processes (radiation, turbulence, viscosity, thermal conduction) which might play a role in the dynamics of filaments. Some processes, for instance gravity and drag force, will be introduced later on. The equation is called homogeneous when $\mathbf{S}(\mathbf{U}) = 0$.

1.2. Geometric Source Term Vector and Symmetry

In case of curvilinear coordinates, the conservation equations are not as simple as in Eq.10, because of geometrical effects. In the case of spherical or cylindrical symmetries, they can be taken into account by simply introducing a geometrical source term on the right hand side of Eq.10. This has the form

$$\mathbf{S}(\mathbf{U}) = -\frac{\alpha}{r} \begin{bmatrix} \rho u \\ \rho u^2 \\ u(E + p) \end{bmatrix} \tag{11}$$

where r is the radial distance from the origin and u is the radial velocity (Toro, 1999). The system is assumed to have planar symmetry when $\alpha = 0$, cylindrical symmetry when $\alpha = 1$ (approximation to two-dimensional flow), and spherical symmetry when $\alpha = 2$ (approximation to three-dimensional flow). See section 5 and part IV for a discussion about the implementation of the geometric source term.

1.3. Central Schemes and Time Splitting Methods

In this section, I study different finite volume methods for numerically solving the system of equations presented by Eq.9 and Eq.10, respectively. For the sake of simplicity, I will consider a planar geometry. A finite volume method is based on subdividing the spatial domain into j intervals (LeVeque, 2002) as shown in Fig.2. These intervals are called grid cells (with a spatial length Δr) and define the resolution of the simulations. The grid cells do not have to have an uniform volume. I also implemented an expanding grid cell, but for simplicity I considered only an uniform cell size. Each grid cell i is defined by a vector of conserved variables $\mathbf{U}_\mathrm{i}^\mathrm{n}$ at time n and two intercell fluxes on the left $\mathbf{F}^n_{i-1/2}$ and right interface $\mathbf{F}^n_{i+1/2}$. To calculate the quantities in all cells, ghost cells are needed (green cells in Fig.2). Intercell fluxes define the evolution of the fluid in space and can be calculated with, for instance, the Lax-Friedrichs or Rusanov scheme (see following subsections). The evolution of the vector of conserved variables in time $\mathbf{U}_i^{n+1}$ follows by the application of time splitting methods, such as the Godunov or Strang splitting methods (see section 1.3.3 and 1.3.4). For simplicity, vector $\mathbf{F}(\mathbf{U})$ and $\mathbf{U}$ are not in bold for the remaining chapter.

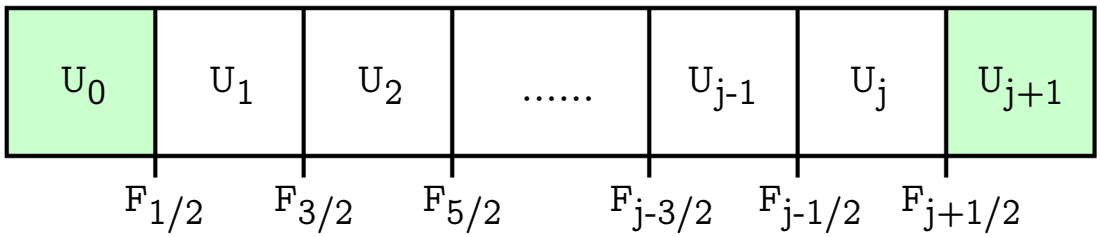

Figure 2: Schematic illustration of the finite volume method. Ghost cells are illustrated by green cells, U_0 represents the innermost ghost cell, $\mathrm{U}_{\mathrm{i}+1}$ the outer one, and F the intercell fluxes. Each cell has a size of Δr and i is the number of cells covering the spatial domain $\mathrm{r}_{\mathrm{max}}$ between $\mathrm{F}_{1/2}$ and $\mathrm{F}_{\mathrm{i}+1/2}$.

The basic equation for solving the system of conservation equations in the i-th cell can be written in the form

$$U_i^{n+1} = U_i^n + \frac{\Delta t}{\Delta r}[F_{i-1/2} - F_{i+1/2}] \tag{12}$$

where Δt is the time step (see section 1.3.5 for further details), Δr is the spatial length of a grid cell, and $\mathrm{F}_{\mathrm{i} \pm 1/2}$ is the numerical flux vector calculated with the

schemes introduced in the following subsections. This vector differs from physical flux vector F_i in Eq.9. The vector F_i represents the flux within a grid cell while the numerical flux vector $F_{i+1/2}$ is an approximation to the physical flux vector and illustrates the interaction between the cell *i* and *i + 1* at the interface *i + 1/2*. The exponent *n* and *n+1* of the vector U is referred to the current and subsequent time step, respectively.

1.3.1. Lax-Friedrichs Scheme

The Lax-Friedrichs (LxF) scheme (Lax, 1954) for intercell flux at i+1/2 between the cell U_i and U_{i+1} is written as

$$F_{i+1/2}^{LxF} = \frac{1}{2}[F_i^n + F_{i+1}^n] + \frac{1}{2}\frac{\Delta r}{\Delta t}(U_i^n - U_{i+1}^n) \tag{13}$$

where $\Delta r/\Delta t$ is also called the grid speed, and F and U on the right-hand side are vectors according to Eq.9. Again, the physical flux vector $F_i^n = F(U_i^n)$ within the square brackets is calculated with U, according to Eq.9, and differs from the numerical flux F^{LxF}. This is also valid for the following Rusanov scheme. This scheme is a modification of the Forward-Time Central-Space scheme and is stable for a Courant number up to 1 (see section 1.3.5).

1.3.2. Rusanov Scheme

The Rusanov flux scheme (Rusanov, 1961), also called the local Lax-Friedrichs scheme, is given by

$$F_{i+1/2}^{Rusa} = \frac{1}{2}[F_i^n + F_{i+1}^n] + \frac{1}{2}S_{i+1/2}^{+}(U_i^n - U_{i+1}^n) \tag{14}$$

which is an improvement of the LxF scheme by replacing the grid speed $\Delta r/\Delta t$ by a physical speed S (LeVeque, 2002). It can be defined as

$$S_{i+1/2}^{+} = max(|u_i| + c_{s_i}, |v_{i+1}| + c_{s_{i+1}}) \tag{15}$$

$$S_{i+1/2}^{+} = max_i(|u| + c_s). \tag{16}$$

The first choice is the maximum local fluid speed within the the cells i and i + 1 composing the intercell surface i + 1/2. It is derived from the method by Davis (1988), but is a more robust scheme. The second choice considers the maximum fluid speed in the total spatial domain and differs slightly from the LxF flux scheme.

See section 5 for numerical issues and differences between the LxF and Rusanov flux scheme, respectively.

1.3.3. Godunov Splitting

The idea to solve the conservation laws with source terms is to use either unsplit methods or fractional step (splitting) methods (LeVeque et al., 1998). I will neglect the first one and present some simple splitting methods. The general approach is to split the differential equations into two subproblems. At first, we solve the pure advection problem without any source terms (homogeneous form of Eq.10) resulting in the solution $\widetilde{U}_i^{n+1}$. Then, we use this solution to solve the system of ordinary differential equations dU/dt = S(t,U). In words, the change of U in time is equal to the integrated sources (Gravity, drag force, etc.). The Godunov time splitting method in conservative form for solving the conservation equations with source terms is therefore defined as

$$\widetilde{U}_i^{n+1} = U_i^n + \frac{\Delta t}{\Delta r}[F_{i-1/2} - F_{i+1/2}] \tag{17}$$

$$U_i^{n+1} = \widetilde{U}_i^{n+1} + \Delta t \cdot S(U)_i \tag{18}$$

where S(U) is the source term vector and F in the square brackets is the numerical flux obtained by the LxF or Rusanov flux scheme (so, $\mathrm{F_{i+1/2}} = F_{i+1/2}^{Rusa}$ or $\mathrm{F_{i+1/2}} = F_{i+1/2}^{LxF}$). This method is first-order accurate, that is, the error is linearly proportional to the time step Δt.

1.3.4. Strang Splitting

The strang splitting method (Strang, 1968) is similar to the Godunov splitting, but the first subproblem (in this case the ordinary differential equation for the source term) is solved over only a half time step. The resulting data is then used to solve the second subproblem over the full time step, and finally take another half time step to advance the solution of the first subproblem (LeVeque, 2002). The Strang splitting in conservative form is written as

$$\widetilde{U}_i^{n+1/2} = U_i^n + \frac{\Delta t}{2} \cdot S(U)_i \tag{19}$$

$$U_i^{n+1/2} = \widetilde{U}_i^{n+1/2} + \frac{\Delta t}{\Delta r} \cdot [F_{i-1/2} - F_{i+1/2}] \tag{20}$$

$$U_i^{n+1} = U_i^{n+1/2} + \frac{\Delta t}{2} \cdot S(U)_i. \tag{21}$$

While Strang splitting is second-order accurate, it is often sufficient to use the simpler and more efficient Godunov splitting method (see LeVeque (2002) for further details).

1.3.5. Time Step and Courant–Friedrichs–Lewy Condition

In order to calculate the time steps Δt, the Courant-Friedrichs-Lewy condition (CFL; named after Richard Courant, Kurt Friedrichs, and Hans Lewy) must be considered. We obtain

$$\Delta t = \frac{c_{cfl} \cdot \Delta r}{c_s + u_{gas,max}} \tag{22}$$

where c_{cfl} is the Courant number and $u_{gas,max}$ is the maximum gas speed within the total spatial domain. Thus, the denominator describes the largest possible wave speed. The Courant number must be $0 \leq c_{cfl} \leq 1$ for stable results. This means that no wave can propagate more than the cell size Δr in time Δt (Toro, 1999). Furthermore, the time steps are larger for a larger value of c_{cfl} resulting in incorrect solutions. The next point in time is then simply calculated by t = t + Δt.

1.4. Boundary Conditions and Ghost Cells

Ghost cells are crucial for simulations and have large impact on the result. As mentioned above, ghost cells are essential to calculate the parameters of *all* grid cells and intercell surfaces within the spatial domain. The following boundary conditions for these ghost cells are considered, particular attention should be paid for reflecting and infall boundaries.

1.4.1. Reflecting Boundary

A reflecting boundary is used for the inner ghost cell (indicated by U_0 in Fig.2) in order to conserve the physical parameters within the simulation. This is realized by using the physical parameters of the innermost cell U_1 for ghost cell U_0, that is,

$$U_0 = U_1 \qquad u_0 = -u_1 \tag{23}$$

which is an adoption of density and the value of velocity, but with an opposite sign for the velocities u to 'reflect' inwards propagating waves outwards. Issues may occur when the LxF scheme is applied in simulations with reflecting boundaries because the LxF scheme decouples even and odds terms. Thus, modified reflecting boundaries may lead to better results.

1.4.2. Modified Reflecting Boundary

The modified reflecting boundary is quite similar to the reflecting boundary, but with a velocity $u_{i+1} = 0$ m s^{-1} vanishing the velocities in the center of the simulated filament resulting in minor differences in density and velocity (in some particular cases oscillations in the velocity profile occur when using reflecting boundary).

$$U_0 = U_1 \qquad u_0 = 0 \tag{24}$$

1.4.3. Non-Reflecting Boundary

A non-reflecting boundary is also used in the inner ghost cell and leads to a loss of the physical quantities. Inwards propagating waves will cross the inner boundary at r = 0 without a response of information for the innermost grid cell. In other words, the boundary absorbs the incoming wave. This boundary is realized by

$$U_0 = U_1 \tag{25}$$

Thus, simulations with a non-reflecting boundary can not provide a growing density profile.

1.4.4. Outflow Boundary

The outflow boundary in the outer ghost cell U_{i+1} is the equivalent to the non-reflecting boundary , where all quantities are conserved in the ghost cell with

$$U_{i+1} = U_i \tag{26}$$

leading to a loss of information.

1.4.5. Infall Boundary

The infall boundary is used in the outer ghost cell and provides material from the outside with

$$\rho_{i+1} = const. \qquad v_{i+1} = -const. \tag{27}$$

leading to an increase of the density in the outer cell with a negative velocity (velocity towards the center). The infall boundary was applied to supply the simulation with material and ensure a growing density profile. The infall is then stopped at a certain central density allowing the development of an equilibrium state. This was realized by changing the outer ghost cell to reflecting boundary.

2. Code and Implementations

I have developed an one-dimensional hydrodynamical *FORTRAN 90* code to simulate the radial profile of filaments in molecular clouds. The code is subdivided into 19 subroutines considering the approaches explained in chapter 1. Furthermore, it is using SI base units: meter for length, kilogram for mass, second for time, kelvin for temperature, and mole for the amount of substance, allowing the application of constants in SI units, for instance, gravitational constant in m^3 kg^{-1} s^{-2}. The most important subroutines are cited in the appendix. Initial conditions for gas and dust and the choice of different schemes are managed by the data files `initial.ini` and `dust.ini`. Output files are marked with the extension `.out`. Furthermore, the code is using double precision to carry out high accurate calculations. Beside the approaches introduced in chapter 1, further sources must be considered. I have considered gravity, centrifugal forces, and drag between dust and gas in the simulations. This chapter is concerned with their implementation. Note that these sources are considered as forces per unit mass.

2.1. Gravity

It is not surprising that gravity is the most important force for the evolution of the filament depending on the initial configuration. It is implemented by introducing the linear mass M_{lin}, or mass per unit length, of the isothermal filament. It is expressed by

$$M_{lin}(r) = \int_0^r 2\pi r \rho(r) dr \tag{28}$$

$$\nabla\Phi(r) = -\frac{2GM_{lin}(r)}{r} \tag{29}$$

where the negative sign determines that the force is directed towards the center of the filament (first cell). Additional components, for instance dust components, must be considered in the calculation of the linear mass, i.e. ρ in Eq.28 is the sum of gas and dust densities.

2.2. Rotation

Rotation is considered by adding the centrifugal force of a rigid body to the source term of the momentum equation. That is,

$$F_z(r) = \rho(r)\omega^2 r \tag{30}$$

where ω is the rotational frequency and is r the radial distance to the center.

2.3. 2-Phase Model and Drag Force

The two-phase model connects the motion of the gas with that of dust and results in a force acting on the gas and dust, respectively. This force is called drag force and is adopted by Miniati (2010), where

$$\mathbf{S}(\mathbf{U}) = \begin{pmatrix} 0 \\ -\rho_g \kappa_g [u_g - u_d] \\ -u_g \rho_g \kappa_g [u_g - u_d] \end{pmatrix}_{Gas} \tag{31}$$

represents the source term vector of the gas component experiencing a drag force due to differences in the gas and dust velocity. The opposite force is exerted by the gas on the dust grains, where

$$\mathbf{S}(\mathbf{U}) = \begin{pmatrix} 0 \\ -\rho_d \kappa_d [u_d - u_g] \\ 0 \end{pmatrix}_{Dust} \tag{32}$$

$$\kappa_g = \kappa_0 \rho_d c_s \qquad \kappa_d = \kappa_0 \rho_g c_s \qquad \kappa_0 = \rho_{dg}^{-1} s^{-1}$$

with the drag coefficients κ_d and κ_g defined by the dust grains size s, dust grain density ρ_{dg}, and sound speed c_s. According to these equations, an exchange of momentum is constituted only between gas and individual dust components, the interactions between individual dust species are neglected.

2.4. Full Set of Equations

Here is a conclusion for an one-dimensional isothermal system including one gas and three dust components and all implementations mentioned above. It is written as

$$\mathbf{U} = \begin{pmatrix} \rho_g \\ \rho_g u_g \\ \rho_{d_1} \\ \rho_{d_1} u_{d_1} \\ \rho_{d_2} \\ \rho_{d_2} u_{d_2} \\ \rho_{d_3} \\ \rho_{d_3} u_{d_3} \end{pmatrix} \qquad \mathbf{F}(\mathbf{U}) = \begin{pmatrix} \rho_g u_g \\ \rho_g u_g^2 + \rho_g c_s^2 \\ \rho_{d_1} u_{d_1} \\ \rho_{d_1} u_{d_1}^2 \\ \rho_{d_2} u_{d_2} \\ \rho_{d_2} u_{d_2}^2 \\ \rho_{d_3} u_{d_3} \\ \rho_{d_3} u_{d_3}^2 \end{pmatrix}$$

$$\mathbf{S}(\mathbf{U}) = \begin{pmatrix} 0 \\ \rho_g(\Phi + \omega^2 r) - \rho_g \kappa_g([u_g - u_{d_1}] + [u_g - u_{d_2}] + [u_g - u_{d_3}]) \\ 0 \\ \rho_{d_1}(\Phi + \omega^2 r - \kappa_{d_1}[u_{d_1} - u_g]) \\ 0 \\ \rho_{d_2}(\Phi + \omega^2 r - \kappa_{d_2}[u_{d_2} - u_g]) \\ 0 \\ \rho_{d_3}(\Phi + \omega^2 r - \kappa_{d_3}[u_{d_3} - u_g]) \end{pmatrix} \tag{33}$$

where the geometric source term is neglected (see section 5 and discussion), and

$$\mathbf{U}_t + \mathbf{F}(\mathbf{U})_r = \mathbf{S}(\mathbf{U}).$$

According to the momentum equation in Eq.33, an equilibrium between pressure and self-gravity (first of all without rotation) can be established when the gas velocity u vanishes. Thus, the momentum equation can be simplified and leads to the equation of the hydrostatic equilibrium in the form of

$$\nabla\Phi = \frac{1}{\rho}\nabla P. \tag{34}$$

3. Initial Conditions

My initial conditions for the simulations consisted of a radial distribution of 0.5 pc with a resolution of 2000 cells resulting in a grid cell length Δr = 2.5·10^{-4} pc. The initial gas density was set to 1.34·10^{-18} kg m^{-3} (=400 cm^{-3}) when infall from the outer ghost cell was applied. This corresponds to the mean density of 100 cm^{-3} up to 1000 cm^{-3} (Solomon et al. (1987); Ferrière (2001)) in molecular clouds. Model simulations without infall were primarily performed with an uniform initial density of 10^{-17} kg m^{-3} to provide central densities similar to those with infall. Infall simulations were performed with an infall density and (subsonic) velocity of $\rho_{inf} = 10^{-18}$

kg m^{-3} and v_{inf} = -190 m s^{-1}, respectively. A few simulations were performed with a discontinuity at r = 0.25 pc to investigate the effect of different initial distributions. The initial gas and dust velocity was set to v = 0 m s^{-1} and a gas temperature of T = 10 K was assumed (Benson and Myers, 1989). Furthermore, I supposed an isothermal system of molecular hydrogen by using an adiabatic index $\gamma = 1$. In particular, I assumed a gas mixture of molecular hydrogen and Helium with an Helium abundance of 10%, as already mentioned above. As it turned out during the first trial runs, the best results were provided by simulations with the LxF flux scheme and Godunov splitting method, and a reflecting boundary for the inner ghost cell. In few cases the Rusanov scheme was used to avoid small oscillations in the velocity profile. Three dust species with sizes of 0.1, 1.0 and 10.0 μm and an uniform density of 2400 kg m^{-3} were assumed. These relatively large dust grains (compared to a typical dust size of $\leq$0.3 μm for silicates and $\leq$0.9 μm for carbonaceous dust grains, see Weingartner and Draine (2001)) were considered to provide a clear decoupling between gas and large dust grains.

4. Synthetic Spectra

Synthetic spectra for the different models were developed with a *Python* code (see appendix for full source code) to potentially compare them with observed filaments and derive their dynamical state during the filament's evolution. For this purpose, the output of the one-dimensional hydrodynamical code (U_1, U_2, U_3, ...) is rotated around the axis of rotation of the filament (cylindrical symmetry) inducing a shell-like structure as illustrated in Fig.3. Each shell exhibits an explicit velocity vector $\mathbf{u}$ (illustrated by grey arrows) pointing towards the center of the filament (because of the assumed symmetry of the problem). The projected velocities $\mathbf{v_P}$ along the line of sight (black arrows) were calculated with trigonometric functions and the center of each shell (in terms of the line of sight) is defined as the initial point for the individual velocity vectors. This approach was applied for one half of the filament and is then mirrored for the second half, but with inverse sign for gas velocities. These projected velocities were then used to calculate the spectra. Two gas species were considered, $C^{18}O$ and N_2N^+. $C^{18}O$ becomes excited at $\sim 5 \cdot 10^2$ cm^{-3} (equal to $1.67 \cdot 10^{-18}$ kg m^{-3}), and depletes at $5 \cdot 10^4$ cm^{-3} (equal to $1.67 \cdot 10^{-16}$ kg m^{-3}). N_2H^+ becomes excited at densities greater than 10^4 cm^{-3}, or $3.35 \cdot 10^{-17}$ kg m^{-3}, and remains in the gas phase for at least one order of magnitude. This should be considered as first order approach, for a more detailed comparison a full radiative transfer code is needed. The spectra were obtained by calculating the intensity $I(v_P)$ of a specific emission line with

$$I(v_P) = \sum_i I_0 \cdot exp\left(-\frac{(v_P - v_i)^2}{2\sigma^2}\right)\left(\frac{n_i}{n_0}\right)^{\alpha} \tag{35}$$

where $I_0 = 1$ is the intensity of an individual shell contributing to the total intensity of a $C^{18}O$ or N_2N^+ line. Thus, the intensity is expressed in arbitrary units. The latter parenthesis describes the normalization of the column density of shell i by the

central column density n_0 of the filament, with $\alpha = 1$ for a linear normalization in case of densities close to the critical density, and $\alpha = 2$ for a squared normalization when densities are below the critical density. This is an approximation in order to simplify the problem. I have used a linear normalization for all spectra in this thesis. A thermal broadening of $\sigma = 200$ m s^{-1} (represented by a Gaussian distribution for each velocity vector) was chosen to imitate a gas with T = 10 K (Bodenheimer, 2011). The contribution of each shell to line of sight is calculated by

$$dy_i = \sqrt{(x+i)^2 - x^2} - \sqrt{(x+i-1)^2 - x^2} \tag{36}$$

where x represents the radius at which the line of sight is assumed (r_3 in case of Fig.3). Shells with densities beyond the range for $C^{18}O$ and N_2N^+ in the gas-phase were evaluated with dy = 0. The column density for each shell along the line of sight is then calculated by $n_i = dy_i \cdot \rho_i$, where i is an integer from 1 to n (number of cells). The maximum of *(x + i)* is equal to the number of cells n. The first term of Eq.36 is illustrated by, for instance, the green triangle and the second term by the yellow triangle in Fig.3. The full width half maximum (FWHM) was calculated for each gas species and the y-axes (normalized intensity) of each plot were divided by $3.9 \cdot 10^2$ to obtain values of order unity.

5. Accuracy and Numerical Issues

- **Main Problem: Geometric Source Term**
  According to the structural condition of an elongated, cylindrical filament a geometric source term is needed in one-dimensional simulations, otherwise the code would not "know" the geometry of the system. There are differences in the geometric source term for Cartesian, cylindrical and spherical coordinates, as described in section 1.2. Some trial simulations have shown that the system can not develop an equilibrium state when a geometric source term is used.

  The problem is the time splitting method that is applied on a quasi steady-state system, as it is discussed by LeVeque et al. (1998). Let us assume an initial hydrostatic equilibrium of the fluid and the splitting methods is applied. As explained in section 1.3, the first step of the splitting method solves the homogeneous conservation equations, that is, without any source terms. Differences in the density will then lead to an acceleration of the fluid. The second step considers the source terms, but it can not maintain the initial equilibrium state and the changes of these two steps will not exactly cancel out each other. An error is developed leading to a growing density profile in spite of the initial hydrostatic equilibrium. This problem can be solved by sophisticated methods as explained by LeVeque et al. (1998). In our case this issue was solved by omitting the geometric source term vector. A perfect Ostriker profile can be reproduced (see section 6.1). Notice that this problem arises only in situations very close to a steady state. In more dynamical situations, where velocities are

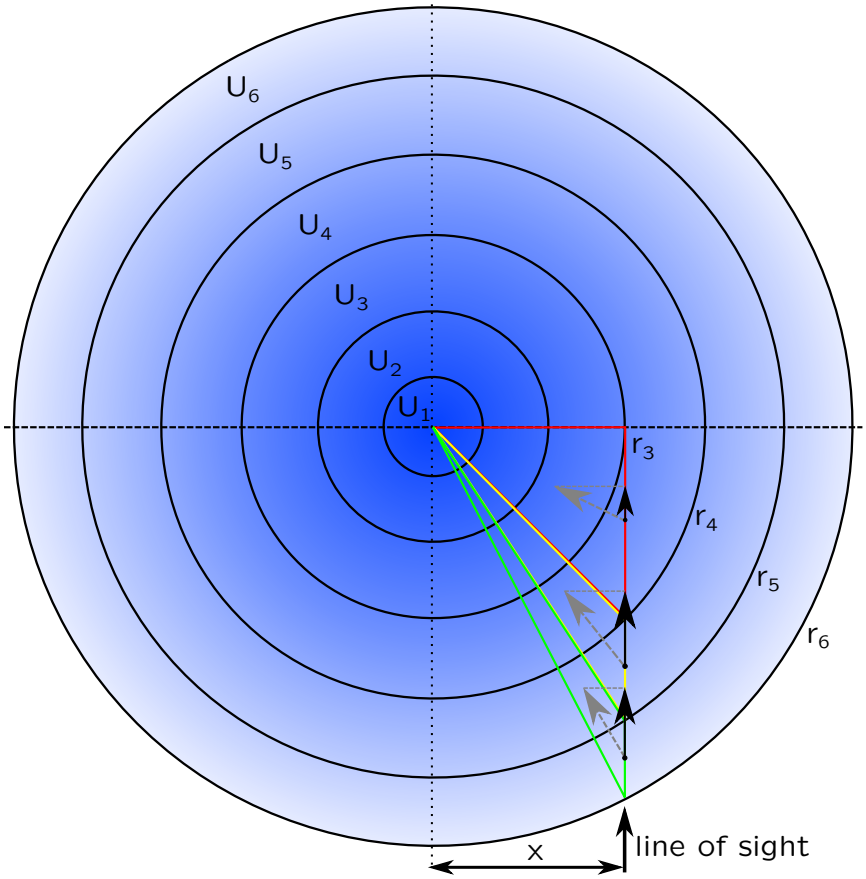

Figure 3: Illustration of the simulated filament resulting from the one-dimensional output (U_1, U_2,...) of the hydrodynamical code. The 2000 cells has been rotated about the center to obtain this two-dimensional shell-like model of a filament. The grey arrows represent the radial velocities for each cell, the black arrows illustrate the projected velocities along the line of sight. The blue background color imitates the density condensation towards the center. The velocities were calculated for the bottom half of the filament and were inverted for the upper half.

significantly larger than zero, the time splitting method in conjunction with geometric source terms is perfectly adequate and produces more accurate results.

- **Non-zero Gas Velocities**
  The velocity of gas in hydrostatic equilibrium must be $v_{equi} \equiv 0$ m s^{-1} (according to Eq.34), but simulations are not exact and large velocities or oscillations (see for instance Fig.23 or chapter 6.1) can be observed due to numerical issues. We therefore have to make a compromise by choosing a maximum permissible gas velocity insignificant for additional data analysis. A gas velocity smaller than 100 m s^{-1} was chosen arbitrarily and is supposed to be small enough to provide an adequate accuracy for subsequent development of synthetic spectra. In particular, simulations mostly show velocities between 10 and 40 m s^{-1}.

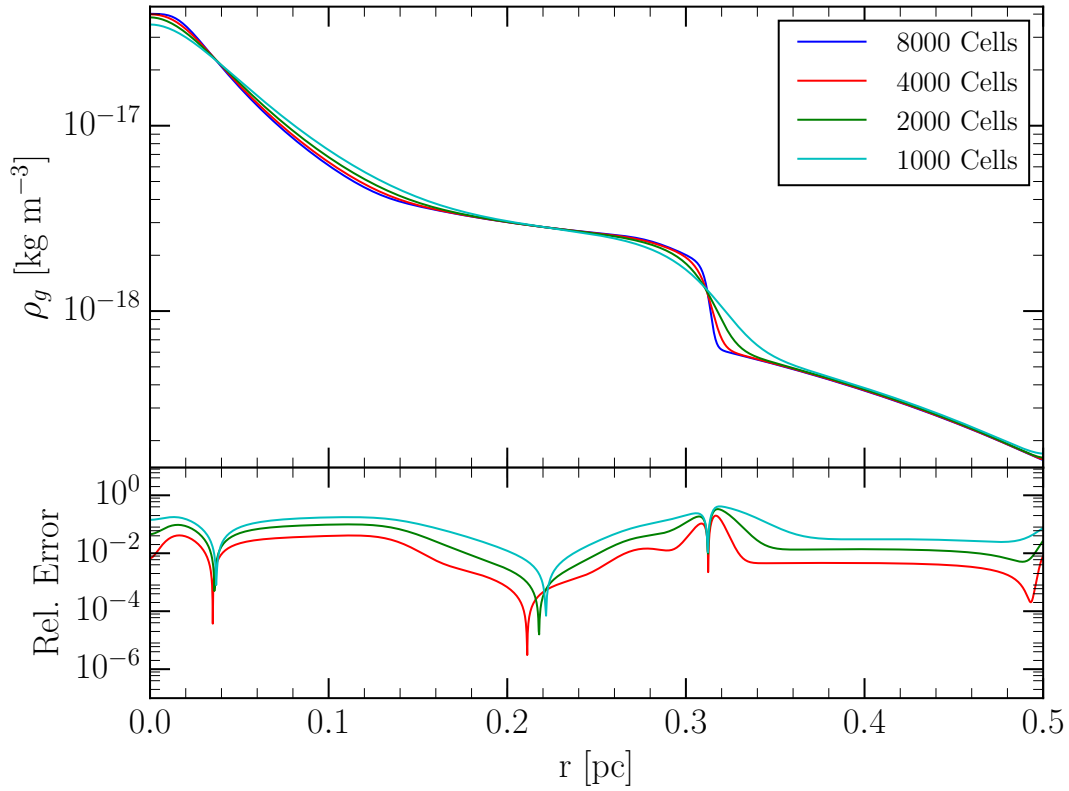

Figure 4: Top: Radial gas density profile of simulations with resolutions of 1000, 2000, 4000, and 8000 cells covering an area of $r_{max} = 0.5$ pc. Bottom: Error in % relative to the simulation with 8000 cells. The maximum occurs at the discontinuity at r $\approx$ 0.32 pc. For simulations in this thesis, 2000 cells covering an area of $r_{max} = 0.5$ pc is an adequate resolution.

- **Spatial resolution**
  The resolution of a simulation is given by the number of grid cells covering the total spatial domain. Differences in the density profile can be seen by using different number of cells. Simulations with a low cell number (for instance, 1000 grid cells for a spatial domain $r_{max} = 0.5$ pc) can indeed reach the hydrostatic equilibrium, but result in a narrower density profile compared to the analytical Ostriker profile. In this case, a break condition, where the simulation stops when the inner 1000 cells of the actual profile are equal to the corresponding Ostriker profile (within an error of 10%), can not be satisfied. Furthermore, differences during the simulation occur and are illustrated in Fig.4. The relative error is referred to the simulation with 8000 cells.

- **Lax-Friedrichs vs. Rusanov**
  Lax-Friedrichs scheme sometimes triggers strong oscillations in the velocity profile as it can seen in simulations with dust and non-zero infall velocity. The final velocity profiles then show non-zero velocities with large, high frequent oscillations, especially in the outer part of the profile. Thus, some simulations with infall were made with the Rusanov scheme.

6. Results

6.1. Numerical Ostriker Profile

A large number of simulations were performed to investigate the origin of filaments and their universal width, but the actual formation progress is still unknown and the results of these simulations should be considered carefully (see for instance Hennebelle (2013)). In this section, I investigated this universal width and initial conditions for self-gravitating, isothermal filaments without infall and compare the numerical results with the analytical Ostriker profile found by Ostriker (1964).

I started with simulations including constant gas density over the whole radius r_{max} = 0.5 pc covered by a resolution of 2000 cells and an initial velocity v_{ini} = 0 m s^{-1} to examine the properties and formation of numerical Ostriker profiles. Dust, rotation and infall were not included in these simulations. Reflecting boundaries were chosen for both inner and outer ghost cell and simulations stopped after 40 Myr (a period which is expected to be sufficient for developing an equilibrium profile). The investigation of the duration to establish an Ostriker profile is not the aim of this chapter.

ρ_{ini} [kg m^{-3}]	ρ_{fin} [kg m^{-3}]	n_{fin} [cm^{-3}]	FWHM [pc]	M_{tot} [$M_\odot$ pc^{-1}]	$M_{0.1}$ [$M_\odot$ pc^{-1}]
$1.0{\cdot}10^{-18}$	$1.5{\cdot}10^{-18}$	448	0.53	8.88	0.68
$5.0{\cdot}10^{-18}$	$2.9{\cdot}10^{-17}$	8667	0.14	15.92	7.44
$7.0{\cdot}10^{-18}$	**$5.6{\cdot}10^{-17}$**	**16736**	**0.10**	**16.59**	**10.17**
$8.0{\cdot}10^{-18}$	$7.3{\cdot}10^{-17}$	21817	0.09	16.62	11.22
$1.0{\cdot}10^{-17}$	$1.1{\cdot}10^{-16}$	32874	0.07	16.61	12.74
$5.0{\cdot}10^{-17}$	$2.5{\cdot}10^{-15}$	747146	0.02	17.53	17.40
$1.0{\cdot}10^{-16}$	$8.5{\cdot}10^{-15}$	2540298	0.01	19.25	19.24
$1.0{\cdot}10^{-15}$	$9.8{\cdot}10^{-14}$	29288139	$<$0.01	156.54	156.54

Table 2: Initial density, final density, FWHM, total mass and mass within 0.1 pc of simulations with constant density distribution over the whole radius. The emphasized filament shows a FWHM of 0.10 pc, the mean width (0.10±0.03 pc) of observed filaments (Arzoumanian et al., 2011).

The gas starts to compress under its own gravity until the hydrostatic equilibrium (Ostriker profile) is established. The results for different initial densities are listed in Table 2 and illustrated in Fig.5. The black lines illustrate the analytical Ostriker profiles for a given central density calculated by Eq.2 . It can also be seen that the accuracy in terms of density (compared to the analytical Ostriker profile) decreases with increasing initial density, primarily in the outer region (magenta line at r $\geq$ 0.05 pc in Fig.5). It should be mentioned that the analytical Ostriker profiles are always the same in normalized units, but shows different profiles in physical units due to different ρ_0 and the changes of H (see Eq.2 in part I). The final gas velocities of the first five filaments in Table 2 are well below an absolute value of 40 m s^{-1} and show density profiles consistent with the analytical Ostriker profile, while filaments with $\rho_{fin} \geq 2.5{\cdot}10^{-15}$ kg m^{-3} exhibit velocities up to 300 m s^{-1} and show strong oscillations in the evolution of the central gas density (not shown here). This

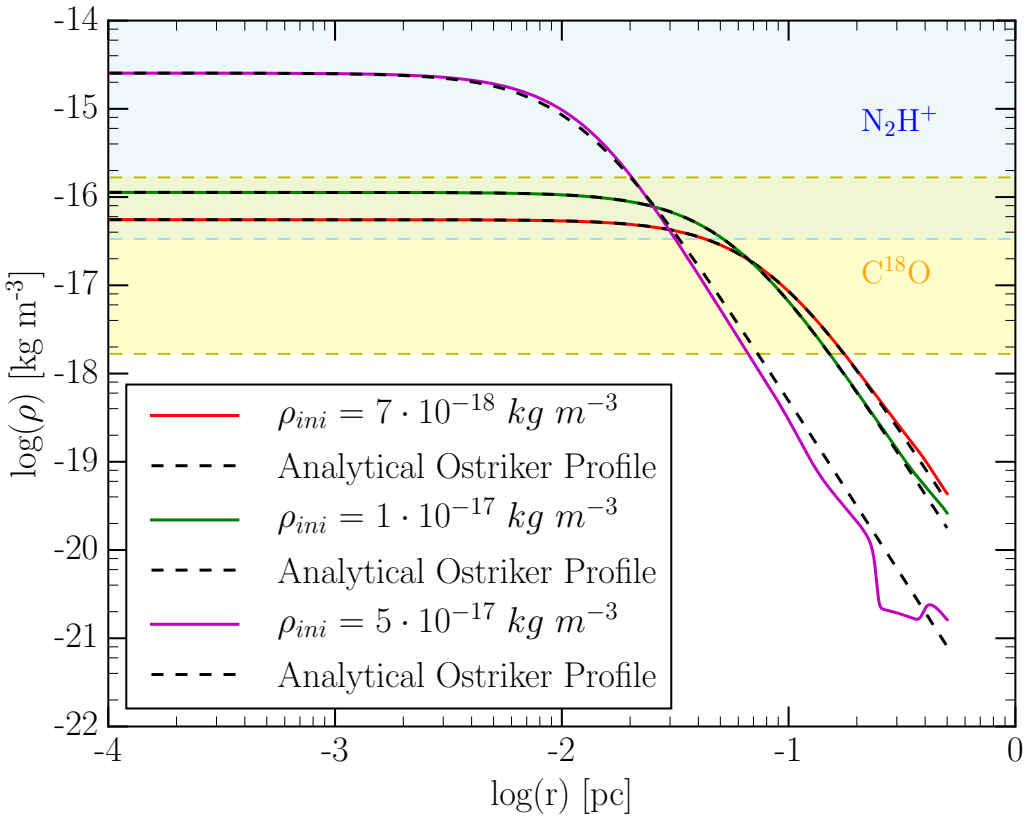

Figure 5: Three final density profiles in equilibrium for T = 10 K and different initial densities listed in Table 2. According to the central density of these profiles, the black dashed lines indicate the corresponding analytical Ostriker profiles calculated by Eq.2. The yellow area indicates densities where $C^{18}O$ becomes excited and the blue area illustrates the N_2H^+ excitation. Simulations with larger central densities exhibit a narrower density profile and show small deviations from the analytical Ostriker profile (e.g. magenta line at r $\geq$ 0.05 pc).

is either a numerical issue or filaments with a large initial density can not establish an equilibrium and oscillate. A filament with a full width half maximum (FWHM) of 0.1 pc (as found by Arzoumanian et al. (2011), who identified an universal width of 0.10±0.03 pc for observed filaments but for a Plummer-like density profile with an exponent of 1.5 > p > 2.5) can be developed by an initial gas density of $7{\cdot}10^{18}$ kg m^{-3} in a cylinder with r = 0.5 pc. Nevertheless, I did not find an universal width for isothermal, self-gravitating filaments without infall and different initial densities. Simulations with higher initial density exhibit a radial width remarkable smaller than 0.1 pc, and simulations with smaller initial density establish broad profiles with a FWHM of ∼0.5 pc. There is an initial density of at least $(9{\pm}2){\cdot}10^{-18}$ kg m^{-3} needed to constitute a profile with a width of 0.1±0.03 pc.

6.2. Simulations with Rotation

Rotation may effect the filament and I tried to investigate its effect on the radial density profile in equilibrium. The implementation of rotation was realized by adding the centrifugal force to the source term (see section 2.2 and listing 2 in appendix). A rotational frequency of $\omega = 6.5{\cdot}10^{-14}$ s^{-1} was adopted by Recchi et al. (2014), but I did not find results with $\omega \leq 3.57{\cdot}10^{-14}$ s^{-1} differing highly from the non-rotational case. Differences in density can primarily be seen in the outermost parts of these profiles, with gas velocities up to 500 m s^{-1}, as shown in Fig.6 (light and dark green, dashed curves). That is, an equilibrium can not be found for isothermal filaments with constant rotational frequency. The central gas density slightly oscillates around a constant density, but do not increases as it should with these high gas velocities towards the center. The red line illustrates the analytical Ostriker profile. Larger values of ω yield profiles ending at the outer part of the simulated region (illustrated by a blue, violet and cyan line), also for the value found by Recchi et al. (2014). Gas velocities are illustrated in the bottom panel of Fig.6 and have values much greater than 100 m s^{-1}, the threshold for numerical issues (see section 5). Notice that rotating cylinders develop density oscillations in their outer parts, which are dynamically unstable (Hansen et al., 1976). In order to conclude these results, I can not find suitable results for a rotational frequency of $\omega \geq 3.58{\cdot}\ 10^{-14}$ s^{-1}, the rotation is too strong for a stable profile to settle down at the center of the filament. On the other hand, smaller rotational frequency leads to a density decrease in the outer part of the filament, a part which is not attractive for observations. Further discussion can be found in section IV.

6.3. Simulations including Two-Phase Model

The evolution and behavior of gas and dust during the star formation process is still not clear and crucial for the understanding of the star formation process. There are numerous models to explain the transition from diffuse low-density gas to dense cores. These models are important for a comparison with observations. Beside gas, dust is a very crucial participant and is in these simulations considered by the implementation of the two-phase model explained in section 2. In this section, I will present the results of the two-phase implementation. For that, I have performed a total of five simulations with different initial distributions of gas and dust to analyze their differences, the evolution from diffuse gas to dense cores, and the effect of dust on gas. This is the main goal of this section.

6.3.1. The Setup

The general types of initial distributions for gas and dust are illustrated in Fig.7. Case 'a' describes a molecular cloud without overdensities, that is, a constant distribution over the total simulated radius r_{max}. It must collapse under its own gravity until the equilibrium is accomplished. This reflects the evolution from an initial low-density cloud to a stable filament. Case 'b' shows a discontinuity in both gas and dust density, for instance at r = 0.25 pc, with a lower density in the outer part. Case 'b' mimics an initial filament of dense gas (with constant density) already

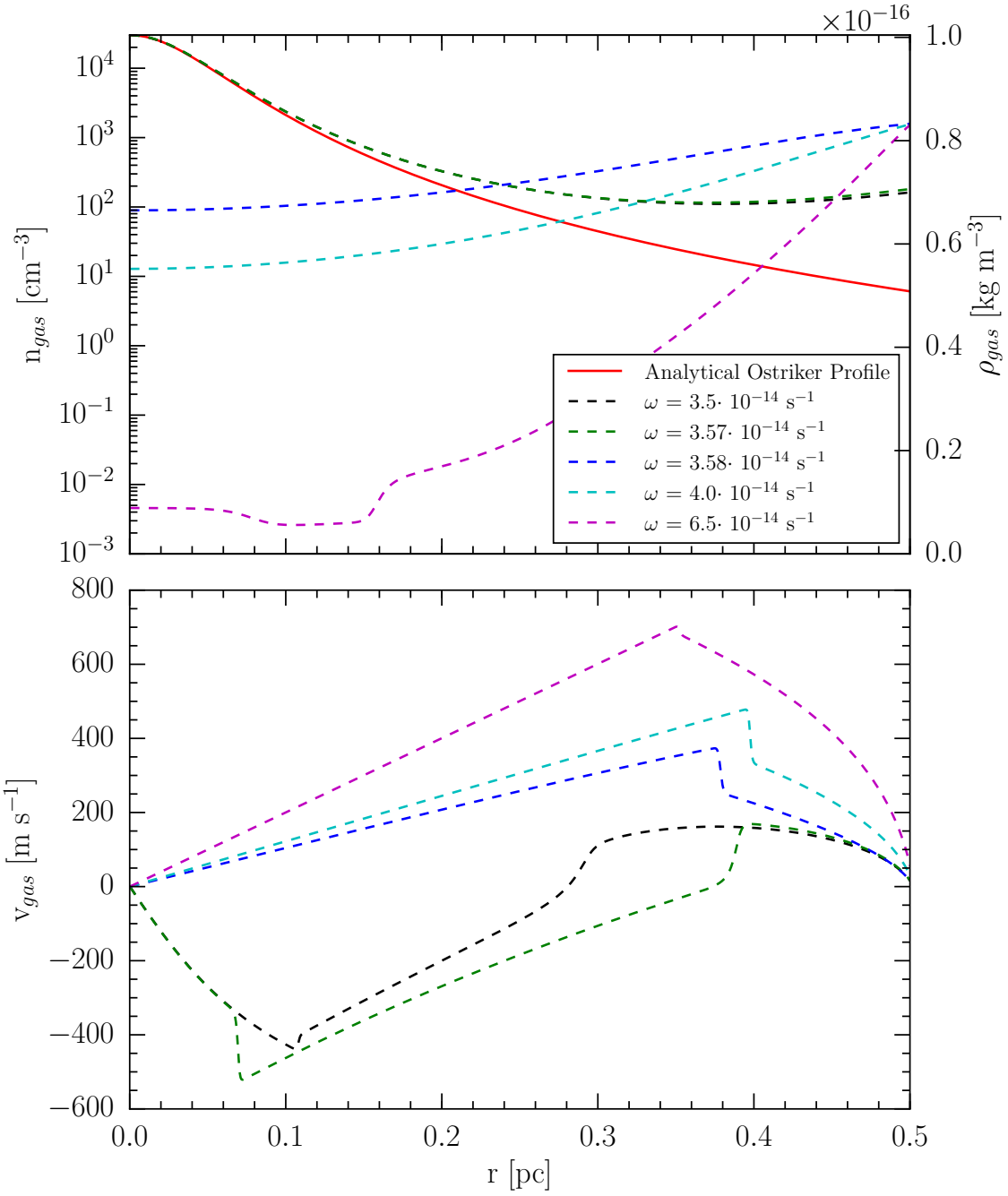

Figure 6: Top: Radial density profiles of filaments with different rotational frequencies ω (dashed lines) and the analytical Ostriker profile (red line) for comparison. Bottom: Corresponding velocities. The transition is between $3.57 \cdot 10^{-14}$ s^{-1} and $3.58 \cdot 10^{-14}$ s^{-1}.

formed by processes mentioned in the introduction (for instance supersonic turbulence), and surrounded by low-density gas. This initial filament is not arranged in an equilibrium phase and must evolve until it reaches an equilibrium configuration. In this section, I will examine the evolution of these configurations. All simulations in this chapter were performed with 2000 cells covering a region of $r_{max} = 0.5$ pc, and reflecting boundaries in the central ghost cell (see section 1). The initial gas density is equal to $\rho_g = 1.34 \cdot 10^{-18}$ kg m^{-3} (equivalent to 400 cm^{-3}, noted as 'default

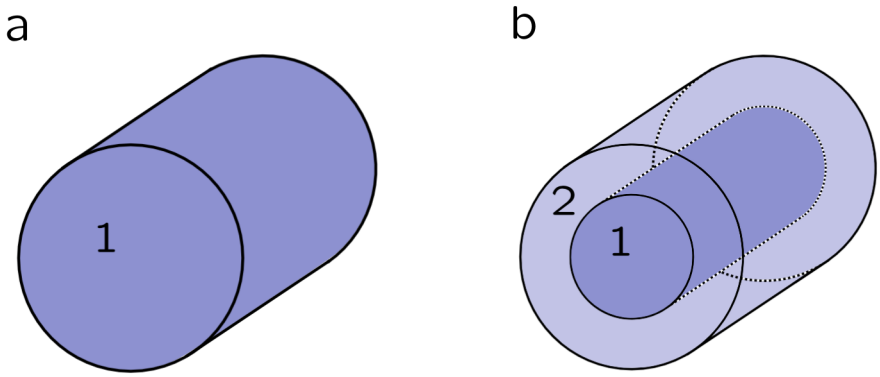

Figure 7: 3D illustration of the basic initial distributions for gas and/or dust in simulations presented in section 6.3. The color is comparable with the density in this region. Light blue (b2) indicates a low density region while dark blue illustrates a region with high density (a1 and b1). Region b1 is noted as 'inner region' while b2 is defined as 'outer region'.

value'), except for the initial filament setup where the density is increased. Each infall simulation was performed with an outer infall boundary including an infall density and velocity of $\rho_{\mathrm{infall}} = 10^{-18}$ kg m^{-3} and $v_{\mathrm{infall}} = -190$ m s^{-1}, a subsonic velocity in clouds with T = 10 K. This was done in order to avoid the formation of shocks due to supersonic infall. By reaching a central density of $9 \cdot 10^{-17}$ kg m^{-3} the outer boundary is changed to reflecting to prevent further infall from the ghost cell and ongoing growth of the density profile. This provides the formation of an equilibrium state (Ostriker profile). Gas and dust are coupled by the scheme presented in section 2.

The effect of the dust on the gas is explained in section 6.3.2 where I compare simulations including dust and simulations without dust. The initial density distribution is illustrated by case 'b' in Fig.7. The initial gas density in the inner region exhibits the default value while it is reduced by a factor 100 in the outer region. The gas-to-dust ratio $\rho_{\mathrm{g}}/\rho_{\mathrm{d}}$=100 remains constant over the whole region (the discontinuity, therefore, occurs in both dust and gas).

Furthermore, in order to investigate the evolution of different configurations in detail I will present four individual simulations in section 6.3.3, noted as model (1), (2), (3) and (4) where (1), (3) and (4) represents case 'b' while case 'a' is used only in simulation (2). An extensive analysis of the gas-to-dust ratio is followed in section 6.3.4. Here is the detailed setup for each of these simulations.

Model (1): The dust density of each species has been set to $\rho_{\mathrm{d}} = 1.34 \cdot 10^{-19}$ kg m^{-3} in the outer part and is reduced by a factor of 100 in the inner part where the gas density retains the default value of $\rho_{\mathrm{g}} = 1.34 \cdot 10^{-18}$ kg m^{-3}. Gas density in the outer part is reduced by a factor of 100 (case 'b') resulting in a gas-to-dust ratio < 1. This was carried out with an infall velocity of -190 m s^{-1} (Model 1a). Moreover, I performed the same setup without infall (Model 1b) and increased initial gas density $\rho_{\mathrm{g}} = 1.7 \cdot 10^{-17}$ kg m^{-3} to provide an evolution and final density comparable with

the infall simulation, and to analyze the differences between infall and simulations without infall.

Model (2): describes a simulation including constant gas and dust density (case 'a') over the whole simulated area with default gas density and ρ_g/ρ_d=100. It illustrates the evolution from an undisturbed molecular cloud to a filament in equilibrium.

Model (3): characterizes a simulation with supersonic infall. The infall velocity has been increased to v = -1000 m s^{-1} and the discontinuity has been set to r = 0.4 pc instead of 0.25 pc (modification of case 'b') to ensure a significant impact of the supersonic infall on the discontinuity. This infall velocity is ∼5x larger than the sound speed. The total initial dust density in the inner part has been set to ρ_d = $1.34 \cdot 10^{-21}$ kg m^{-3} (resulting in a gas-to-dust ratio of 10^3) and is increased in the outer 0.1 pc by a factor of ∼330 to ensure large differences in the gas-to-dust ratio and consequently in the coupling between gas and dust. I used the default value for the gas density in the inner part and reduced it in the outer part by a factor of 100. Hence, the dust density in the outer part is larger than the gas density resulting in a gas-to-dust ratio of ∼0.03 to show how the dust evolves under the effect of supersonic infall and low gas-to-dust ratio. We will see that this configuration in the outer part is rapidly destructed by the supersonic infall.

Model (4): also illustrates an initial filament (case 'b') with constant gas and dust density up to 0.25 pc surrounded by low density gas and dust while the gas-to-dust ratio is constant over the whole region (compared to the previous models where the gas-to-dust ratio is not constant). I increased the infall density to $\rho_{g,infall} = 6.67 \cdot 10^{-18}$ kg m^{-3} and density in the inner region to $\rho_{g,initial} = 3.35 \cdot 10^{-18}$ kg m^{-3} (= 1000 cm^{-3}, see No. 24 of Table 4) to ensure a fast evolution comparable with the lifetime of observed filaments. The outer gas and dust density was set to 1/100 of the density in the inner region. A complete list of the setup and final quantities of these four models are summarized in Table 3. A detailed presentation of the results can be found in section 6.3.3.

6.3.2. Result: The Effect of the Dust on the Gas

Significantly small dust particles, for instance 0.05 μm, and small gas-to-dust ratios (e.g. high dust density) have marginal impact on the evolution of the gas density and velocity due to the gas-dust coupling. I have tested this with simulations including infall (see setup section for further details) and is shown in Fig.8. This effect does not rise with time since the small gas-to-dust ratio will be balanced by infalling material with normal dust-to-gas ratio. For the widely used ratio of ρ_g/ρ_d=100 the effect of the back-reaction exerted by the dust particles on the gas can be neglected. We will, however, see in the next subsections that the gas-to-dust ratio is spatially (but also in time) not constant and may become very large. This could have a small impact on the gas profile.

Model	(1a)	(1b)	(2)	(3)	(4)
Distribution	D	D	U	D	D
$\rho_{g,ini}$ [kg m^{-3}]	$1.34{\cdot}10^{-18}$	$1.70{\cdot}10^{-17}$	$1.34{\cdot}10^{-18}$	$1.34{\cdot}10^{-18}$	$3.35{\cdot}10^{-18}$
$\rho_{g,fin}$ [kg m^{-3}]	$9.92{\cdot}10^{-17}$	$9.92{\cdot}10^{-17}$	$9.88{\cdot}10^{-17}$	$5.77{\cdot}10^{-17}$	$3.71{\cdot}10^{-16}$
$v_{g,max}$ [m s^{-1}]	-649.07	-529.49	-515.78	-1180.89	-914.83
v_{infall} [m s^{-1}]	-190	-	-190	-1000	-190
ρ_{infall} [kg m^{-3}]	$1.00{\cdot}10^{-18}$	-	$1.00{\cdot}10^{-18}$	$1.00{\cdot}10^{-18}$	$6.67{\cdot}10^{-18}$
Infall phase [Myr]	4.80	0.60	4.80	1.00	1.20
Infall time [Myr]	19.85	-	18.50	3.32	0.29

Table 3: A summary of the four models. Model (1a) is referred to the simulation with infall, (1b) to the same simulation without infall. Model (2) describes the simulation with an uniform gas distribution, model (3) a simulation with supersonic infall, and model (4) represents an initial filament. The infall time is the time where the infall boundary is changed to reflecting boundary to prevent further infall. U refers to an uniform gas distribution, D to a distribution with a discontinuity.

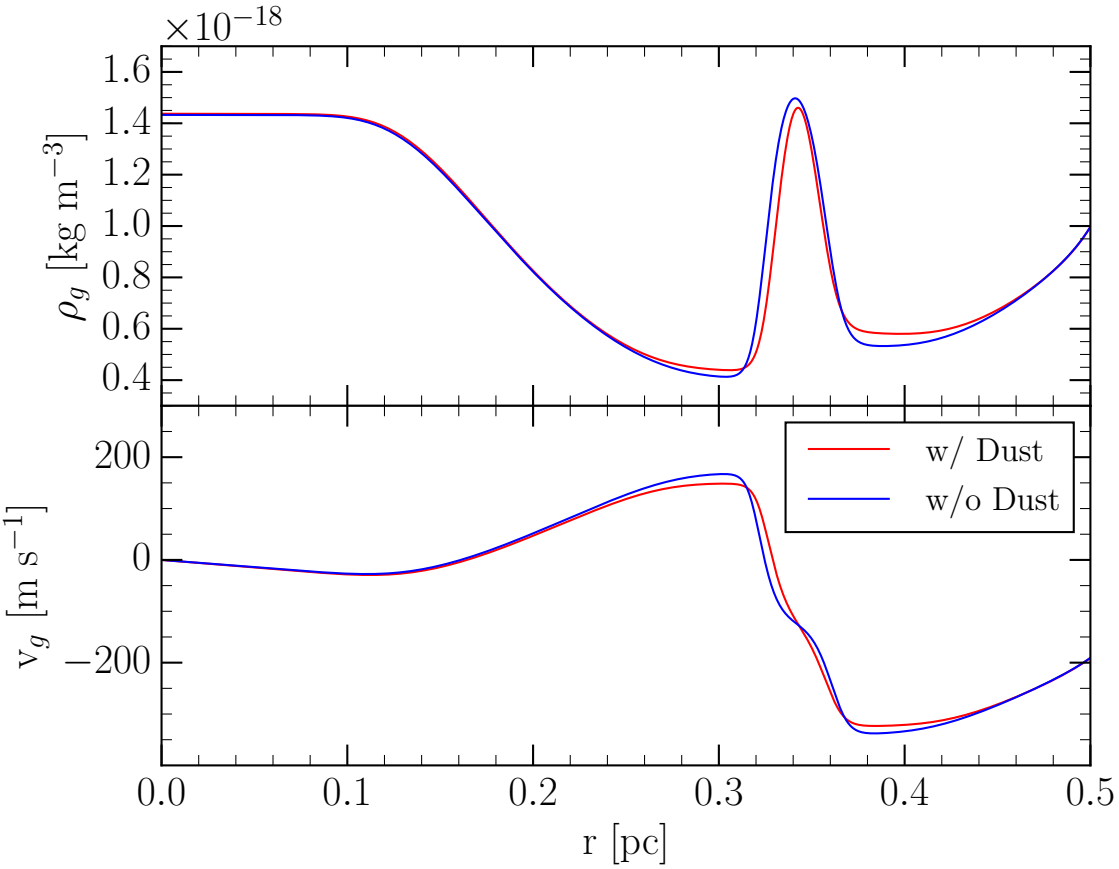

Figure 8: The effect of small (0.05 μm) dust grains on the gas is showing neglecting differences in the gas profile. Gas density profile in the upper panel and appropriate velocities in the lower panel. The simulations were performed with 2000 cells.

6.3.3. Result: Evolution of Gas and Dust

The general evolution of a model corresponding to case 'b' (regardless of the setup in detail) always shows a rarefaction wave evolving from the discontinuity towards the center while the 'shock' (for instance, at r $\simeq$ 0.3 pc in Fig.10 or Fig.14) is moving outwards. This shock is then colliding with the infalling accretion wave within the outer region (for instance, at r $\simeq$ 0.35 pc and t = 0.36 Myr in Fig.10) developing a peak in the gas density profile where small dust grains are captured therein. After this peak is evolved towards the center and stays in an equilibrium between gravity and pressure, the gas density profile is starting to evolve outwards. This is the beginning of the re-expansion phase. The evolution is consequently separated into an accretion phase and a re-expansion phase.

While large dust species are unaffected by the gas evolution during the re-expansion phase and thus remain in the center, very small grains follow the gas outwards. This results in a strong *separation between different dust species*. The reason is a different gas-dust coupling of individual dust grain sizes. Due to the friction between gas and dust, small dust grains adopt the gas velocity more efficiently than larger ones. Mathematically, the term $\kappa_0 = \rho_{\rm dg}{}^{-1} \cdot {\rm s}^{-1}$, where s is the dust grain size and $\rho_{\rm dg}$ the dust grain density, becomes very large for small dust grain sizes and densities resulting in a larger drag force. For large dust grains, this effect leads to a smaller transposition between gas and dust momentum.

The infall phase is the first stage of the evolution and ends when the density profile stops to evolve towards the center and starts to develop outwards. This is also the beginning of the re-expansion phase. The gas settling in equilibrium in the center in this phase is not moving outwards anymore, but the infalling gas broadens this region resulting in an outwards evolving profile which is also seen by the negative gas velocities beyond this central overdensity. The re-expansion phase ends when the profile has fully developed an hydrostatic equilibrium. The infall phase is not related to the actual infall (accretion) from the outer ghost cell. The infall phase can stops before the accretion is stopped.

The evolution of a constant gas and dust distribution over the whole simulated area, as it is graphically illustrated by case 'a', starts with very small drift velocities ($\approx$ same velocity for gas and dust) at the outer boundary - see e.g. Fig.12. The differences between gas and dust are small and depends on the gas-to-dust ratio and infall. Further evolution is equivalent to the re-expansion phase in case 'a'. Here is a detailed analysis of the individual models denoted as (1) - (4).

Model (1): Infall vs. No Infall

I have compared the influence of infall using model (1a) and (1b). The evolution of the infall simulation (1a) (infall stops at $\sim$20 Myr - see red line in Fig.9) is shown in Fig.10. The x-axis shows the radius while in the y-axes we plot the density in [kg m^{-3}], drift velocity in [m s^{-1}], and gas-to-dust ratio at different time. It should be noted that the y-axes show different ranges at different time steps. One tick on the x-axis is equivalent to 0.025 pc (or 100 cells). The differences with the results of the simulation without infall (model *1b*, illustrated in Fig.11) become noticeable primarily at large r. The infall modifies the density and velocity profiles beyond

the initial discontinuity. A striking difference between these setups is seen in the drift velocity. While the infall simulation (Fig.10) shows one negative and one positive velocity peak (due to the infall and formation of the outwards moving shock - see above), the simulation without infall features only one positive peak meaning that the gas is moving outwards relative to the dust. In both simulations, large dust grains (red lines) exhibit larger (negative) velocities with respect to small dust grains resulting in a larger, positive drift velocity due to the initial distribution and gas-dust coupling. Small dust species are captured in the outwardly evolving gas wave ('shock' at r $\simeq$ 0.25 pc during the first time steps shown in Fig.10 and Fig.11) showing a slower evolution towards the center in both infall simulations and without infall.

The final dust distribution of the small dust species (0.1 μm) is slightly more extended in case without infall. The minimum density threshold has been reached at 0.275 pc. Larger dust grains show negligible differences between these simulations (the minimum density threshold has been reached at 0.075 pc and 0.15 pc for intermediate and large grains), but both simulations show a similar and clear stratification of different dust species. The gas profiles in both simulations results in a nearly perfect Ostriker profile demonstrated by the cyan lines at t = 75 Myr. The central gas density at this time step is in both simulations about $\rho_g = 9.92 \cdot 10^{-17}$ kg m^{-3} (with a difference of $\sim 2 \cdot 10^{-20}$ kg m^{-3}). A faster evolution without infall can be explained by the higher mass (larger initial density and therefore larger gravitational pull towards the center) available during the whole evolution. In the infall simulation, the mass is slowly added from the outside and thus has no gravitational effect until it reaches the central region. Therefore, simulations without infall develop an equilibrium faster than with infall. It can also be seen that the dust is still moving inwards (velocities up to v_{dust} = -420 m s^{-1}) while the gas is in equilibrium state resulting in positive drift velocity, for instance, at t = 10 Myr in Fig.11 with gas velocities of $-10 \leq v_{gas}$ [m s^{-1}] ≤ 50 (probably due to numerical error). Similar drift velocities are also present in the infall simulation.

The evolution of the dust in these simulation is concluded as follows: In the infall phase dust is falling towards the center. The re-expansion phase forces the dust profile to evolve outwards until approximately the time when the gas has fully developed an equilibrium. Then, the dust is starting to evolve towards the center resulting in a narrower density profile in future time steps. It should be mentioned that the dust always exhibits negative velocities meaning that it is moving inwards at any time step. There are few cases where small dust grains (blue line) show positive velocities up to v_{gas} = 195 m s^{-1}, primarily at the beginning of the simulation where they are captured into the outwards moving shock. The final density profile is very similar in both simulations. Differences between infall and no infall can essentially be seen in the gas velocity. Infall simulations show higher gas velocity towards the center (negative velocity) than simulations without infall. On the other hand, infall simulations evolve much slower due to the smaller amount of mass. Furthermore, the infall simulation also features large positive velocities up to $v_{g,max}$ = 356 m s^{-1} at the beginning of the evolution while the simulation without infall shows a large (positive) velocity peak of $v_{g,max}$ = 224 m s^{-1} only after the transition between infall and re-expansion phase at t = 0.6 Myr when infalling gas seems to rebound out-

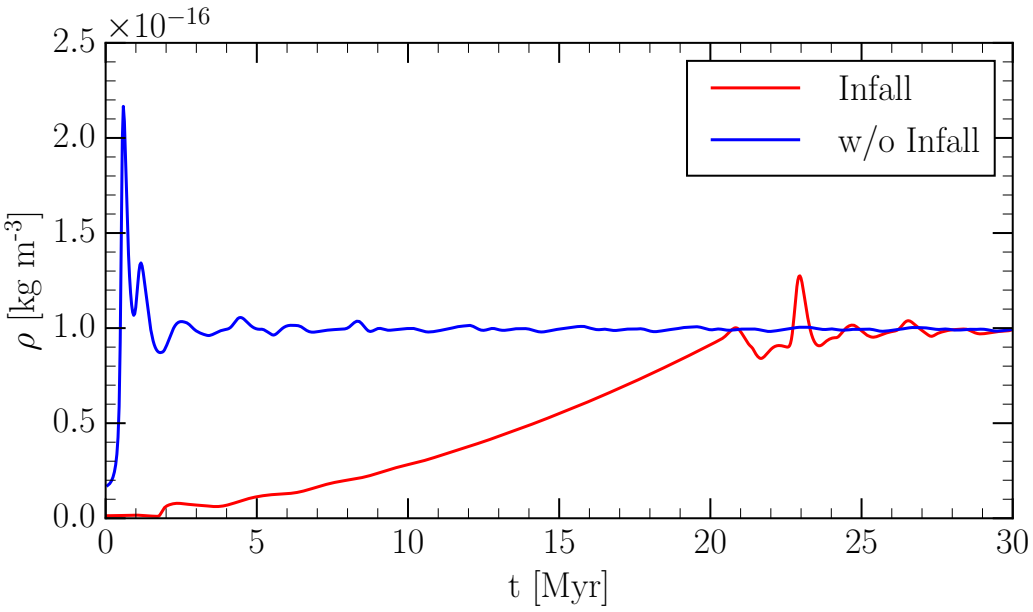

Figure 9: Central gas density evolution in simulations with (red line) and without infall (blue line) represented by model (1a) and (1b).

wards. The central density at this time exceeds a value of $2{\cdot}10^{-16}$ kg m^{-3} as shown in Fig.9. The hydrostatic equilibrium has been reached after ∼2 Myr in simulations without infall and after 21 Myr in infall simulations.

Model (2): Constant Density and Gas-to-Dust ratio
The evolution of a constant gas and dust distribution is presented in Fig.12. The infall in this model stops after 18.4 Myr. Major differences between the dust species are observed during the re-expansion phase (t $\geq$ 4.8 Myr) showing an evolution very similar to model (1) with infall, while the accretion phase displays nearly identical dust profiles and small drift velocities for each dust species. The maximum gas velocity $v_{g,max}$ = -581 m s^{-1} occurs at t = 10 Myr where small dust grains (blue line) exhibits nearly the same velocity profile leading to a very small drift velocity for this dust species. This simulation confirms the result of the previous model: a clear stratification of different dust species. Furthermore, it shows that the evolution of the re-expansion phase in infall simulations is nearly independent of the initial distribution.

Model (3): Supersonic Infall
Small and intermediate dust grains (0.1 and 1.0 μm) are well coupled with the gas as it is shown by blue and green lines in Fig.13. *A strong separation of small and large dust grains (10 μm)* is seen at nearly all time steps in spite of similar infall velocities for gas and individual dust species ($v_{infall,g,d}$ = 1000 m s^{-1}). The infall stops after ∼3.3 Myr. Fig.13 shows that the drift velocity v_g - v_d is strongly negative in case of large dust grains while species of small dust grains exhibit positive velocities as well. The drift velocity of the large dust species illustrated as red line is scaled down by a factor of 2. The drift velocity of small dust grains shows multiple peaks indicating that the velocity profile of the dust is broader than the gas velocity profile. It should be considered that the infall velocity is ∼5x the sound speed of

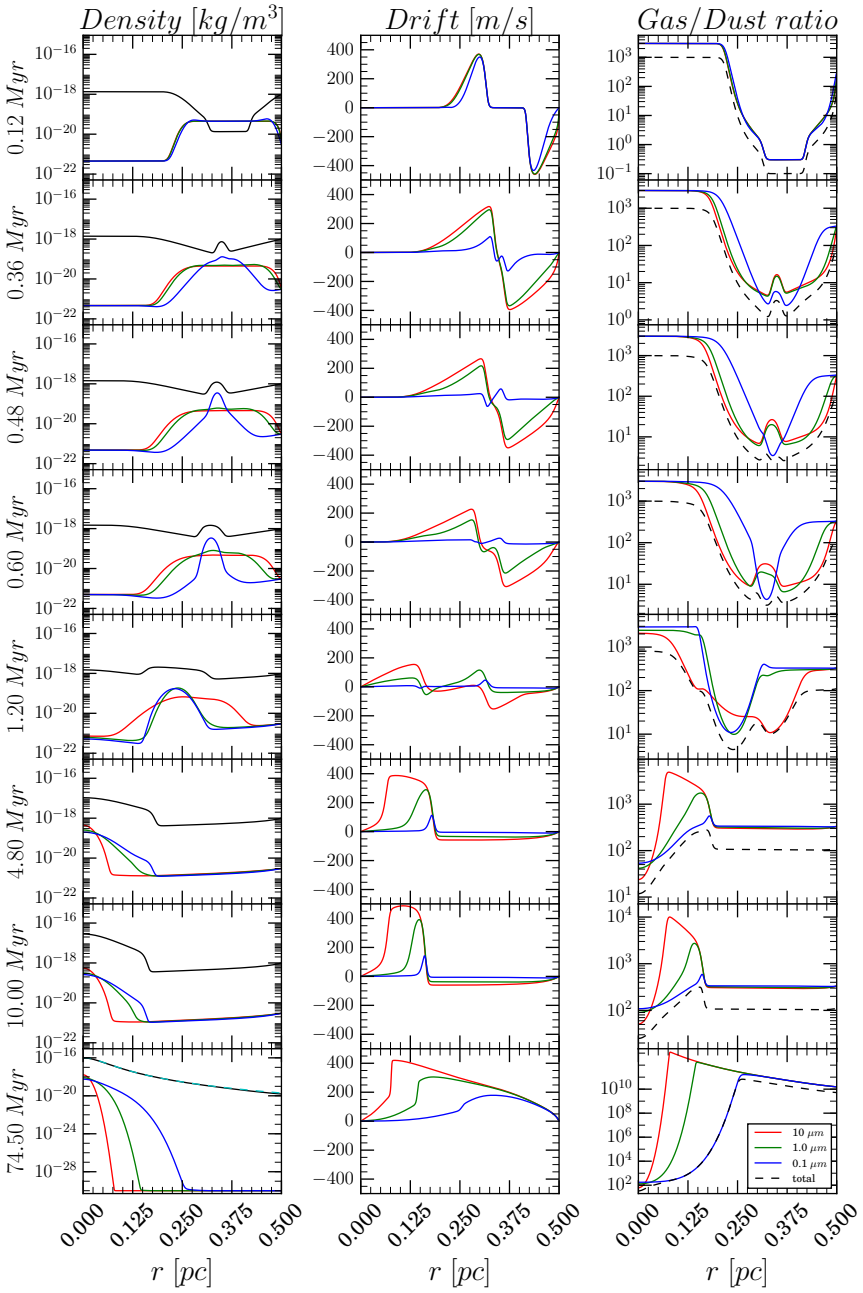

Figure 10: Evolution of an initial filament with uniform density and infall (Model 1a). The first panel describes the evolution of the radial density profile of gas, illustrated by black lines, and dust species illustrated by blue, green and red lines. Small dust grains with size s = 0.1 μm are indicated by blue lines, large dust particles with s = 10.0 μm by red lines, and green lines illustrate intermediate dust particles with s = 1.0 μm. The second panel shows the drift velocity v_g - v_{d_i} of individual dust species colored by the same color code as explained. The last panel reveals the evolution of the total (black dashed) and individual (colored) gas-to-dust ratios. Infall stops at t $\approx$ 20 Myr (time step not illustrated). The final gas profile at t = 75 Myr establish an Ostriker profile illustrated by the dashed cyan line.

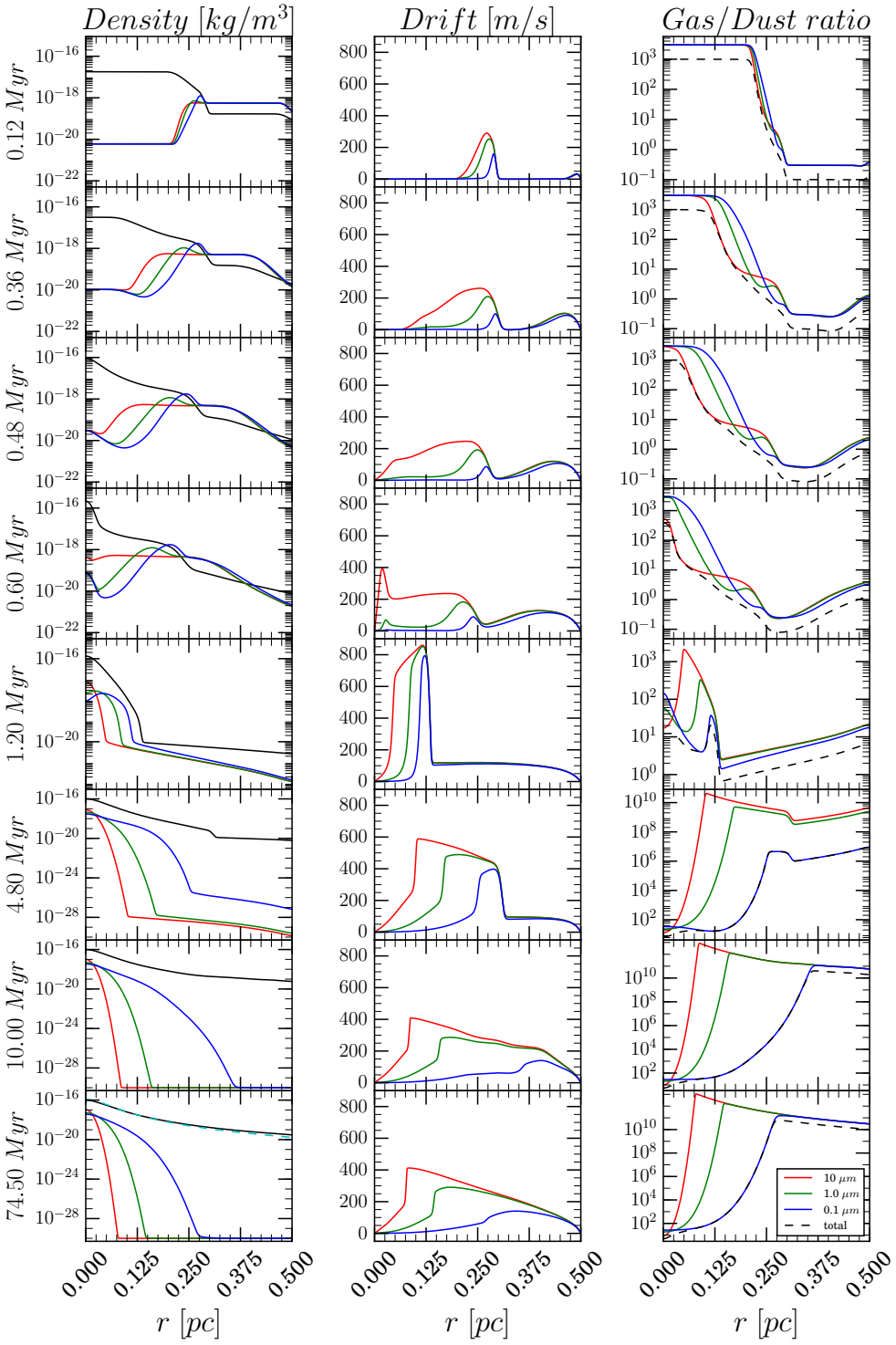

Figure 11: Same configurations as shown in Fig.10, but without infall and increased initial density (Model 1b). Major differences are seen in the drift velocity and gas-to dust ratio. Compared to the infall simulation, large dust species at e.g. t = 4.8 Myr and 75 Myr are radially more extended as it is also shown in the gas-to-dust ratio. Thus, large dust particles must primarily found within the filament itself. See Fig.10 for further description of the lines.

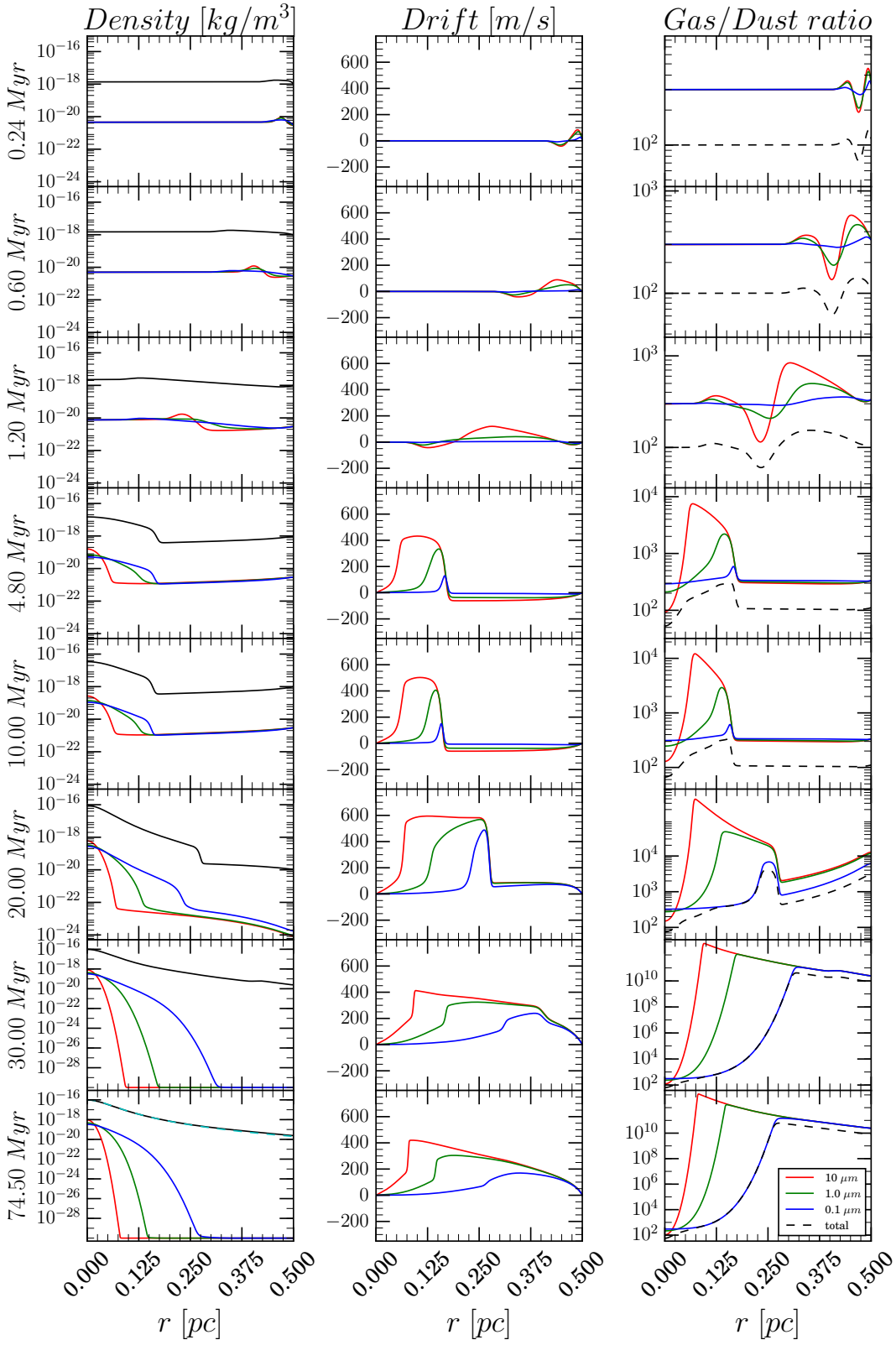

Figure 12: Evolution of the simulation presented by model (2), with an uniform density distribution and gas-to-dust ratio over the whole domain. See Fig.10 for further description of the lines.

molecular clouds with T = 10 K leading to shocks. This also leads to oscillations in the velocity evolution during the re-expansion phase. The maximum gas and dust velocity (towards the center) v_g = -1181 m s^{-1} and v_d = -1190 m s^{-1} occurs at t = 4.5 Myr but at different radii leading to a large drift velocities. This also shows that the evolution of the filament illustrated at that time step is still ongoing. In general, the gas and dust velocities at all time steps in this simulation have values between -1000 and -1200 m s^{-1} occurring almost always beyond the gas density peak, for instance, at ∼0.062 pc between t = 1.0 Myr and 2.0 Myr (not shown here). We, therefore, can see a distinct separation between small and large dust grains during the re-expansion phase *and* infall phase, depending on the initial conditions. The final profile at t = 4.5 Myr established an equilibrium profile up to r = 0.1 pc. This is, in other words, a nearly perfect Ostriker profile up to 0.1 pc surrounded by small density peak at 0.13 pc in a shell of constant density ($\rho_g \simeq 9{\cdot}10^{-19}$ kg m^{-3}). It should also be noted that the configuration at e.g. t = 1.4 Myr could be used for further simulations showing a central density peak surrounded by low density gas (a filament by definition as mentioned in section I).

Model (4): Initial Filament

The evolution of this model is illustrated in Fig.14. It also shows a clear coupling between gas and small dust particles during the infall and re-expansion phase, respectively. During the infall, very small dust grains (blue line) show a clear coupling resulting in a peak at t = 0.4 Myr. Nevertheless, the separation during the infall phase is weaker than in previous simulations. The dust density profiles are very similar until t = 0.8 Myr. A clear separation occurs during the re-expansion phase (t ≥ 1.2 Myr) where large dust grains remain at the center while small dust grains start to evolve with the gas outwards visible by the outwards evolving drift velocity profiles (in terms of the spatial width with v ≠ 0 m s^{-1}). The velocities during this phase are negative for both dust and gas. Large dust species show a broad drift velocity profile, e.g. at t = 2.0 Myr, indicating that the dust is still falling towards the center with high velocity while the gas is slowly (compared to the dust) moving inwards with a mean velocity $\bar{v}_g$ = -173 m s^{-1} resulting in a positive drift velocity. This slowly inwards moving gas in this phase settles down into an equilibrium configuration starting at the center and proceeding outwards. The smooth break at e.g. t = 3.0 Myr and r = 0.3 pc in the gas profile (and in the density profile of small dust grains due to the coupling) indicates the partition between gas in an equilibrium and non-equilibrium state and is the region of largest (negative) gas velocities. Small dust grains are strongly coupled with the gas and therefore show smaller drift velocities at the beginning of the re-expansion phase (t ≥ 0.8 Myr up to 2 Myr) until the break is reaching low gas densities where the coupling becomes weak and the outer peaks of the drift velocities at r = 0.3 pc show the same magnitude for all dust species. The infall in this simulation stops at roughly 0.4 Myr. The central gas density at t = 3.0 Myr is $\rho_g = 3.71{\cdot}10^{-16}$ kg m^{-3}. Maximum velocities $v_{max} \simeq$ -915 m s^{-1} of gas and dust occur at t = 0.8 Myr. There is also a large rebound effect resulting in an overdensity with $\rho_{g,max} = 7{\cdot}10^{-16}$ kg m^{-3} at t = 0.4 Myr persisting for at least 0.1 Myr. A summary of these four models is presented in table 3.

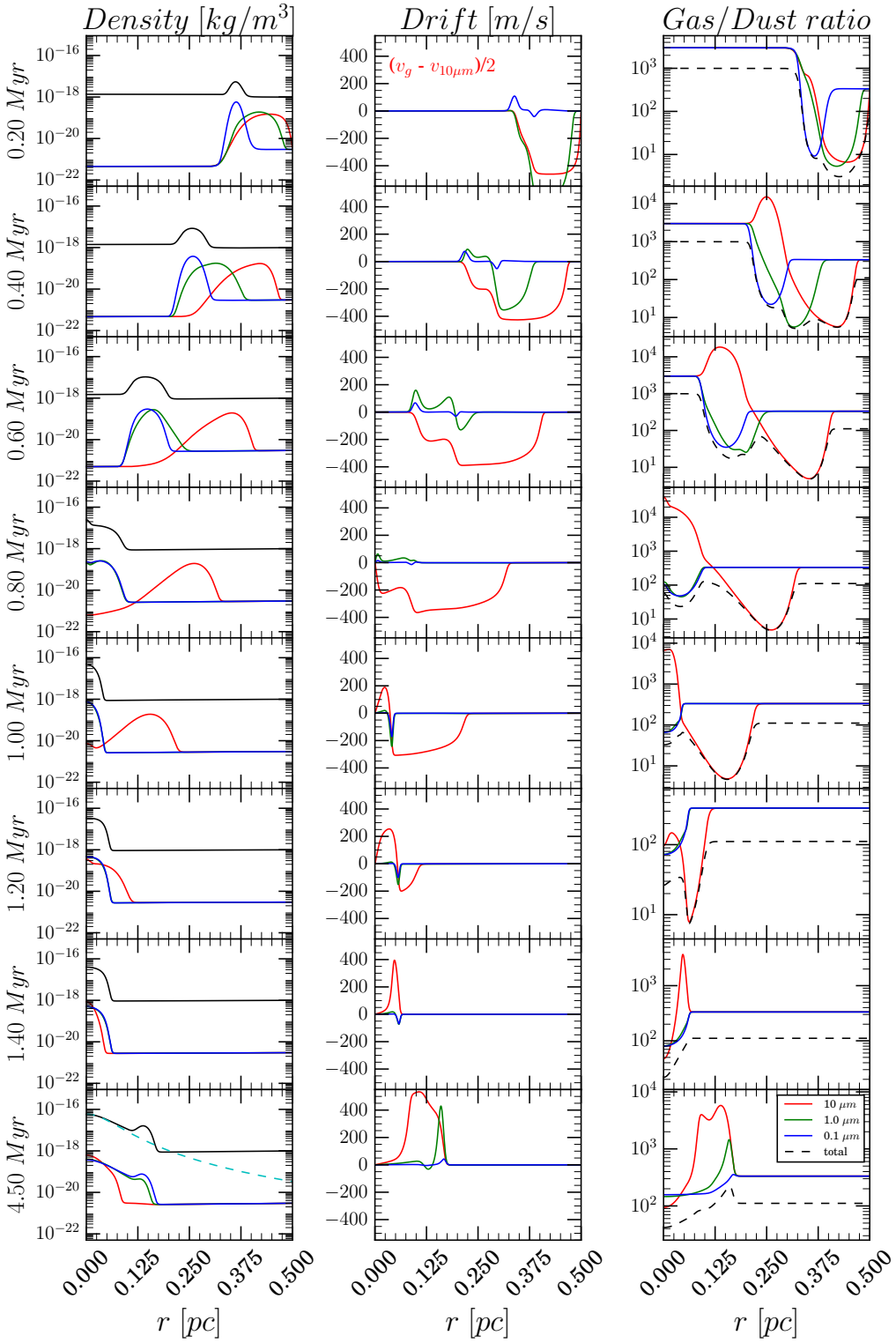

Figure 13: Evolution of the simulation with supersonic infall v_{infall} = -1000 m s^{-1} presented in (3). A clear separation between small and large dust species can be seen in both infall and re-expansion phase. The drift velocity of large dust grains (red line) is scaled down by a factor of 2. At t = 4.5 Myr, the density profiles established an equilibrium only in the inner ∼0.12 pc. See Fig.10 for further description of the lines.

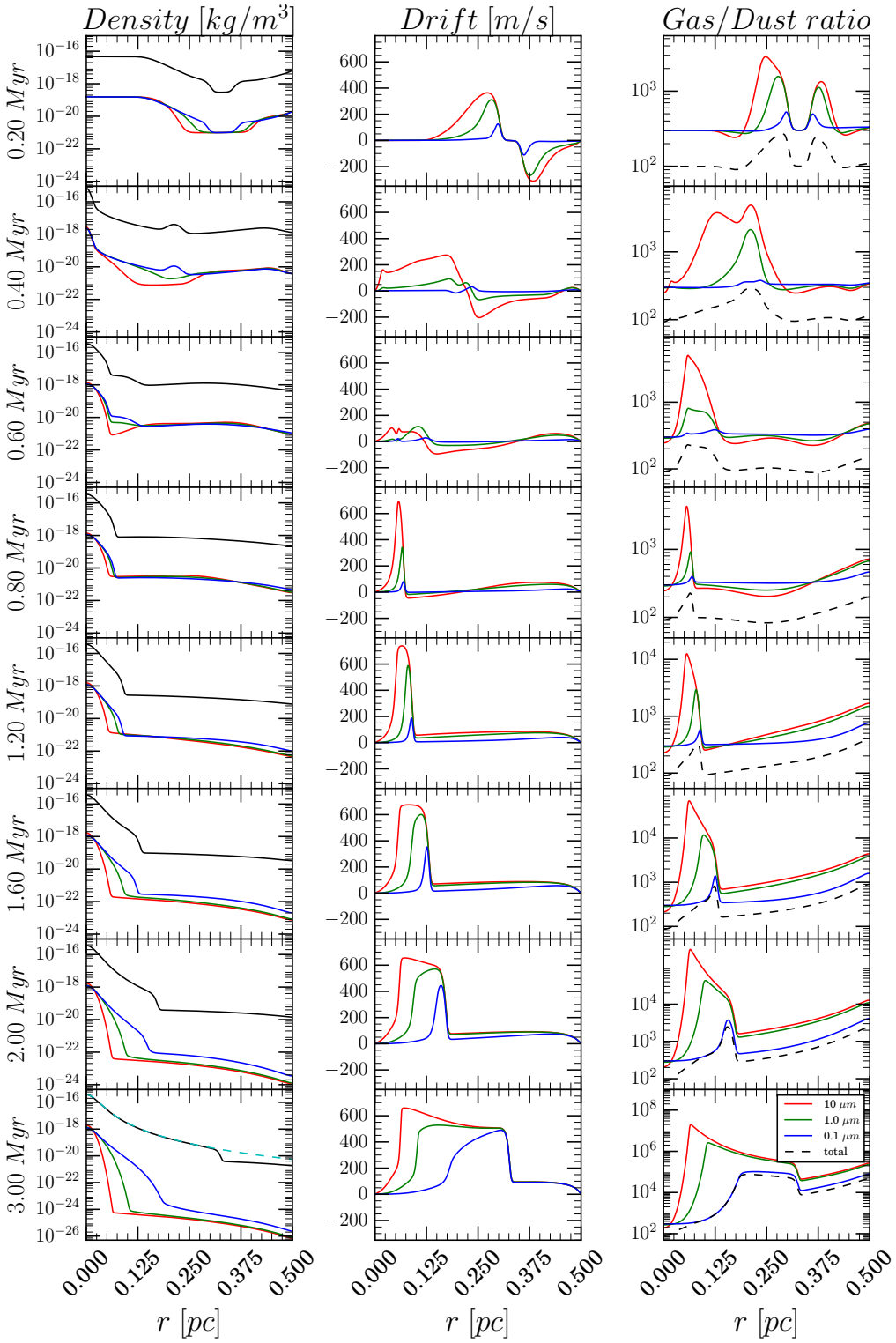

Figure 14: Result of the simulation with an initial filament and high infall rate (No.24 in Table 4) as described in model (4). Radial profiles of gas and dust are very similiar up to t = 0.8 Myr, especially that of small dust grains. A strong separation of the dust species occurs during the re-expansion phase at t $\geq$ 1.2 Myr. See Fig.10 for further description of the lines.

6.3.4. Result: Gas-to-Dust Ratios

Gas-to-dust ratios are shown in the last column of Fig.10 - Fig.14. The final ratios show similar shapes in all types of simulations, except in model (3) where only a part of the filament is in equilibrium. The linear decreasing ratio in the outer parts is an outcome of the minimum density threshold of $10^{-30}\ kg\ m^{-3}$. The distributions in the re-expansion phase show that the gas-to-dust ratio depends on the *radius and dust grain size*. For large dust species the ratio increases rapidly within the inner 0.1 pc indicating that large dust grains must primarily found in the filament itself while small dust grains are located beyond the filament as well, especially seen in Fig.10, Fig.11 and Fig.12. Small dust grains (blue lines) are strongly coupled to the gas resulting in a smaller gas-to-dust ratio. Large dust species evolve independently of the gas and, therefore, resulting in a larger drift velocity, on the one hand, and larger gas-to-dust ratio, on the other hand.

Both simulations in model (1) start with similar ratios (slightly larger than 10^3 in the inner part and smaller than 1 in the outer part) but end with different minimal values. The simulation without infall shows significantly smaller values than 10^2 in the inner 0.125 pc while the infall simulation reveals values up to $\sim 10^3$ (at r = 0.125 pc). While it shows values up to 10^4 during the infall phase, the re-expansion phase may reveal much higher values in model (1) and (2), depending on the lower dust density threshold in these simulations. Hence, the simulated gas-to-dust ratios strongly diverge from the widely used ratio of 10^2 in all time steps of the evolution. *The assumption of constant gas-to-dust ratios is, thus, not supported by these simulations.*

In both models (1) and (2) the final gas-to-dust ratios are very similar. There are no prominent differences between these simulations and simulations with and without infall. As it can be seen during the last time steps, the dust profiles still evolve towards the center due to the lack of pressure acting on the dust grains. The dust grains will completely settle onto the center. At this point, it should be mentioned that the dust grains in the interstellar medium do not take discrete values in terms of the dust size and density, but rather follow a continuous distribution (Weingartner and Draine, 2001). The dust species in model (3) and (4) presented in Fig.13 and Fig.14, respectively, may still evolve towards the center until the density threshold of 10^{-30} kg m^{-3} has been reached. This is, for instance in model (4), $\sim$5 orders of magnitude smaller in terms of the minimum dust density observed at t= 3.0 Myr where the gas-to-dust ratio is at $\sim 10^4$ - 10^7. I therefore expect a final gas-to-dust of about 10^{10} - 10^{13} in model (3) and (4) as well.

6.4. Synthetic Spectra

In the previous section, I have presented the evolution of four different models denoted as (1),(2),(3), and (4). Comparing them with each other reveals us the differences between individual models, for instance, comparing simulations with subsonic (model (1)) and supersonic infall (model (3)) demonstrates the differences between different infall velocities, or comparing a constant gas distribution with an initial filament (model (2) and (4)) shows the impact of different initial density distributions

on the evolution of the filament. Radio observations, however, may show us the evolution of filaments at a given moment obscuring the dynamical evolution of the filament. How can we diagnose the current dynamical state of observed filaments? How can we determine previous and upcoming evolution of these filaments? By developing synthetic spectra (see section 4 for a detailed description) for these models, I have made a statement about the dynamics and a prediction about observable signatures for filaments.

Observing $C^{18}O$ and N_2H^+ permit us the opportunity to trace regions in molecular clouds with different densities. Remind that $C^{18}O$ is tracing the diffuse gas with densities between $1.67 \cdot 10^{-18}$ and $1.67 \cdot 10^{-16}$ kg m^{-3} while N_2H^+ is tracing dense gas with $\rho \geq 3.35 \cdot 10^{-17}$ kg m^{-3}. In general, evolution with high infall velocities must be dominated by broad $C^{18}O$ or N_2H^+ lines, depending on the region where infall primarily happens. Filaments in an equilibrium state must provide narrow lines, that is, they show pure thermal lines without additional contribution of other velocity sources. Since the maximum gas density in the infall phase of my models is most of the time lower than the density where $C^{18}O$ or N_2H^+ arise, I do not expect prominent lines in this phase until their density threshold for the line excitation is exceeded.

According to the simplified treatment of interstellar depletion (see introduction), the $C^{18}O$ line must increase in intensity until after the time when N_2H^+ occurs. Then, $C^{18}O$ decreases and N_2H^+ becomes dominant in the central region. $C^{18}O$ must then be seen in a ringlike structure around the center. Broad lines should be seen in both species, depending on the gas density and velocity. During the re-expansion phase, broad lines should be seen along the line of sight within the inner overdensity due to the large negative infall velocities beyond this central region and the assumption of cylindrical symmetry, while the line intensity should be small (due to the projection effect) along the line of sight in regions where the infall actually happens. Beyond this region the density may be low and the lines should vanish, or at least be very small compared to the central emission lines. This is a preliminary assumption for these spectra.

Therefore, scanning a filament from the outside towards the center, individual lines should broaden and increase in intensity. We should therefore look at the center when the filament experience symmetric infall. Since the density profile of the filament is evolving outwards the velocities should be seen at a later point in time by off-centered spectra (for instance at 0.1 pc) as well, when the density is high enough for the formation and excitation of one of these species. Thus, we should also look for off-centered spectra ($x \neq 0$, see Fig.3), which may be helpful to determine the dynamical state of the filament.

6.4.1. Model (1): Infall vs. No Infall

The central synthetic spectra for simulations with and without infall are shown in Fig.15 and Fig.16. These figures show the synthetic spectra of $C^{18}O$ (blue lines) and N_2H^+ (red lines) for 12 different time steps during the evolution of the filament. The x-axes show the gas velocities between -2000 and 2000 m s^{-1} while the

y-axes illustrate the normalized intensities of the emission lines in arbitrary units. As expected, the emission lines in Fig.15 become dominant in the late evolution of the filament, primary at the re-expansion phase t $\geq$ 4.8 Myr, and the $C^{18}O$ line is observable before N_2H^+ occurs. Fig.16 illustrates the spectra of the faster evolving simulation without infall. Remember, this is due to the fact that the simulation without infall contains a higher initial mass and therefore attains a fast evolution towards the center. The evolution between t = 0.12 Myr and 1.20 Myr in this simulation should essentially also happen in the infall simulation between t = 10.00 Myr and 20.00 Myr. It shows an initial $C^{18}O$ line (due to the higher initial density) that broadens up to $\Delta v_{C^{18}O} \simeq 1108$ m s^{-1} at t = 0.48 Myr. This is the time where the N_2H^+ line occurs, with $\Delta v_{N_2H^+} \simeq 876$ m s^{-1}. The subsequent evolution increases the intensity of the N_2H^+ line and decreases the line width of both species. The N_2H^+ intensity remains constant for the rest of the evolution revealing that the central region, which is the main contributor for the N_2H^+ line, is already fully evolved in terms of density. Then, the intensity of $C^{18}O$ increases until t = 1.20 Myr, where the equilibrium is also developed in regions that contributes to the $C^{18}O$ emission. Further evolution, where the filament experience ongoing equilibrium formation in low density gas, reveals consistent spectra for all time steps. These consistent lines are also seen in the off-centered spectra at x = 0.1 pc in Fig.17, but only $C^{18}O$ with lower intensity. Therefore, the state of a filament during the infall phase can exactly be investigated while there are no remarkable differences in the re-expansion phase. The distinction between subsonic infall and no infall is complicated with these simulations. Observed velocities in these simulations tend to have similar order of magnitude during the re-expansion phase.

6.4.2. Model (2): Constant Density

The spectra for model (2) displayed in Fig.18 is quite similar to the spectra of the infall simulation in model (1). There are no broad lines and they become dominant only after t = 4.8 Myr (re-expansion phase). These strong similarities between different models lead to the conclusion that the evolution of the re-expansion phase is nearly independent of the initial gas distribution while the infall phase is strongly effected by it. Since we cannot observe any lines during the infall phase, we cannot deduce the initial distribution due to the spectra.

6.4.3. Model (3): Supersonic Infall

As expected, the supersonic infall in model (3) leads to a double peak in the $C^{18}O$ line (see Fig.19) growing in intensity between t = 0.2 Myr and 0.8 Myr followed by a fast transition from a double peaked spectra to a single narrow line within 0.2 Myr. This is the transition from the infall to the re-expansion phase (t $\geq$ 1.0 Myr). It is also the time where N_2H^+ occurs in the spectra for the first time. The N_2H^+ intensity shrinks at t = 1.2 Myr due to oscillations in the gas density during the growth of the filament. The evolution of the spectra at t $\geq$ 1.4 Myr shows a constant intensity increase in both species. Here, we see an unique double peaked spectra arguing for the supersonic infall, but only at low gas densities and during the infall phase. Thus, we can easily distinguish between subsonic and supersonic infall.

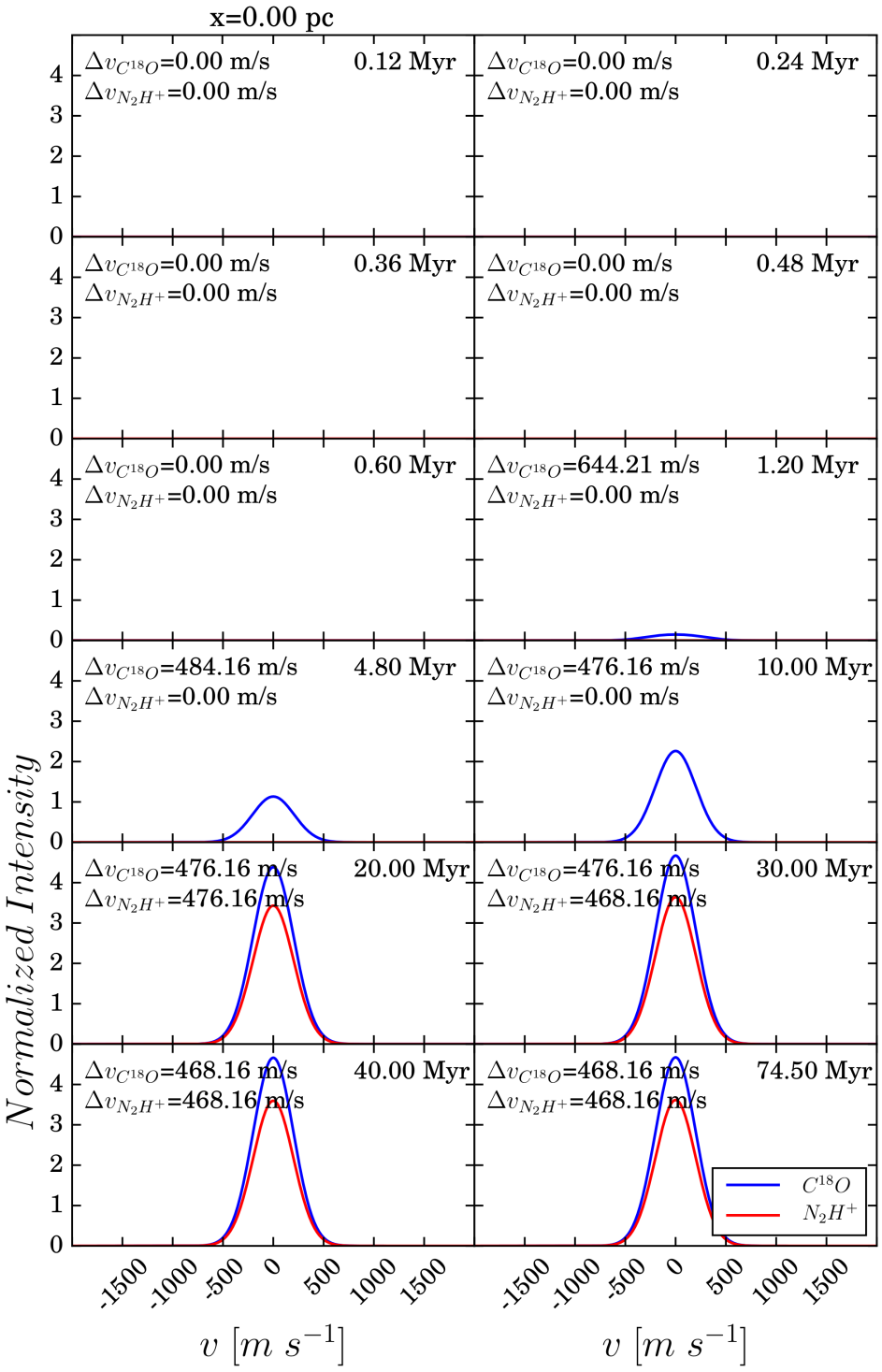

Figure 15: Central spectra of the infall simulation in model (1) at different time steps. It shows the intensity in arbitrary units (normalized to values in order unity) against velocity developed by the approach explained in section 4. The $C^{18}O$ line is indicated by the blue line, N_2H^+ by the red line. The lines become dominant during the re-expansion phase at t $\geq$ 4.8 Myr. The filament in equilibrium shows the same FWHM for $C^{18}O$ and N_2H^+.

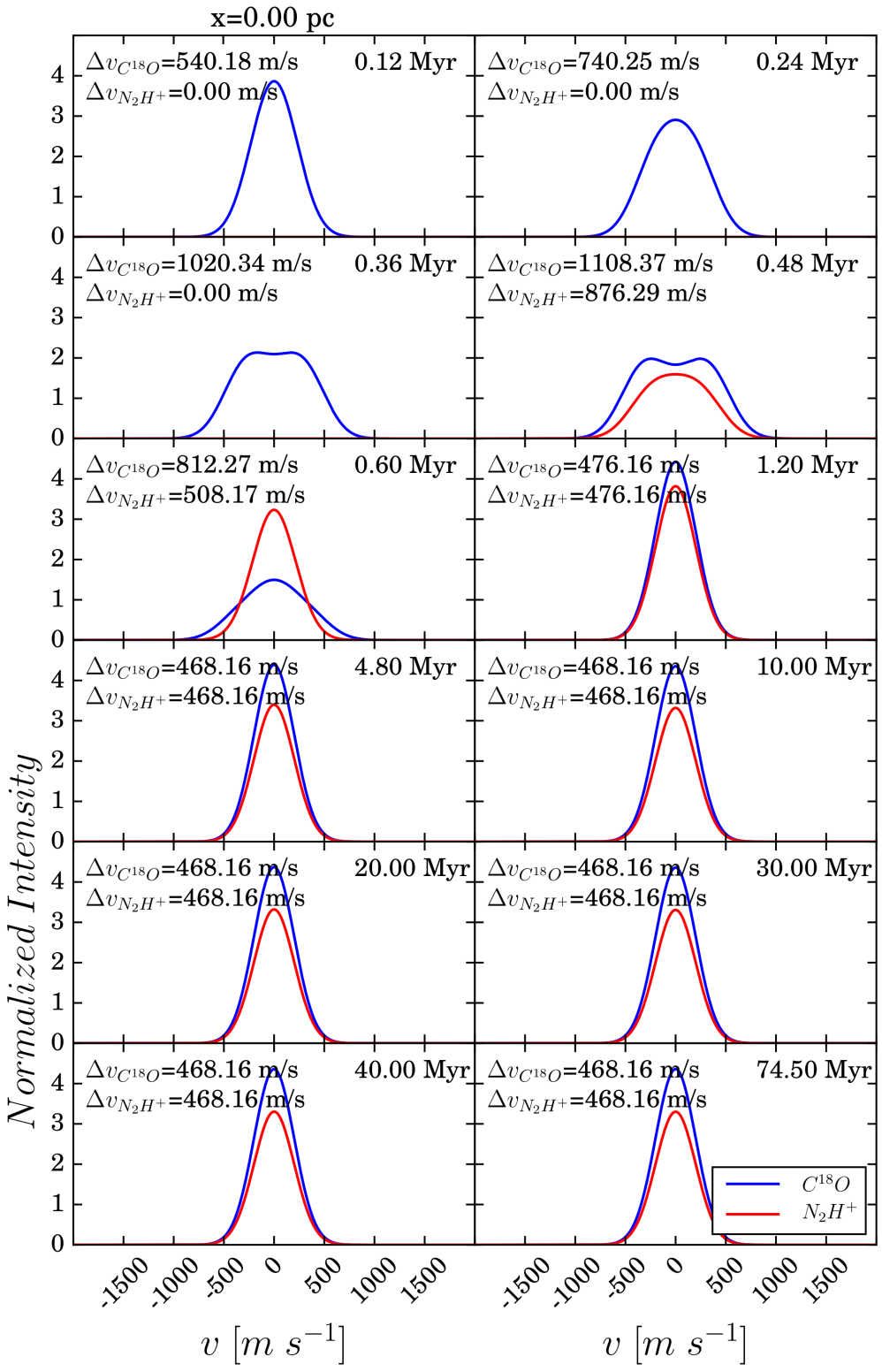

Figure 16: Central spectra of the simulation in model (1) without infall. An initial $C^{18}O$ is seen due to the larger initial density compared to the infall simulation in model (1). The infall phase is stamped by unique spectra between each time step. See Fig.15 for a further description.

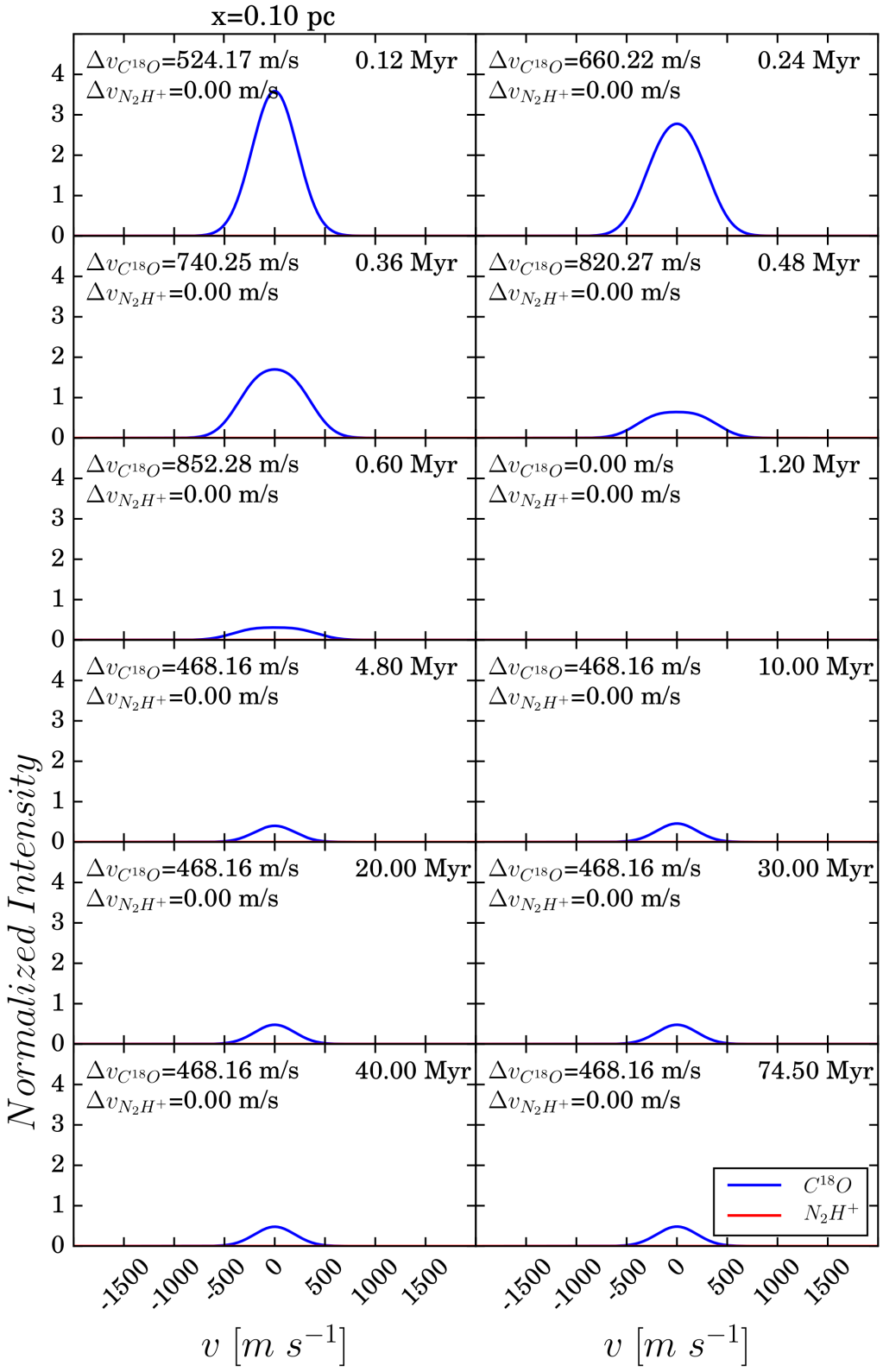

Figure 17: Off-centered spectra at r = 0.1 pc of simulation in model (1) without infall. There are no significant distinctions to differentiate between individual time steps. See Fig.15 for a further description.

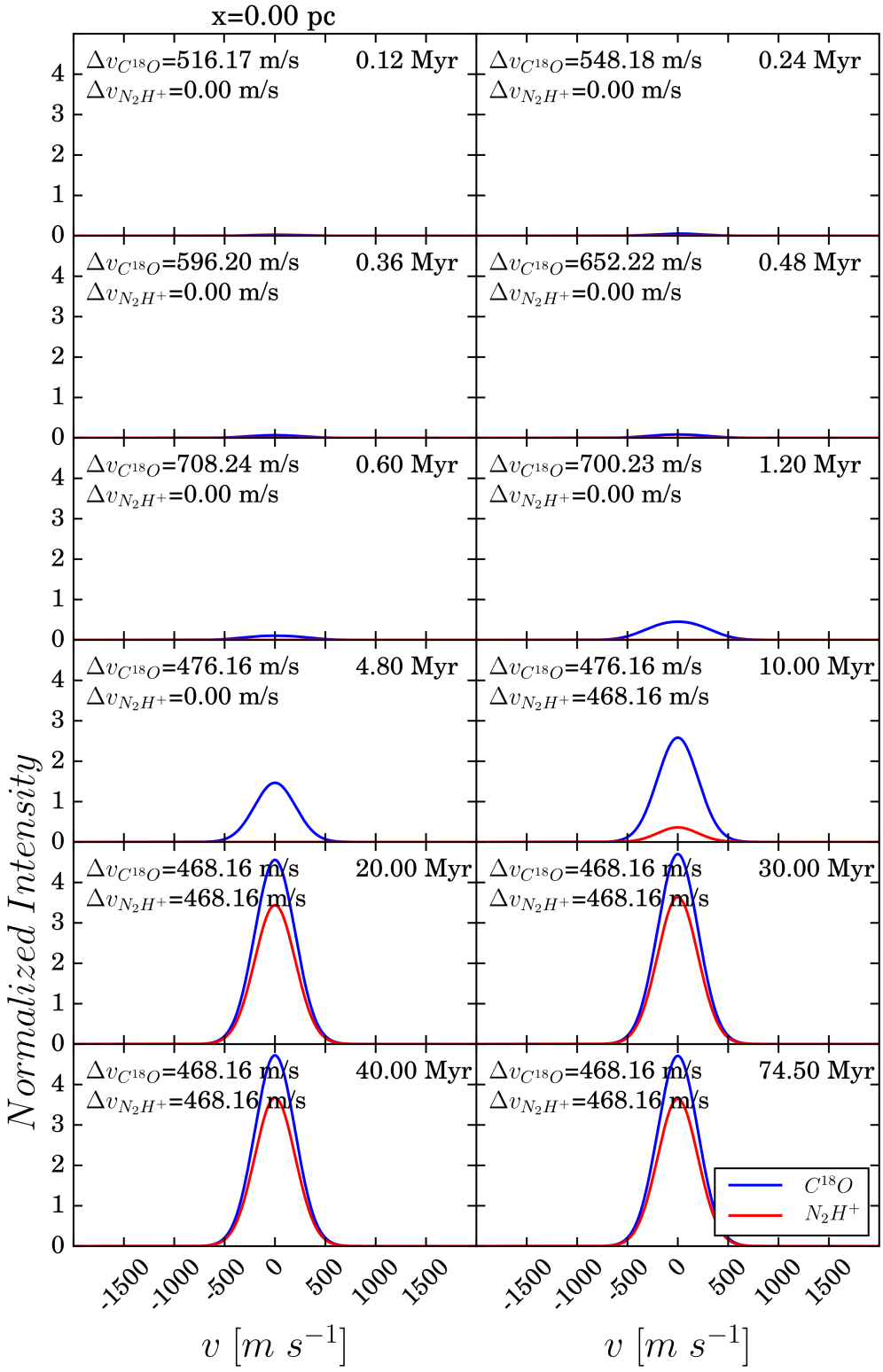

Figure 18: Evolution of the central synthetic spectra of simulation with constant density distribution and infall (model (2)). It is very similar to the central spectra of the infall simulation in model (1) leading to the conclusion that the re-expansion phase is not effected by the initial distribution. See Fig.15 for a further description.

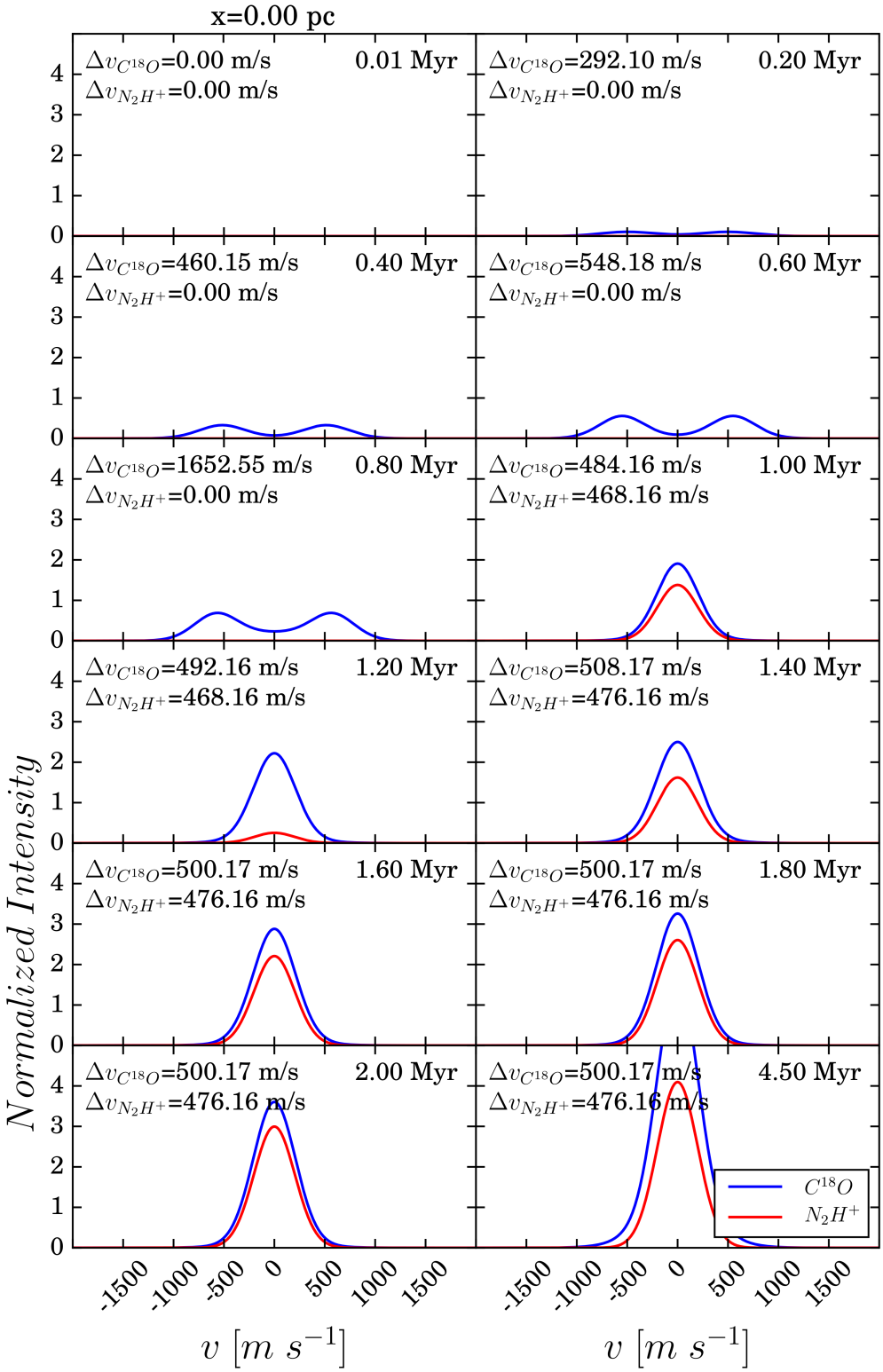

Figure 19: Central spectra for the simulation with supersonic infall. The evolution is dominated and unique by its double peaked lines in $C^{18}O$ during the infall phase. The transition to the re-expansion phase happens at t = 1.0 Myr. See Fig.15 for a further description.

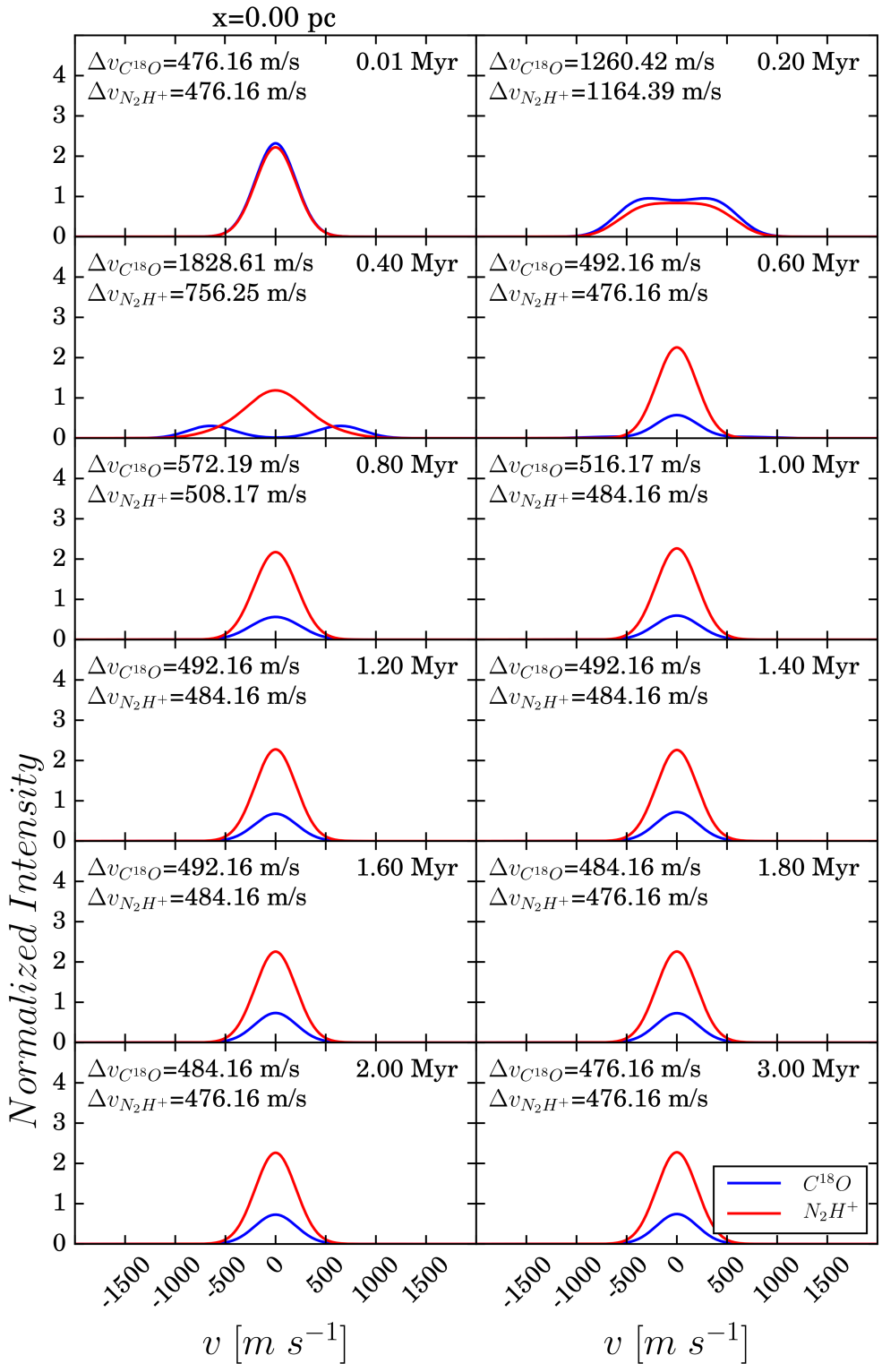

Figure 20: Central spectra of an initial filament with infall (model (4)). N_2H^+ and $C^{18}O$ lines are seen since the beginning of the simulation due to the large initial density. Again, the time steps during the infall phase are distinguishable between each other while the re-expansion phase shows very similar emission lines. See Fig.15 for a further description and Fig.21 for an off-centered spectra.

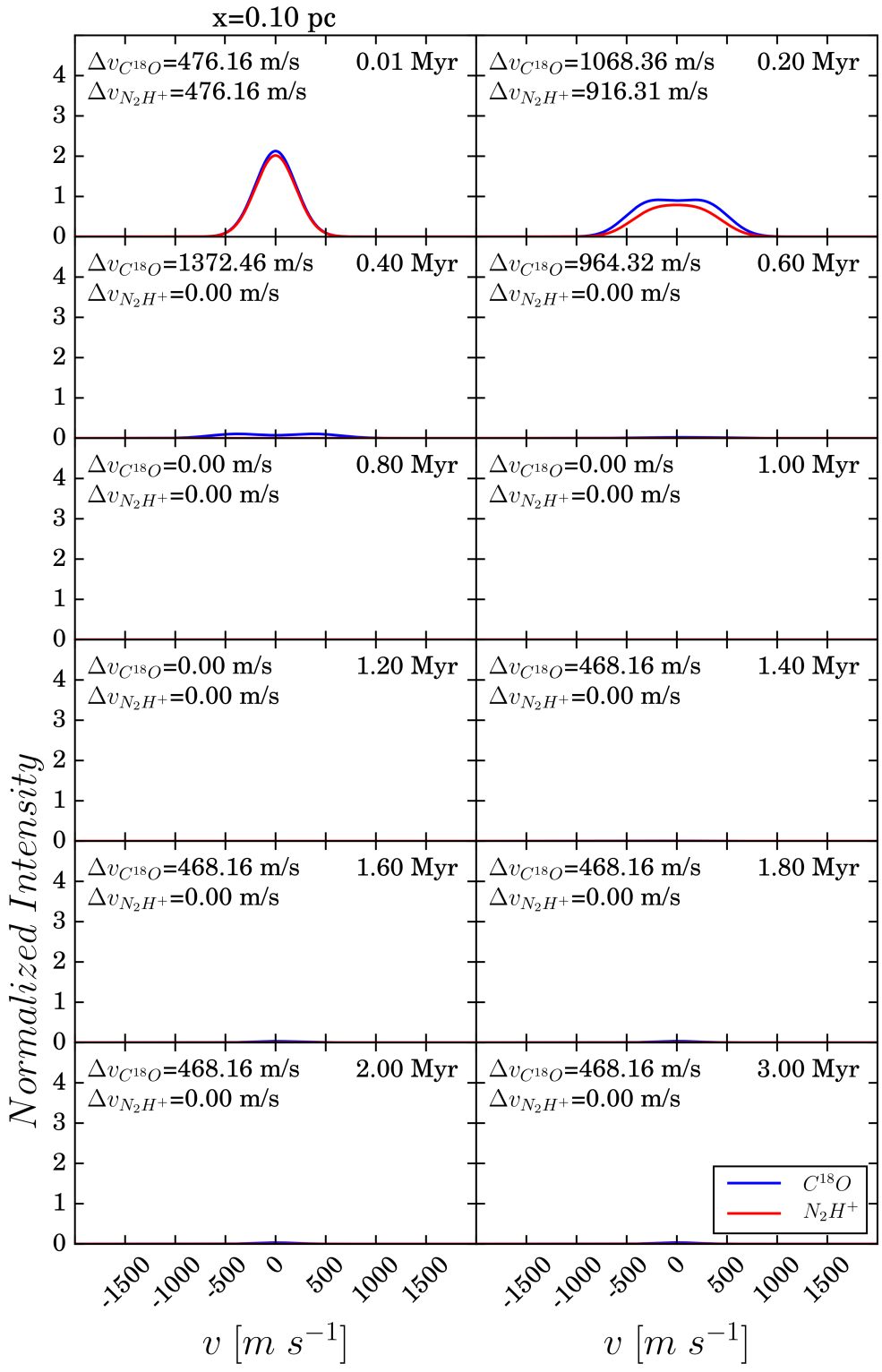

Figure 21: Off-centered spectra at r = 0.1 pc of an initial filament with infall represented by model (4) reveals differences only during the infall phase. The lines vanish during the re-expansion phase (t $\geq$ 0.6 Myr).

6.4.4. Model (4): Initial Filament

The synthetic spectra of the initial filament - model (4) - presented in section 6.3.3 is shown in Fig.20. It displays an equal intensity and FWHM in $C^{18}O$ and N_2H^+ at t = 0.01 Myr due to the constant initial gas density of $3.35{\cdot}10^{-17}$ kg m^{-3} where both $C^{18}O$ and N_2H^+ becomes excited. At this point, it should be considered that the intensities of two different species, in general, depends on the normalization and are not comparable with each other. The peak of both lines decreases and broadens (Δv up to $\sim$1260 m s^{-1}) at t = 0.2 Myr due to the infall towards the center. At t = 0.4 Myr, $C^{18}O$ construct a double peak around $\pm$ 700 m s^{-1} due to high infall velocities in the low-density region, while N_2H^+ shows a broad single line peaked at v = 0 m s^{-1}, means that the dense gas slows down and start to settle onto the center. In the following 0.2 Myr the N_2H^+ line increases in intensity and becomes narrow while the double peak in $C^{18}O$ disappears and develops a single weak line also at v = 0 m s^{-1}.

This is the beginning of the re-expansion phase where dense gas is already in rest. This picture remains nearly unchanged (the line width of both lines is slightly changing) until the end of the simulation. Thus, the gas releasing this emission is in an equilibrium state. Again, we can clearly distinguish the spectra of different time steps during the infall phase (due to the unique shape of the spectra at each time step) while both lines remains unchanged during the re-expansion phase. Observing an off-centered spectra x = 0.1 pc (see Fig.21) reveals no further in-depth information about both re-expansion and infall phase. It shows nearly the same lines for the first two time steps followed by a rapid decrease in intensity until both lines completely disappear at t = 0.6 Myr. In summary, the initial filament is collapsing within $\sim$0.6 Myr until the gas at r $\geq$ 0.1 pc has densities lower than the critical density for $C^{18}O$ and N_2H^+ excitation, and the observation of off-centered spectra at x $\geq$ 0.1 pc is prevented.

6.5. Infall

Herschel observations of the Taurus B211/3 filament have shown that filaments undergo infall of low-density gas through striations arranged perpendicular to them, with rates of $\sim$27-50 M$_\odot$ pc^{-1} Myr^{-1} and velocities $\sim$0.5-1 km s^{-1} (Palmeirim et al., 2013). This section is primarily concerned with infall to investigate the timescale to form a filament in hydrotatic equilibrium out of an uniform gas distribution and to link this timescale with typical molecular cloud lifetimes. For this purpose, I have considered infall from the outer ghost cell until a central density of $9{\cdot}10^{-17}$ kg m^{-3} is achieved (the central density ends up at $\sim10^{-16}$ kg m^{-3}, or $\sim3{\cdot}10^4$ cm^{-3}, a typical core density). Then, the outer boundary was changed to reflecting to permit the formation of hydrostatic equilibrium. An uniform distribution over the total spatial domain of 0.5 pc was assumed and rotation and dust were neglected.

The evolution of the central density for an uniform initial distribution with ρ = $1.34{\cdot}10^{-18}$ kg m^{-3} is shown in Fig.22, evolving until the infall stops at t = 9.12 Myr. Corresponding gas velocities at different radii are presented in Fig.23 showing velocities up to $\sim$700 m s^{-1} at r = 0.125 pc, a gas velocity roughly three times higher than

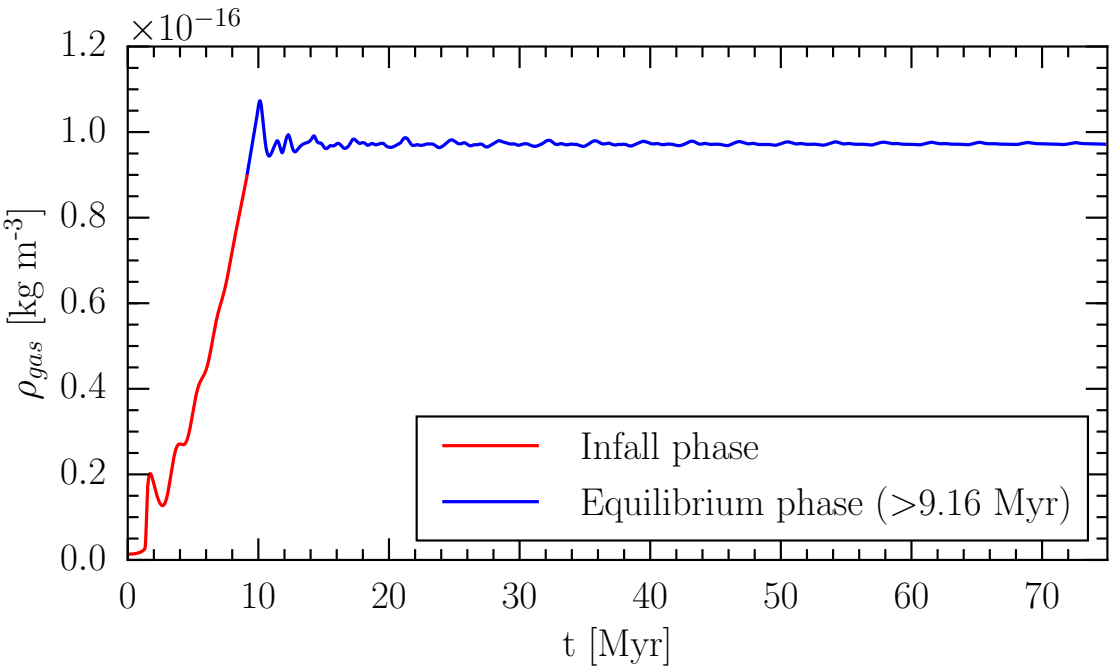

Figure 22: The evolution of the central gas density in a simulation with an uniform initial density $\rho = 1.34{\cdot}10^{-18}$ kg m^{-3}. The infall stops when the central gas density reaches a value of $\rho = 7 \cdot 10^{-17}$ kg m^{-3}. The red line indicates the accretion phase while the blue line shows the final phase after 9.16 Myr where the gas establish a radial profile in hydrostatic equilibrium. The central density remains unchanged after t $\approx$ 11 Myr under negligence of very small perturbations.

the sound speed of an isothermal filament with T = 10 K. A clear distinction between supersonic motion at the outer region (green and red line) and subsonic velocities in the inner part (red and black lines) can be seen. The gas velocities after the infall are nearly $\sim$0 m s^{-1} (well below the the threshold for numerical issues as mentioned in section 5). Further simulations were performed to determine infall and equilibrium timescales for different initial density, infall velocity, and infall density. The resulting timescales depending on different initial conditions are listed in table 4. An initial density of $1.34{\cdot}10^{-18}$ kg m^{-3} and $3.35{\cdot}10^{-18}$ kg m^{-3} corresponds to 400 cm^{-3} and 1000 cm^{-3}, respectively. A comparison with molecular cloud lifetimes (20-30 Myr) reveals that most of these filaments can be developed within the clouds lifetime by relatively low infall rates (compared to the observed infall rates mentioned above). Infall rates for simulation (6), (21), and (24) were derived in Fig.24. The total mass evolution is indicated by dashed lines in yellow, blue and green, respectively. Infall rates are illustrated by the solid lines. The black dashed line marks the critical line mass of 16.6 M$_\odot$ pc^{-1}. We can see that all these filaments are well below the critical line mass. Simulation (24) in Table 4 has the highest initial density, infall density, and initial infall velocity (with gas velocities up to -700 m s^{-1} during the evolution) and shows an infall rate of 12.4 M$_\odot$ pc^{-1} Myr^{-1}. This is consistent with the values observed by Palmeirim et al. (2013), more specifically, higher infall densities and velocities, and therefore higher infall rates, would be appropriate as well leading to a faster evolution.

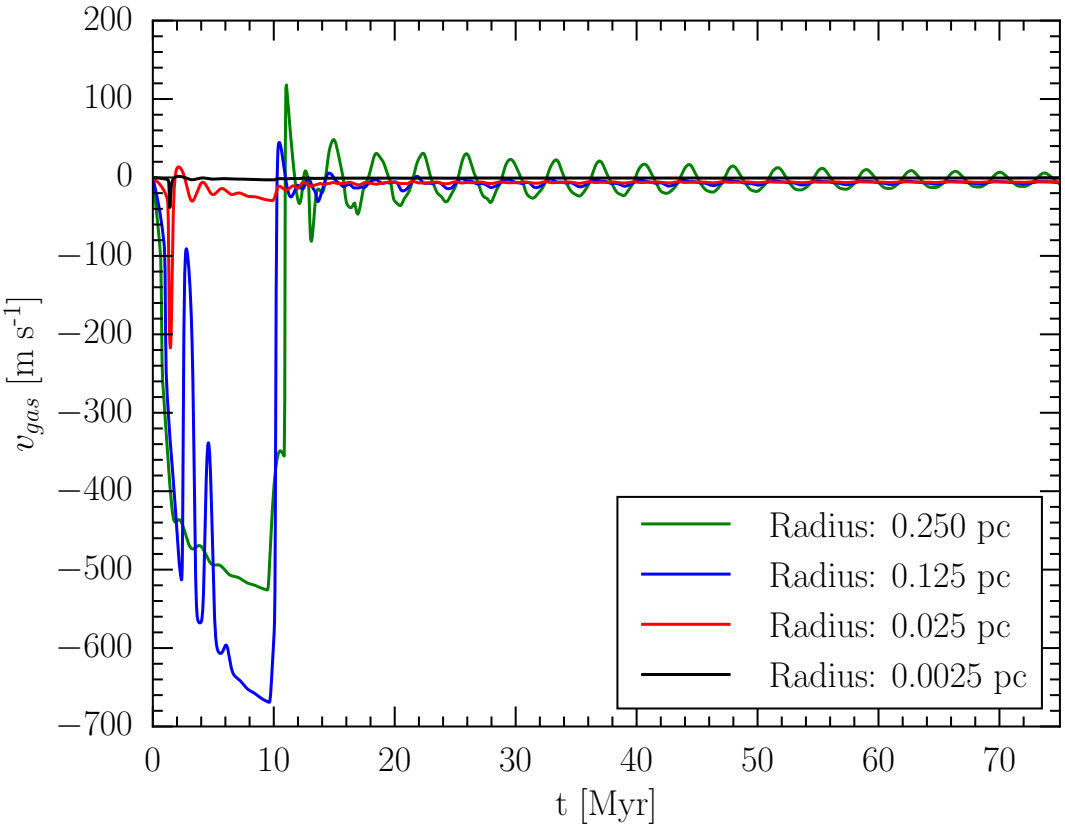

Figure 23: Evolution of the gas velocity at different radii in a simulation with infall v_{infall} = 0 m s^{-1} and ρ_{infall} = 5.34 · 10^{-18} kg m^{-1}. After the filament established an equilibrium state at t ≈ 11 Myr, only small velocities of v ≤ 50 m s^{-1} can be seen. These oscillations, primarily seen at large radii (e.g. green line), are numerical issues decreasing with time. During the infall, the outer region of the filament (blue and green line) exhibits velocities up to v_g ≈ -700 m s^{-1}.

In order to deduce whether the filament is in equilibrium or still experiencing infall, I have plotted the results from table 4 in a three-dimensional surface plot (see Fig.25). The blue surface indicates the infall time for simulations with ρ_{ini} = 1.34·10^{-18} kg m^{-3}, the red one simulations with ρ_{ini} = 3.35·10^{-18} kg m^{-3}. The green line marks a cloud lifetime of 20 Myr. If we locate a point below one of these surfaces, a corresponding filament undergoes infall while the region above these planes characterizes the period where either the hydrostatic equilibrium currently starts to form or filaments are already in an equilibrium state. The infall time strongly depends on the infall velocity and density. According to these results, filaments can be considered in equilibrium when 1) the cloud has an age of at least $t_{age} \geq$ 10 Myr and the simulated evolution of a filament starts at $t_{age} \simeq$ 0 Myr, and 2) the filament underwent infall with $\rho_{infall} \geqslant$ 3.35·10^{-18} kg m^{-3}. Older molecular clouds can, however, occupy filaments that have experienced a lower infall in the past.

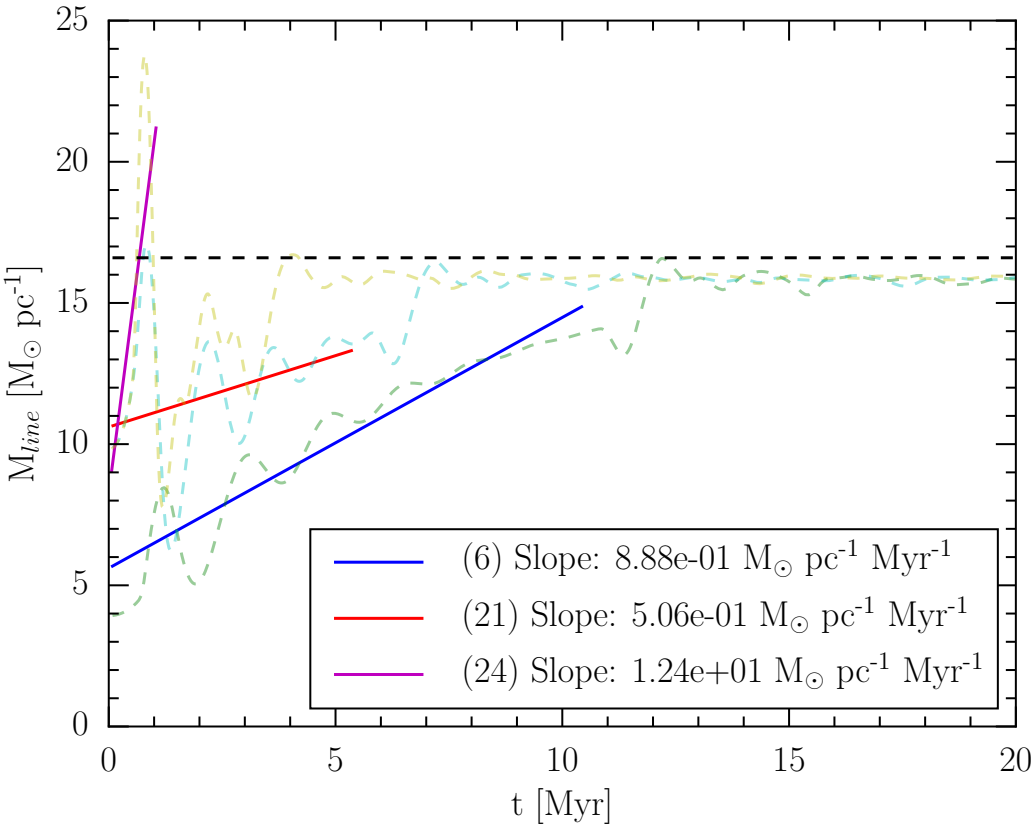

Figure 24: Linear mass evolution of three different setups (dashed lines) listed in table 4. The solid lines show the individual infall rates of these simulations. The black dashed line indicates the critical line mass of 16.6 $M_\odot$ pc^{-1}.

7. Final Remarks

I have investigated the evolution and dynamics of isothermal filaments in molecular clouds by simulating their radial profile and the development of synthetic spectra. I have considered gravity, rotation and a drag force between gas and three dust components. Furthermore, simulations were performed with a resolution of 2000 cells covering a spatial domain of 0.5 pc. I have investigated radial density profiles without dust and rotation in section 6.1 to compare their equilibrium state with the analytical Ostriker profile. Simulations in section 6.2 were performed to analyze rotating filaments and their differences to non-rotating filaments. Simulations considering gravity and the two-phase model by Miniati (2010) were presented in section 6.3 to investigate the evolution of gas and three dust species in four individual models differing in the infall from the outer ghost cell and the initial distribution of gas and dust. The timescales for infall with different initial conditions were explored in section 6.5. From these simulations, I have found the following results:

- Filaments in simulations without rotation and initial infall can establish a hydrostatic equilibrium by pure self-gravitation, which is very similar to the analytical solution found by Ostriker (1964). Regions with an initial density of $7{\cdot}10^{-18}$ kg m^{-3} (equivalent to $\sim 2.1{\cdot}10^{3}$ cm^{-3}) can develop a filament with

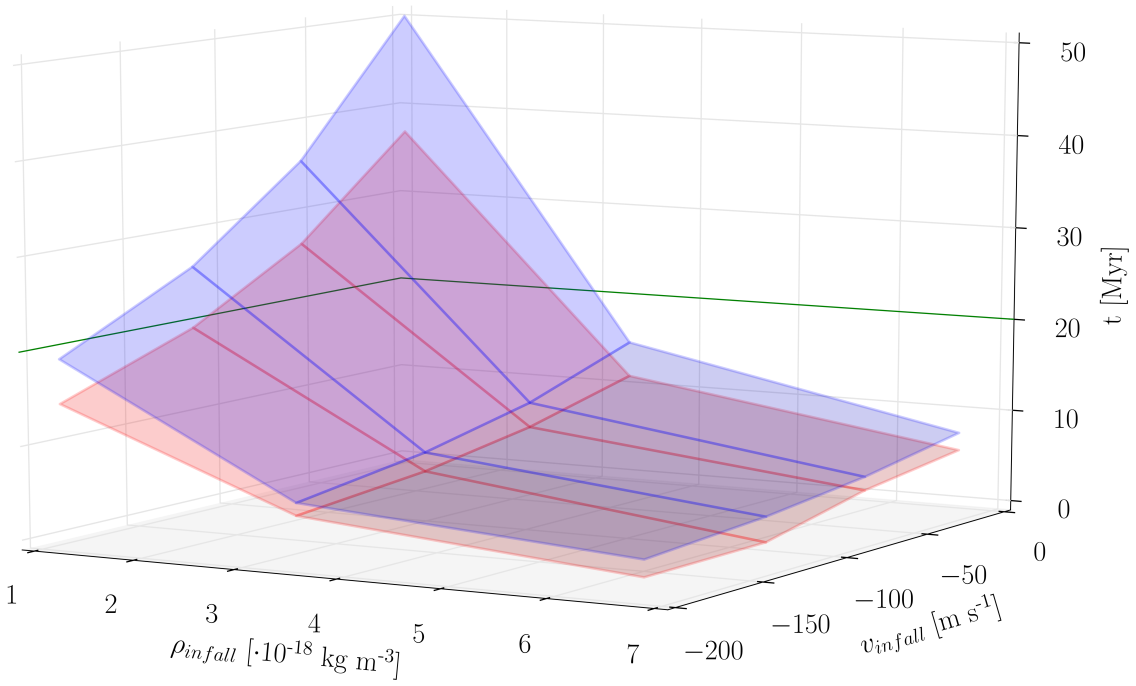

Figure 25: Three-dimensional surface plot of the results in table 4. The blue surface indicates the infall time of simulations with $\rho_{\mathrm{ini}} = 1.34{\cdot}10^{-18}$ kg m^{-3} while the red plane represents simulations with $\rho_{\mathrm{ini}} = 33.5{\cdot}10^{-18}$ kg m^{-3}. The green line marks the estimated lifetime t = 20 Myr for molecular clouds. Thus, most of the simulated filaments can form the hydrostatic equilibrium within the clouds lifetime.

mean width of 0.1 pc and should show N_2H^+ emission in the inner ∼0.05 pc (see Fig.5).

- Simulations with constant rotational frequency $\omega \leq 3.57{\cdot}10^{-14}$ s^{-1} have shown that the central density is not effected by the rotation. I did not find a solution with a reduced central density. Rotation primarily effects the outer region of the filament resulting in a higher density at large radii (see Fig.6). In simulations with $\omega \geq 3.58{\cdot}10^{-14}$ s^{-1} filaments can not be formed.

- A clear dust grain separation due to a pure dynamical effect is seen in all models and evolutionary phases of the filaments. The strength of this separation depends on the initial conditions, for instance, supersonic infall leads to a separation up to 0.25 pc (peak to peak) between small and large dust grains.

- The gas-to-dust ratio shows a dependency of the radius and dust grain size in all simulated filaments. The differences in the final gas-to-dust ratio between the individual models are irrelevant and strongly diverge from the well known ratio of 100.

No.	ρ_{ini} [kg m^{-3}]	ρ_{infall} [kg m^{-3}]	v_{infall} [m s^{-1}]	Infall period t [Myr]	Equilibrium[a] [Myr]
(1)	$1.34{\cdot}10^{-18}$	$1.00{\cdot}10^{-18}$	0.00	49.99	51.53
(2)	$1.34{\cdot}10^{-18}$	$1.00{\cdot}10^{-18}$	-60.00	35.53	37.01
(3)	$1.34{\cdot}10^{-18}$	$1.00{\cdot}10^{-18}$	-120.00	25.98	27.45
(4)	$1.34{\cdot}10^{-18}$	$1.00{\cdot}10^{-18}$	-190.00	18.78	20.21
(5)	$1.34{\cdot}10^{-18}$	$3.35{\cdot}10^{-18}$	0.00	14.68	17.27
(6)	$1.34{\cdot}10^{-18}$	$3.35{\cdot}10^{-18}$	-60.00	10.46	13.00
(7)	$1.34{\cdot}10^{-18}$	$3.35{\cdot}10^{-18}$	-120.00	7.70	10.90
(8)	$1.34{\cdot}10^{-18}$	$3.35{\cdot}10^{-18}$	-190.00	5.61	8.82
(9)	$1.34{\cdot}10^{-18}$	$6.67{\cdot}10^{-18}$	0.00	7.29	9.83
(10)	$1.34{\cdot}10^{-18}$	$6.67{\cdot}10^{-18}$	-60.00	5.24	8.40
(11)	$1.34{\cdot}10^{-18}$	$6.67{\cdot}10^{-18}$	-120.00	3.86	7.01
(12)	$1.34{\cdot}10^{-18}$	$6.67{\cdot}10^{-18}$	-190.00	2.90	6.01
(13)	$3.35{\cdot}10^{-18}$	$1.00{\cdot}10^{-18}$	0.00	36.94	38.49
(14)	$3.35{\cdot}10^{-18}$	$1.00{\cdot}10^{-18}$	-60.00	26.32	27.82
(15)	$3.35{\cdot}10^{-18}$	$1.00{\cdot}10^{-18}$	-120.00	19.33	20.79
(16)	$3.35{\cdot}10^{-18}$	$1.00{\cdot}10^{-18}$	-190.00	14.01	15.46
(17)	$3.35{\cdot}10^{-18}$	$3.35{\cdot}10^{-18}$	0.00	10.89	13.47
(18)	$3.35{\cdot}10^{-18}$	$3.35{\cdot}10^{-18}$	-60.00	7.77	10.30
(19)	$3.35{\cdot}10^{-18}$	$3.35{\cdot}10^{-18}$	-120.00	5.66	8.90
(20)	$3.35{\cdot}10^{-18}$	$3.35{\cdot}10^{-18}$	-190.00	4.25	7.46
(21)	$3.35{\cdot}10^{-18}$	$6.67{\cdot}10^{-18}$	0.00	5.38	7.92
(22)	$3.35{\cdot}10^{-18}$	$6.67{\cdot}10^{-18}$	-60.00	3.77	6.99
(23)	$3.35{\cdot}10^{-18}$	$6.67{\cdot}10^{-18}$	-120.00	1.15	6.31
(24)	$3.35{\cdot}10^{-18}$	$6.67{\cdot}10^{-18}$	-190.00	1.07	5.53

Table 4: Initial density, infall density, infall velocity, infall period and time after the equilibrium has been reached for 24 individual simulations without dust and rotation. Infall properties of simulation (4) were used for model (1) - (3) in section 6.3, simulation (24) for model (4). Simulations were performed with the Rusanov scheme.

[a]For a relative error of $\leq 10\%$ between actual density profile and analytical Ostriker profile within the innermost 1000 cells.

- According to these simulations, large dust grains must be preferentially located within the filament while small dust species may be beyond the filament as well, at least for the simulated time. The dust profiles still evolve towards the center at the end of the simulations (due to the positive drag velocity). Dust must completely end up at the center of the filament.

- Synthetic spectra were developed for each model presented in section 6.3 revealing that the spectra during the re-expansion phase is very similar in all time steps and all models, while the infall phase of these models is dominated by unique spectra due to the following reasons. $C^{18}O$ starts to broaden due to growing gas velocities towards the center. At some point (during the infall phase) the gas density exceeds the threshold for N_2H^+ excitation and shows a

narrow N_2H^+ line. Therefore, high-density gas preferentially exhibits quiescent behaviour in all simulations and time steps while low-density gas, traced by $C^{18}O$, is dominated by large velocities during the infall phase and also quiescent behaviour during the re-expansion phase. An off-centered spectrum does not reveal in-depth information about the evolutionary state of the filament.

- An analysis of infall simulations without dust and rotation shows that the timescale for infall and the formation of an equilibrium state is smaller than typical molecular cloud lifetimes for nearly all initial conditions. Assumed infall quantities in previous simulations are, therefore, adequate to form dense cores. A comparison with observed values from Palmeirim et al. (2013) shows that much higher infall rates are possible and would therefore lead to a faster evolution in time.

Part IV.
Discussion and Conclusion

In this thesis I have developed a hydrodynamical code and synthetic spectra to explore the dynamics and evolution of isothermal, self-gravitating filaments and to compare individual models with observed filaments. The evolution of simulated filaments is divided into two individual phases defined by the behaviour of the gas. The first phase, the infall phase, is dominated by gas falling onto the center of the filament. After the bulk of gas has settled in the center of the filament, the gas profile starts to evolve outwards. This is the beginning of the re-expansion phase dominated by the quiescent behaviour of the gas. These two phases are relevant for the evolution of filaments and the comparison of different models. I have explored the universal width of simulated filaments, the influence of rotation and the evolution of gas and dust. In order to make a statement about observable signatures for filaments, I have developed synthetic spectra for each model.

Simulations exploring the universal width of filaments in hydorstatic equilibrium were performed without infall, dust and rotation. These are very simplified assumptions, but it clearly shows that a filament with an Ostriker profile and a width of $\sim$0.1 pc can be established by pure self-gravity and enough mass. The results in Table 2 also reveals that we can not find an universal width for isothermal, self-gravitating filaments. The width of filaments in these simulations strongly depends on the total mass within the simulated frame. We therefore need further physical processes to explain the universal width of filaments.

Simulations with rotation did not show a flattening of the radial density profile resulting in a broadening of the profile. I found two groups of simulations, one for $\omega \geq 3.58{\cdot}10^{-14}$ s^{-1} where the radial gas profiles show their peak at the outermost region of the simulated domain, and one for $\omega \leq 3.57{\cdot}10^{-14}$ s^{-1} where the central density is retained and only the outer region of the gas profiles reveals a change, an increase in density. That can be explained by the linear dependency of the radius while ω^2 is constant at all radii. The gas will be pushed outwards when the centrifugal force is too high. Furthermore, the gas velocity in equilibrium reveals values about $\pm$600 m s^{-1}, which is not consistent with the definition of the hydrostatic equilibrium.

Interesting results are obtained with the implementation of the two-phase model, for instance, a separation of dust species due to a pure dynamical effect primarily during the re-expansion phase, or the gas-to-dust ratio depending on dust size and radius of the filament. Here, we should keep in mind that we deal with discrete dust grain sizes while the true size distribution is a continuous function (see, e.g. Weingartner and Draine (2001)). The true gas-to-dust ratio should not show this strong dependency on the radius. The variation must be smaller since we have to deal with smaller dust grains as well, while dust grains larger than 1.0 μm are uncommon. However, the finding that large dust grains should primarily be observed within the filament should be unaffected. We should also keep in mind that additional processes, such as grain growth by collision, or in general, any interaction between dust

grains, were neglected.

The development of synthetic spectra reveals another interesting result. According to these spectra, it should be possible to determine the exact age of a filament during the infall phase (due to unique spectra), while we could not distinguish between individual time steps in the re-expansion phase. Comparing the models with each other, it should be possible to determine the initial conditions for observed filaments. For comparison with observed spectra the broadening of emission lines due to turbulence and the intensity of synthetic spectra in arbitrary units should be considered.

The investigation of pure infall simulations, without dust and rotation, has revealed that we can simply develop a filament within the clouds lifetime by relatively low infall rates and most of the filaments (under several assumption) should therefore be in hydrostatic equilibrium. The differences to observed filaments is the lifetime. Observed filaments have a limited lifetime depending on their mean volume density (Jessop and Ward-Thompson, 2000), while simulated filaments in this thesis stay in the hydrostatic equilibrium, in principle, forever. We can, however, apply this result to adjust timescales and infall rates of the simulated models.

Numerous simulations with turbulence and magnetic fields were performed and have shown that these physical processes are crucial for the formation and evolution of molecular clouds and filaments (see introduction). Poloidal and toroidal magnetic fields effect filaments in different ways. A poloidal field supports the pressure against the gravity, while a toroidal field assists the gravity by squeezing down on the surface of the filament (Fiege and Pudritz, 2000). An example for the role of turbulence is the association of the filaments width with the sonic scale of turbulence or the cutoff wavelength for MHD waves, which are also expected to be $\sim$0.1 pc (for instance, Hennebelle (2013) or discussion in Arzoumanian et al. (2011)), or velocity-coherent fibers which could be an indication of accretion-driven turbulence. We definitely have to consider various physical processes to find one explaining the universal width of filaments, or other observed phenomena, but this is not the main goal of the thesis. The goal is to find a way to make a statement about the evolution of filaments since our observations reveal us a picture only for a single point in time. The dynamics of filaments in molecular clouds is complex, and so are simulations to find a detailed result for this problem.

Acknowledgments

I thank my supervisors Alvaro Hacar and Simone Recchi for the great support and detailed recommendations, and for their patience in the past 1.5 years. I also thank them for suffering my bad English skills, which was sometimes an obstacle. A special thanks to Simone who was not obliged to support me.

Bibliography

P. André, A. Men'shchikov, S. Bontemps, V. Könyves, F. Motte, and et al. From filamentary clouds to prestellar cores to the stellar IMF: Initial highlights from the Herschel Gould Belt Survey. *A&A*, 518:L102, July 2010.

P. André, J. Di Francesco, D. Ward-Thompson, S.-I. Inutsuka, R. E. Pudritz, and J. E. Pineda. From Filamentary Networks to Dense Cores in Molecular Clouds: Toward a New Paradigm for Star Formation. *Protostars and Planets VI*, pages 27–51, 2014.

D. Arzoumanian, P. André, P. Didelon, V. Könyves, N. Schneider, A. Men'shchikov, T. Sousbie, A. Zavagno, S. Bontemps, J. di Francesco, M. Griffin, M. Hennemann, T. Hill, J. Kirk, P. Martin, V. Minier, S. Molinari, F. Motte, N. Peretto, S. Pezzuto, L. Spinoglio, D. Ward-Thompson, G. White, and C. D. Wilson. Characterizing interstellar filaments with Herschel in IC 5146. *A&A*, Vol. 529:L6, May 2011.

J. Bally, W. D. Langer, A. A. Stark, and R. W. Wilson. Filamentary structure in the Orion molecular cloud. *ApJ*, 312:L45–L49, Jan. 1987.

E. E. Barnard. On a nebulous groundwork in the constellation Taurus. *ApJ*, 25: 218, Apr 1907.

E. E. Barnard. On the dark markings of the sky, with a catalogue of 182 such objects. *ApJ*, 49:1–24, Jan 1919.

P. J. Benson and P. C. Myers. A survey for dense cores in dark clouds. *ApJS*, 71: 89–108, Sept. 1989.

E. A. Bergin and M. Tafalla. Cold Dark Clouds: The Initial Conditions for Star Formation. *ARA&A*, 45:339–396, Sept. 2007.

P. H. Bodenheimer. *Principles of Star Formation*. Astronomy and Astrophysics Library. Springer, 2011.

S. F. Davis. Simplified second-order godunov-type methods. *SIAM J. Sci. Stat. Comput.*, 9(3):445–473, May 1988. ISSN 0196-5204.

M. Dopita and R. Sutherland. *Astrophysics of the Diffuse Universe*. Astronomy and Astrophysics Library. Springer Berlin Heidelberg, 2013. ISBN 9783662058664.

B. Draine. *Physics of the Interstellar and Intergalactic Medium*. Princeton Series in Astrophysics. Princeton University Press, 2010. ISBN 9781400839087.

B. G. Elmegreen and J. Scalo. Interstellar Turbulence I: Observations and Processes. *ARA&A*, 42:211–273, Sept. 2004.

K. M. Ferrière. The interstellar environment of our galaxy. *Reviews of Modern Physics*, Vol. 73:1031–1066, Oct 2001.

J. D. Fiege and R. E. Pudritz. Helical fields and filamentary molecular clouds - I. *MNRAS*, 311:85–104, Jan. 2000.

R. J. Gould and E. E. Salpeter. The Interstellar Abundance of the Hydrogen Molecule. I. Basic Processes. *ApJ*, 138:393, Aug. 1963.

A. Hacar and M. Tafalla. Dense core formation by fragmentation of velocity-coherent filaments in L1517. *A&A*, 533:A34, Sept. 2011.

A. Hacar, M. Tafalla, J. Kauffmann, and A. Kovács. Cores, filaments, and bundles: hierarchical core formation in the L1495/B213 Taurus region. *A&A*, 554:A55, June 2013.

C. J. Hansen, M. L. Aizenman, and R. L. Ross. The Equilibrium and Stability of Uniformly Rotating, Isothermal Gas Cylinders. *ApJ*, 207:736–744, Aug. 1976.

P. Hennebelle. On the origin of non-self-gravitating filaments in the ISM. *A&A*, 556:A153, Aug. 2013.

S.-i. Inutsuka and S. M. Miyama. A Production Mechanism for Clusters of Dense Cores. *ApJ*, 480:681–693, May 1997.

N. E. Jessop and D. Ward-Thompson. A far-infrared survey of molecular cloud cores. *MNRAS*, 311:63–74, Jan. 2000.

D. Johnstone and J. Bally. JCMT/SCUBA Submillimeter Wavelength Imaging of the Integral-shaped Filament in Orion. *ApJ*, 510:L49–L53, Jan. 1999.

J. Kauffmann, F. Bertoldi, T. L. Bourke, N. J. Evans, II, and C. W. Lee. MAMBO mapping of Spitzer c2d small clouds and cores. *A&A*, 487:993–1017, Sept. 2008.

M. R. Krumholz, C. D. Matzner, and C. F. McKee. The Global Evolution of Giant Molecular Clouds. I. Model Formulation and Quasi-Equilibrium Behavior. *ApJ*, 653:361–382, Dec. 2006.

P. D. Lax. Weak solutions of nonlinear hyperbolic equations and their numerical computation. *Comm. Pure. Appl. Math.*, pages 159–193, 1954.

R. LeVeque, O. Steiner, A. Gautschy, D. Mihalas, E. Dorfi, and E. Müller. *Computational Methods for Astrophysical Fluid Flow: Saas-Fee Advanced Course 27. Lecture Notes 1997 Swiss Society for Astrophysics and Astronomy*. Saas-Fee Advanced Course. Springer Berlin Heidelberg, 1998. ISBN 9783540644484.

R. J. LeVeque. *Finite volume methods for hyperbolic problems*. Cambridge texts in applied mathematics. Cambridge University Press, Cambridge, New York, 2002. ISBN 0-521-81087-6.

X. Li, A. N. Heays, R. Visser, W. Ubachs, B. R. Lewis, S. T. Gibson, and E. F. van Dishoeck. Photodissociation of interstellar N_2. *A&A*, 555:A14, July 2013.

C. D. Matzner. On the Role of Massive Stars in the Support and Destruction of Giant Molecular Clouds. *ApJ*, 566:302–314, Feb. 2002.

F. Miniati. A hybrid scheme for gas-dust systems stiffly coupled via viscous drag. *Journal of Computational Physics*, May 2010.

S. Molinari, B. Swinyard, J. Bally, M. Barlow, J.-P. Bernard, P. Martin, T. Moore, A. Noriega-Crespo, R. Plume, L. Testi, A. Zavagno, A. Abergel, B. Ali, and et al. Clouds, filaments, and protostars: The Herschel Hi-GAL Milky Way. *A&A*, 518: L100, July 2010.

T. Nagai, S.-i. Inutsuka, and S. M. Miyama. An Origin of Filamentary Structure in Molecular Clouds. *AjP*, 506:306–322, Oct. 1998.

J. Ostriker. The Equilibrium of Polytropic and Isothermal Cylinders. *ApJ*, Vol. 140: 1056, Oct 1964.

P. Padoan, M. Juvela, A. A. Goodman, and Å. Nordlund. The Turbulent Shock Origin of Proto-Stellar Cores. *ApJ*, 553:227–234, May 2001.

P. Palmeirim, P. André, J. Kirk, D. Ward-Thompson, D. Arzoumanian, V. Könyves, P. Didelon, N. Schneider, M. Benedettini, S. Bontemps, J. Di Francesco, D. Elia, M. Griffin, M. Hennemann, T. Hill, P. G. Martin, A. Men'shchikov, S. Molinari, F. Motte, Q. Nguyen Luong, D. Nutter, N. Peretto, S. Pezzuto, A. Roy, K. L. J. Rygl, L. Spinoglio, and G. L. White. Herschel view of the Taurus B211/3 filament and striations: evidence of filamentary growth? *A&A*, 550:A38, Feb. 2013.

T. Passot, E. Vazquez-Semadeni, and A. Pouquet. A Turbulent Model for the Interstellar Medium. II. Magnetic Fields and Rotation. *ApJ*, 455:536, Dec. 1995.

D. Porter, A. Pouquet, and P. Woodward. Effects of Fluid Turbulence on Stellar Convection. In *American Astronomical Society Meeting Abstracts #184*, volume 26 of *Bulletin of the American Astronomical Society*, page 928, May 1994.

R. E. Pudritz and N. K.-R. Kevlahan. Shock interactions, turbulence and the origin of the stellar mass spectrum. *Philosophical Transactions of the Royal Society of London A: Mathematical, Physical and Engineering Sciences*, 371(2003), 2013. ISSN 1364-503X.

S. Recchi, A. Hacar, and A. Palestini. On the equilibrium of rotating filaments. *MNRAS*, 444:1775–1782, Oct 2014.

V. Rusanov. Calculation of interaction of non-steady shock waves with obstacles. *J. Comput. Math. Phys. USSR*, pages 267–279, 1961.

S. Schneider and B. G. Elmegreen. A catalog of dark globular filaments. *ApJ*, 41: 87–95, Sept. 1979.

P. M. Solomon, A. R. Rivolo, J. Barrett, and A. Yahil. Mass, luminosity, and line width relations of Galactic molecular clouds. *ApJ*, Vol. 319:730–741, Aug 1987.

S. Stahler and F. Palla. *The Formation of Stars*. Wiley, 2008. ISBN 9783527618682.

G. Strang. On the Construction and Comparison of Difference Schemes. *SIAM Journal on Numerical Analysis*, 5:506–517, 1968.

M. Tafalla and A. Hacar. Chains of dense cores in the Taurus L1495/B213 complex. *A&A*, 574:A104, Feb. 2015.

A. Tielens. *The Physics and Chemistry of the Interstellar Medium*. Cambridge University Press, 2005. ISBN 9781139445658.

E. F. Toro. *Riemann Solvers and Numerical Methods for Fluid Dynamics : A Practical Introduction*. Springer-Verlag Berlin Heidelberg, 1999.

J. C. Weingartner and B. T. Draine. Dust Grain-Size Distributions and Extinction in the Milky Way, Large Magellanic Cloud, and Small Magellanic Cloud. *ApJ*, 548:296–309, Feb. 2001.

S. Weinreb, A. H. Barrett, M. L. Meeks, and J. C. Henry. Radio Observations of OH in the Interstellar Medium. *Nature*, 200:829–831, Nov. 1963.

R. W. Wilson, K. B. Jefferts, and A. A. Penzias. Carbon Monoxide in the Orion Nebula. *ApJ*, 161:L43, July 1970.

Appendix

Appendix A: Subroutine DRAGSR

Subroutine for drag force between gas and dust components, according to the aprroach presented by (Miniati, 2010). This subroutine is called by *subroutine source* (see below).

```
subroutine dragSR()
!Gas drag coefficients
 k_G = k0*U(4,i)*sqrt(SSPE)
 k_G2 = k0_2*U(6,i)*sqrt(SSPE)
 k_G3 = k0_3*U(8,i)*sqrt(SSPE)

!Dust drag coefficients
 k_D = k0*U(1,i)*sqrt(SSPE)
 k_D2 = k0_2*U(1,i)*sqrt(SSPE)
 k_D3 = k0_3*U(1,i)*sqrt(SSPE)

!Drag forces for each species
 drag(1) = U(1,i)*k_G*(U(2,i)/U(1,i) - U(5,i)/U(4,i))+&
           U(1,i)*k_G2*(U(2,i)/U(1,i) - U(7,i)/U(6,i))+&
           U(1,i)*k_G3*(U(2,i)/U(1,i) - U(9,i)/U(8,i))
 drag(2) = U(4,i)*k_D*(U(5,i)/U(4,i) - U(2,i)/U(1,i))
 drag(3) = U(6,i)*k_D2*(U(7,i)/U(6,i) - U(2,i)/U(1,i))
 drag(4) = U(8,i)*k_D3*(U(9,i)/U(8,i) - U(2,i)/U(1,i))
end subroutine dragSR
```

Listing 1: Drag force subroutine

Appendix B: Subroutine SOURCE

This subroutine is equivalent to Eq.33 for different applications with or without rotation/dust. It is called from the main program during the application of the splitting methods.

```
subroutine source()
 call gravity()
 call dragSR()

!These source terms are always zero
 SRCE(1,i) = 0d0
 SRCE(3,i) = 0d0
 SRCE(4,i) = 0d0
 SRCE(6,i) = 0d0
 SRCE(8,i) = 0d0


 if (selectdust.eq.1) then
!Source terms with dust and rotation
    if (selectrot.eq.1) then
        SRCE(2,i) = U(1,i)*(GRAV(i) + omega*omega*r(i)) - drag(1)
        SRCE(5,i) = U(4,i)*(GRAV(i) + omega*omega*r(i)) - drag(2)
        SRCE(7,i) = U(6,i)*(GRAV(i) + omega*omega*r(i)) - drag(3)
        SRCE(9,i) = U(8,i)*(GRAV(i) + omega*omega*r(i)) - drag(4)
!Source terms with dust and without rotation
    else
        SRCE(2,i) = U(1,i)*GRAV(i) - drag(1)
        SRCE(5,i) = U(4,i)*GRAV(i) - drag(2)
        SRCE(7,i) = U(6,i)*GRAV(i) - drag(3)
        SRCE(9,i) = U(8,i)*GRAV(i) - drag(4)
    end if
 else
!Source terms with rotation and without dust
    if (selectrot.eq.1) then
        SRCE(2,i) = U(1,i)*(GRAV(i) + omega*omega*r(i))
        SRCE(5,i) = U(4,i)*(GRAV(i) + omega*omega*r(i))
        SRCE(7,i) = U(6,i)*(GRAV(i) + omega*omega*r(i))
        SRCE(9,i) = U(8,i)*(GRAV(i) + omega*omega*r(i))
!Source terms without rotation and without dust
    else
        SRCE(2,i) = U(1,i)*GRAV(i)
        SRCE(5,i) = U(4,i)*GRAV(i)
        SRCE(7,i) = U(6,i)*GRAV(i)
        SRCE(9,i) = U(8,i)*GRAV(i)
    end if
 end if
end subroutine source
```

Listing 2: source subroutine

Appendix C: Subroutine BOUNDARIES

See section 1.4 for further details. This subroutine is called after the physical flux calculation.

```
subroutine boundaries()
do i=1,1
call euler()
end do

!This if-condition changes the outer boundary condition from infalling (b1=3) to a boundary (selectbr) selected in initial.ini
if (selecta.eq.1) then
    if (U(1,1).lt.9e-17) then
      b1=3
    else
      b1=selectbr
    end if
elseif (selecta.eq.0) then
    b1=selectbr
end if

!Reflecting boundary (inner boundary)
    if (selectb.eq.2) then
    VELO_G = -VELO_G
    VELO_D = -VELO_D
    VELO_D2 = -VELO_D2
    VELO_D3 = -VELO_D3
    elseif (selectb.eq.3) then
!Modified reflecting boundary
    VELO_G = 0
    VELO_D = 0
    VELO_D2 = 0
    VELO_D3 = 0
    end if

!Non-reflecting boundary, default inner boundary if reflecting or modified reflecting boundary is not selected
    UBL(1) = DENS_G
    UBL(2) = DENS_G*VELO_G
    UBL(3) = 0d0 !The 3rd term represents the energy conservation equation and is not used
    UBL(4) = DENS_D
    UBL(5) = DENS_D*VELO_D
    UBL(6) = DENS_D2
    UBL(7) = DENS_D2*VELO_D2
    UBL(8) = DENS_D3
    UBL(9) = DENS_D3*VELO_D3

    FBL(1) = DENS_G*VELO_G
    FBL(2) = DENS_G*VELO_G*VELO_G + DENS_G*SSPE(1)
    FBL(3) = 0d0
```

```
    FBL(4) = DENS_D*VELO_D
    FBL(5) = DENS_D*VELO_D*VELO_D
    FBL(6) = DENS_D2*VELO_D2
    FBL(7) = DENS_D2*VELO_D2*VELO_D2
    FBL(8) = DENS_D3*VELO_D3
    FBL(9) = DENS_D3*VELO_D3*VELO_D3

!Non-reflecting boundaty (outer boundary)
    if (b1.eq.1) then
       UBR(:)=U(:,cells)
       FBR(:)=F(:,cells)
!Modified reflecting boundary (outer boundary)
    elseif (b1.eq.0) then
       UBR(1) = U(1,cells)
       UBR(2) = 0d0
       UBR(3) = 0d0
       UBR(4) = U(4,cells)
       UBR(5) = 0d0
       UBR(6) = U(6,cells)
       UBR(7) = 0d0
       UBR(8) = U(8,cells)
       UBR(9) = 0d0
       FBR(1)=0d0
       FBR(2)=UBR(1)*SSPE(cells)
       FBR(3)=0d0
       FBR(4)=0d0
       FBR(5)=0d0
       FBR(6)=0d0
       FBR(7)=0d0
       FBR(8)=0d0
       FBR(9)=0d0

!Reflecting boundary (outer boundary)
    elseif (b1.eq.2) then
       UBR(1) = U(1,cells)
       UBR(2) = -U(2,cells)
       UBR(3) = 0d0
       UBR(4) = U(4,cells)
       UBR(5) = -U(5,cells)
       UBR(6) = U(6,cells)
       UBR(7) = -U(7,cells)
       UBR(8) = U(8,cells)
       UBR(9) = -U(9,cells)

       FBR(1) = -F(1,cells)
       FBR(2) = F(2,cells)
       FBR(3) = 0d0
       FBR(4) = -F(4,cells)
       FBR(5) = F(5,cells)
       FBR(6) = -F(6,cells)
       FBR(7) = F(7,cells)
```

```
      FBR(8) = -F(8,cells)
      FBR(9) = F(9,cells)
    else

!Infall boundary (outer boundary)
      UBR(1) = accdens
      UBR(2) = UBR(1)*accvelo
      UBR(3) = 0d0
      UBR(4) = UBR(1)/334d0
      UBR(5) = UBR(4)*accvelo
      UBR(6) = UBR(1)/333d0
      UBR(7) = UBR(6)*accvelo
      UBR(8) = UBR(1)/333d0
      UBR(9) = UBR(8)*accvelo

      FBR(1) = UBR(1)*accvelo
      FBR(2) = UBR(1)*accvelo*accvelo + UBR(1)*SSPE(cells)
      FBR(3) = 0d0
      FBR(4) = UBR(4)*accvelo
      FBR(5) = UBR(4)*accvelo*accvelo
      FBR(6) = UBR(6)*accvelo
      FBR(7) = UBR(6)*accvelo*accvelo
      FBR(8) = UBR(8)*accvelo
      FBR(9) = UBR(8)*accvelo*accvelo
    end if
  end subroutine boundaries
```

Listing 3: boundaries subroutine

Appendix D: Spectra source code

This is a python code for the development of synthetic spectra. See section 4 for further details.

```
import numpy as np
import matplotlib.pyplot as plt
import time
from astropy.table import Table
from astroML.plotting import setup_text_plots
setup_text_plots(fontsize=22, usetex=True)
fst = 14
fsx = 14
ymdhs = time.strftime("%Y%m%d-%Hh%Mm%s")
#12 Time steps are used for the output
iparts = ['01','02','03','04','05','06','07','08','09','10','11','12']

#Input models
no1 = 'model1infall'
str1 = '20160205-171241.237.out'
no2 = 'model1noinfall'
str2 = '20160205-160250.603.out'
no3 = 'model2'
```

```
19 str3 = '20160205-165157.155.out'
20 no4 = 'model3'
21 str4 = '20151107-164332.947.out'
22 no5 = 'model4'
23 str5 = '20151103-123725.480.out'
24
25 #Selection of one of the models
26 noi = no4
27 stri = str4
28
29 ylim = 3.9e+2 #Axis normalization
30 cells=2000 #Number of cells
31 x = 0.0 #Position of the line of sight, see Fig.3
32 nrm = 11
33 xinpc = x/2000.0*0.5
34 sigma = 200.0 #Thermal broadening
35 I_0 = 1.0 #Amplitude
36 dy = np.zeros(cells)
37 CD = np.zeros(cells)
38 alpha = np.zeros(cells)
39 proj_velo = np.zeros(cells)
40 proj_dens = np.zeros(cells)
41 proj_C18O = np.zeros(cells)
42 proj_N2Hp = np.zeros(cells)
43 dens_C18O = np.zeros(cells)
44 dens_N2Hp = np.zeros(cells)
45 dr = 1.55e+16/cells
46
47 xplot = np.linspace(-6000,6000,3000) #Resolution of the plot
48 yplot_C18O = np.zeros(len(xplot))
49 yplot_N2Hp = np.zeros(len(xplot))
50 fwhm_C18O = np.zeros(len(xplot))
51 fwhm_N2Hp = np.zeros(len(xplot))
52
53 #Initial input for the column density
54 nrm_input = Table.read(noi+'/output-___-part-'+iparts[nrm]+'-'+stri, format
       ='ascii',delimiter=',')
55 CCD = nrm_input['DENS_G'][0]*1.0 #Central column density
56
57 plt.figure(figsize=(8,12))
58 plt.subplots_adjust(hspace=0.0,wspace=0.0)
59 for i1 in range(0,len(iparts)):
60     finput = noi+'/output-___-part-'+iparts[i1]+'-'+stri #Actual input
61     t = Table.read(finput, format='ascii',delimiter=',')
62     DENS = t['DENS_G']
63     VELO = t['VELO_G']
64
65     f = open(finput,'r') #Reading in the time of each time step
66     lines = f.readlines()[0]
67     f.close()
68     time = float(lines[4:10])
```

```
    print time

    #Calculation of the projected velocity and fraction dy of each shell
        for the total line of sight, see Fig.3 and section 4 for further
        details.
    for i in range(1,cells+1):
        if i == 1: #for the inner shell along the line of sight
            if x == 0: #x=0 describes a central line of sight
                alpha[i-1] = np.pi/2.0
            else: #for off-centered spectra
                alpha[i-1] = np.arccos(x/(x+i))/2.0

            proj_velo[i-1] = VELO[x+i-1]*np.sin(alpha[i-1])
            dy[i-1] = np.sqrt((x+i)**2.0 - x**2.0)

        else: #for subsequent shells
            if x == 0: #for central line of sight
                alpha[i-1] = np.pi/2.0
            else: #for off-centered line of sight
                alpha[i-1] = np.arccos(x/(x+i-1.0)) + np.arccos((x+i-1.0)/(x+
                    i))/2.0

            if x+i > cells: #the maximum of x+i is always the number of
                cells, if greater (beyond the simulated filament), density
                and velocity are weighted with non-existing values
                dy[i-1] = 0.0
                proj_velo[i-1] = 999999.0
            else: #if x+1 is smaller than the number of cells
                proj_velo[i-1] = VELO[x+i-1]*np.sin(alpha[i-1])
                dy[i-1] = np.sqrt((x+i)**2.0 - x**2.0) - np.sqrt(((x+i-1))
                    **2.0 - x**2.0)

        if x+i > cells: # density weighting beyond the filaments, as above
            proj_C18O[i-1] = 0.0
            proj_N2Hp[i-1] = 0.0
        else:
            #Selection/Calculation of the cells contributing to C18O
            if DENS[x+i-1]/1000.0 > 1.67303e-21 and DENS[x+i-1]/1000.0 <
                1.67303e-19:
                proj_C18O[i-1] = DENS[x+i-1]*dy[i-1]
                dens_C18O[i-1] = DENS[x+i-1]
            else:
                proj_C18O[i-1] = 0.0
                dens_C18O[i-1] = 0.0
            #Selection/Calculation of the cells contributing to N2H+
            if DENS[x+i-1]/1000.0 > 3.34606e-20:
                proj_N2Hp[i-1] = DENS[x+i-1]*dy[i-1]
                dens_N2Hp[i-1] = DENS[x+i-1]
            else:
                proj_N2Hp[i-1] = 0.0
                dens_N2Hp[i-1] = 0.0
```

```
113
114     yplot_C18O = 0.0
115     yplot_N2Hp = 0.0
116     #Velocity and density is calculated for only on half of the filament
117     #Doubling of the velocity and density vecotr for the calculation of the
            full filament
118     #but with inverted velocities
119     dens_spec_C18O = np.concatenate((proj_C18O,proj_C18O),axis=0)
120     dens_spec_N2Hp = np.concatenate((proj_N2Hp,proj_N2Hp),axis=0)
121     velo_spec = np.concatenate((proj_velo,-proj_velo),axis=0)
122
123     #Calculation of the spectral lines according to Eq.35
124     for i in range(0,len(velo_spec)):
125         yplot_C18O = yplot_C18O + I_0 * np.exp(-(xplot - velo_spec[i])
                **2.0/(2.0*sigma**2.0))*     (dens_spec_C18O[i]/CCD)**1.0 #CCD =
                 Central column density
126         yplot_N2Hp = yplot_N2Hp + I_0 * np.exp(-(xplot - velo_spec[i])
                **2.0/(2.0*sigma**2.0))*(dens_spec_N2Hp[i]/CCD)**1.0
127
128     #Calculation of the full width half maximum
129     yplot_C18O_max = np.max(yplot_C18O)
130     yplot_N2Hp_max = np.max(yplot_N2Hp)
131     for i55 in range(0,len(xplot)):
132         fwhm_C18O[i55] = np.abs(yplot_C18O[i55] - (yplot_C18O_max/2.0))
133         fwhm_N2Hp[i55] = np.abs(yplot_N2Hp[i55] - (yplot_N2Hp_max/2.0))
134     W_C18O = np.argmin(fwhm_C18O[:])
135     FWHMi_C18O = np.abs(2.0*xplot[W_C18O])
136     W_N2Hp = np.argmin(fwhm_N2Hp[:])
137     FWHMi_N2Hp = np.abs(2.0*xplot[W_N2Hp])
138
139     #Setup for plots
140     ax1=plt.subplot(len(iparts)/2,2,(1*i1+1))
141     ax1.set_xticklabels([' ',-1500,-1000,-500,0,500,1000,1500,' '],rotation
            =45,fontsize=fsx)
142     ax1.set_yticklabels([0,1,2,3,4],fontsize=fsx)
143     plt.ylim(0,ylim)
144     plt.tick_params(direction='in', pad=5,width=1,size=5)
145     plt.tick_params(which='minor',width=0.5,size=5)
146     if i1 in (1,3,5,7,9,11): ax1.yaxis.set_major_formatter(plt.
            NullFormatter())
147     if i1 <= 9: ax1.xaxis.set_major_formatter(plt.NullFormatter())
148     if i1 == 8: plt.ylabel('Normalized Intensity')
149     ymax = np.max(yplot_C18O+0.05*yplot_C18O)
150     plt.xlim(-2000,2000)
151     plt.xlabel(r'v [m $s^{-1}$]')
152     if i1 == 0: plt.title("r=%.2f" % float(dr*x/(3.085e16)) + " pc",
            fontsize=16)
153     plt.plot(xplot,yplot_C18O,'b-',lw=1.5,label='$C^{18}O$')
154     plt.plot(xplot,yplot_N2Hp,'r-',lw=1.5,label='$N_{2}H^{+}$')
155     if FWHMi_C18O == 12000: FWHMi_C18O = 0.0
156     if FWHMi_N2Hp == 12000: FWHMi_N2Hp = 0.0
```

```
157     textstr3_N2Hp = "$\Delta v_{N_{2}H^{+}}$=" + "%.2f" % FWHMi_N2Hp + " m/
            s"
158     textstr3_C18O = "$\Delta v_{C^{18}O}$=" + "%.2f" % FWHMi_C18O + " m/s"
159     texttime = "%.2f" % time + " Myr"
160     props = dict(boxstyle='round', facecolor='wheat', alpha=0.0)
161     plt.text(0.03, 0.90, textstr3_C18O, fontsize=fst,transform=ax1.
            transAxes, verticalalignment='top', bbox=props)
162     plt.text(0.03, 0.75, textstr3_N2Hp, fontsize=fst,transform=ax1.
            transAxes, verticalalignment='top', bbox=props)
163     plt.text(0.70, 0.92, texttime, fontsize=fst,transform=ax1.transAxes,
            verticalalignment='top', bbox=props)
164     if i1 == (len(iparts)-1): plt.legend(loc=4, fontsize=fst-2)
165
166 plt.savefig('spectra-'+noi+'-'+ymdhs+'-'+str(xinpc)+'pc.pdf',bbox_inches='
        tight')
167 plt.show()
```

Listing 4: Python code for synthetic spectra